KUNGL
TEKNISKA
HÖGSKOLAN

TRITA-MEK
Technical Report 1998:7
ISSN 0348-467X
ISRN KTH/MEK/TR—98/7-SE

Oblique Waves in Boundary Layer Transition

Stellan Berlin

Doctoral Thesis
Stockholm, 1998

Royal Institute of Technology
Department of Mechanics

Oblique Waves in Boundary Layer Transition

by

Stellan Berlin

May 1998
Technical Reports from
Royal Institute of Technology
Department of Mechanics
S-100 44 Stockholm, Sweden

Typsatt i LaTeX with Stellan's *thesis-style*.

Akademisk avhandling som med tillstånd av Kungliga Tekniska Högskolan i Stockholm framlägges till offentlig granskning för avläggande av teknologie doktorsexamen fredagen den 29:de maj 1998 kl 10.15 i Kollegiesalen, Administrationsbyggnaden, Kungliga Tekniska Högskolan, Valhallavägen 79, Stockholm.

Norstedts Tryckeri AB, Stockholm 1998

Oblique Waves in Boundary Layer Transition

Berlin, S. 1998
Department of Mechanics, Royal Institute of Technology
S-100 44 Stockholm, Sweden

Abstract

Traditional research on laminar-turbulent transition has focused on scenarios that are caused by the exponential growth of eigensolutions to the linearized disturbance equations, e.g. two-dimensional Tollmien-Schlichting waves. Recent research has reveled the existence of other non-modal growth mechanisms, for example associated with the transient growth of streamwise streaks.

Oblique waves may trigger transition in which the new mechanisms is an important ingredient. We have investigated the role of oblique waves in boundary layer transition, using an efficient spectral code for direct numerical simulations.

In the initial stage of this transition scenario oblique waves have been found to interact nonlinearly and force streamwise vortices, which in turn force growing streamwise streaks. If the streak amplitude reaches a threshold value, transition from laminar to turbulent flow will take place.

In the late transition stage, large velocity fluctuations are found at flow positions associated with steep spanwise gradients between the streaks. At those positions we have also found Λ-vortices, structures that are also characteristic for traditional secondary instability transition. The Λ-vortices are shown to be due to the interaction of oblique waves and streaks that seem to play a more important role in the late stage of transition than previously appreciated.

The numerical results are compared in detail with experimental results on oblique transition and good agreement is found.

A new nonlinear receptivity mechanism is found that can trigger boundary layer transition from oblique waves in the free-stream. The mechanism continuously interact with the boundary layer and the resulting transition scenario is characterized by the growth of streamwise streaks. The same structures that are observed in experiments on transition caused by free-stream turbulence. A linear receptivity mechanism that interact with the boundary layer downstream of the leading edge is also identified. It is related to linear receptivity mechanisms previously studied at the leading edge. The nonlinear and linear mechanisms are of comparable strength for moderate free-stream disturbance levels.

Two strategies for control of oblique transition are investigated, both based on spanwise flow oscillations. The longest transition delay was found when the flow oscillations were generated by a body force. When the control was applied to a transition scenario initiated by a random disturbance it was more successful and transition was prevented.

Descriptors: laminar-turbulent transition, boundary layer flow, oblique waves, streamwise streaks, Λ-vortex, transient growth, receptivity, free-stream turbulence, nonlinear mechanism, neutral stability, non-parallel effect, DNS, spectral method, transition control.

Preface

This thesis on boundary layer transition is structured according to the present tradition at KTH and the faculty of engineering physics. It contains a collection of articles and reports of research results. They have been published in or submitted to scientific journals and are written accordingly. The first part is a summary of the results presented in the papers, where the work is put into a historic perspective and related to the work of other researchers. However, the summary it is not intended to be a general review of transition research. The ambition has instead been to make the material in the summary accessible to a wider audience than those daily confronted with fluid dynamics and transition to turbulence.

Acknowledgments

Several persons have inspired me and contributed to this work in their own special way and I would like to express my sincere gratitude to them.

Of outstanding importance is Prof. Dan Henningson, who not only initiated this research but also has been the perfect advisor. He has generously shared his knowledge and made many interesting problems visible. I have been free to chose my own path and always felt his inspiring interest in my work. Dan also has given me valuable opportunities to meet and interact with other people in the international research community.

The programming skills of Dr. Anders Lundbladh has saved me many valuable hours of CPU time and I have been fortunate to have Anders as teacher in Fortran programming, guide in the world of parallel super computers and problem solver.

My first steps in transition research were also guided by Prof. Peter Schmid and I have always enjoyed and looked forward to his regular visits to our office.

Prof. John Kim and his students in particular Mr. Jasig Choi introduced me to the area of flow control during my enjoyable stay at UCLA. They also shared their experience of numerical simulations with me.

I have had many opportunities to develop my interest for computers and UNIX in particular. In that process Dr. Arne Nordmark has been invaluable. My only disappointment is that I have not been able to provide him with a problem that he could not solve.

It has been inspiring and valuable to discuss and compare calculations with the experimental data that Dr. Markus Wiegel has presented and shared with me.

In daily work and all sorts of other activities my colleges, friends and room mates at the Mechanics department has provided an nice atmosphere, in which I have been happy even when results has been poor.

Many thanks to all of you!

This work has been supported by TFR (Swedish Research Council for Engineering Sciences).

Contents

CHAPTER 1

Introduction

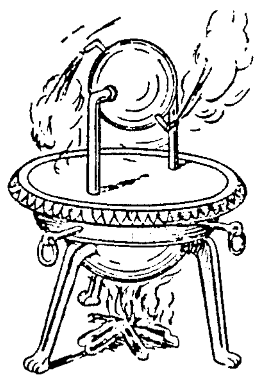

FIGURE 1.1 Heron's "gas-turbine"

Our climate and weather are governed by the fluid dynamics of the atmosphere and since there often is a strong interest in tomorrows forecast, meteorology is a popular application of fluid dynamics. Knowledge in fluid dynamics has been used and been of great interest throughout history. Early civilizations used complicated irrigation systems and the first "designers" of floating vessels certainly wanted to optimize for speed or load. Heron of Alexandria was an early observer of fluid phenomena and figure 1.1 contains a sketch of his "gas-turbine". Water is heated to produce steam, which is directed such that the sphere on the top of the device rotates. Heron probably did not find much use of his apparatus at the time. Today, however, design of turbines, for both propulsion and power generation, are as important applications of fluid dynamics as is the construction of vehicles.

It is easy to observe that a fluid sometimes moves in an ordered, predictable fashion, like when you pour coffee out of an old fashioned pot. However, when the coffee comes in the cup the motion is suddenly swirly and chaotic. We distinguish these states as laminar or turbulent flow. Why, when and how the transition between the two takes place is of great practical interest. A laminar flow over the surface of a vehicle is often desired since the drag force on the vehicle is much lower than had the flow been turbulent. Enormous amounts of fuel could be saved if we could control the characteristics of turbulence to reduce drag or even prevent its occurrence. At other instances turbulence is desired,

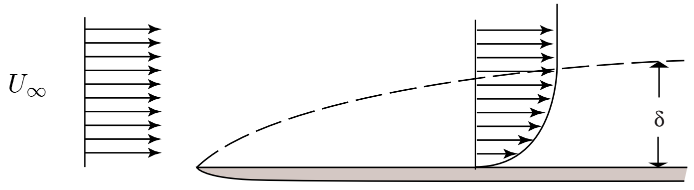

FIGURE 1.2 Plate creates boundary layer with thickness δ in oncoming uniform flow U_∞.

for example to mix sugar in the coffee or improve the mixing of fuel and air in a combustion engine.

We simplify the study of the laminar-turbulent transition process by considering a very simple geometry (figure 1.2), a flat plate with a leading edge in the direction of a uniform oncoming flow. The fluid on the surface of the plate is slowed down by the friction. A boundary layer is formed, in which the fluid velocity changes form the speed of the free stream to be zero at the plate surface. The boundary layer is caused by viscosity (internal friction) and its thickness grows as the flow evolve downstream. It is well know that this flow, at some position downstream, will become turbulent and by studying this simple case we can hope to gain enough insight into the physics of laminar turbulent transition to be able to predict and understand more complicated situations.

The transition process of the boundary layer can be further divided into two stages. First a disturbance from the free-stream or a roughness on the plate has to cause a flow disturbance in the boundary layer. A process normally denoted receptivity. Secondly the disturbance will either grow or decay depending on its characteristics. Research on the second topic, the stability problem, has been more intense and the major interest has been on two-dimensional so called Tollmien-Schlichting waves.

However, recent findings has clearly indicated that other types of disturbances, can also be very potent causes of transition. A pair of oblique waves is such an example and this thesis is focused on the mechanisms by which oblique waves cause transition. The very same month as this work begun, the journal "Theoretical and Computational Fluid Dynamics" received an article by Joslin, Streett & Chang (1993). They had calculated transition caused by two oblique waves primarily to verify two numerical codes, and they write " … no adequate formal theory is available to explain the breakdown process … ". You will hopefully find that this thesis give a valuable contribution to the understanding of oblique transition.

CHAPTER 2

Basic concepts and notation

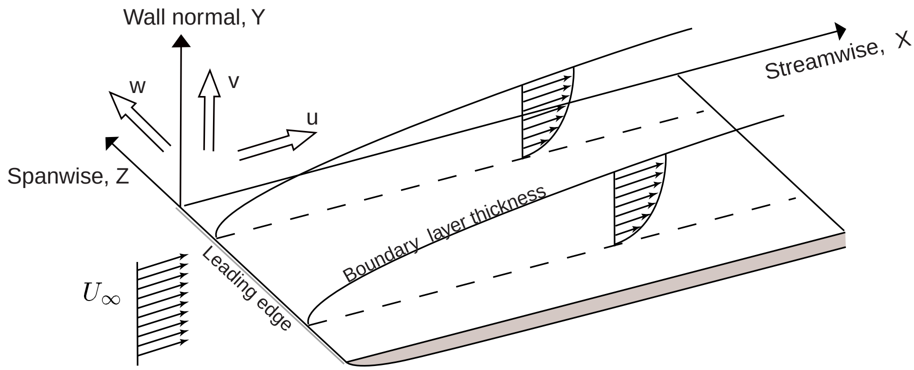

FIGURE 2.1 Boundary layer flow with free-stream velocity U_∞. The velocity has components u v and w in the coordinate system x, y and z.

2.1. Coordinate system and flow decomposition

We start by defining the basic terminology and the coordinate system, with the help of figure 2.1. The main flow is uniform and not affected by the plate, which causes the formation of the boundary layer. It is directed in the streamwise, x, direction and denoted U_∞ or free-stream. A natural point to define as the origin, $x = 0$, is the point where the flow meet the plate, the leading edge. But our computations will not start at that position and we therefore often define $x = 0$ to be at the starting point of our calculations. The direction normal to the plate will be denoted y, with $y = 0$ at the plate surface. The direction parallel to the leading edge, the spanwise direction, is called z. We consider the plate to be infinite in that direction and define $z = 0$ as the center of the domain we are considering.

The flow may be in any direction but we will always divide its total velocity into three parts, each following one of the coordinate directions. The velocity components in the x, y and z directions will be denoted $\mathcal{U}$, $\mathcal{V}$ and $\mathcal{W}$ respectively. We often study disturbances that are small compared to the total velocity and to aid the analysis we decompose the flow in the following way:

$$\mathcal{U} = U + u,\ \mathcal{V} = V + v,\ \mathcal{W} = W + w,\ \mathcal{P} = P + p. \quad (1)$$

U, V and W are the base flow that we would have if no disturbance was present and u, v and w are the disturbance velocities, P and p are the corresponding pressures. In the following the spanwise base flow component W will always be zero.

A disturbance may either be constant over time or fluctuating. The constant part is separated by calculating time averages of the disturbance, which we denote $\bar{u}$ $\bar{v}$ and $\bar{w}$. What remains is then the fluctuating part: $\tilde{u}$ $\tilde{v}$ and $\tilde{w}$. The fluctuating part can also be studied by computing the root mean square of the disturbance, denoted u_{rms}, v_{rms} and w_{rms}.

Vorticity in the three coordinate directions are defined as,

$$\omega_x = \frac{\partial w}{\partial y} - \frac{\partial v}{\partial z},\ \omega_y = \frac{\partial u}{\partial z} - \frac{\partial w}{\partial x},\ \omega_z = \frac{\partial v}{\partial x} - \frac{\partial u}{\partial y}. \tag{2}$$

These can be decomposed in the same way as the velocity components. A vortex in the x direction is a swirling motion around an axis parallel to the x axis and is associated with vorticity ω_x. However, it is important to note that vorticity itself does not imply the presence of a vortex.

2.2. Wave disturbances

Disturbances are often wave-like, which suggests a decomposition of the total disturbance into a sum of waves. We frequently perform the decomposition with the aid of Fourier transforms. Figure 2.2 displays a wall parallel plane of a flow with a wave propagating at an angle to the mean flow direction, with the lines representing positions of constant phase. We can then define wavelengths λ_x and λ_z in the streamwise and spanwise directions respectively. A stationary observer will register a frequency ω, with which he repeatedly makes the same observation. A velocity component, for example v, of a single wave disturbance depending on all coordinates and time t, may now be represented as,

$$v(x,y,z,t) = \hat{v}(y)e^{i(k\alpha x + l\beta y - m\omega t)},\ \alpha = \frac{2\pi}{\lambda_x},\ \beta = \frac{2\pi}{\lambda_z}, \tag{3}$$

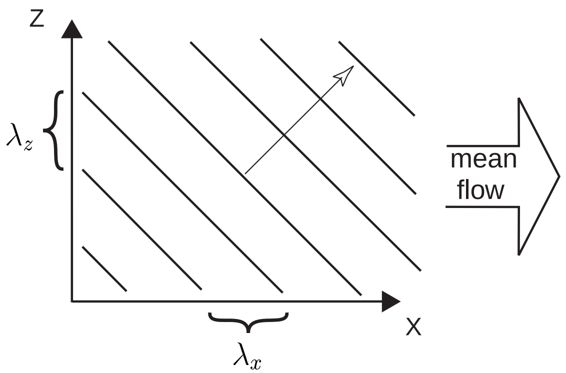

FIGURE 2.2 Wave propagating at an angle to the meanflow U, with streamwise wavelength λ_x and spanwise wavelength λ_z.

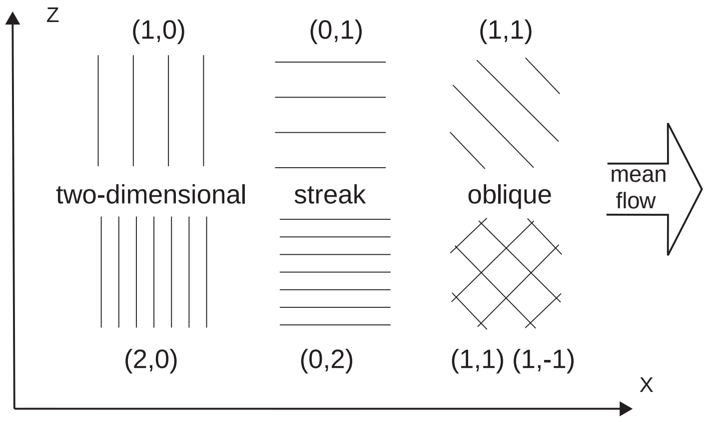

FIGURE 2.3 Examples of the notation for wave disturbances

where α and β are the streamwise and spanwise wavenumbers, respectively. Note that the frequency ω is closely related to α by the speed with which the disturbance travels downstream. α, β and ω are chosen to represent the primary wave disturbance that we like to study. The integers (or integer fractions) k, l and m can then be used to represent all other disturbances in the wave decomposition and relate them to the primary one. If we consider the flow at a specific time t, a disturbance will be denoted as a mode (k, l), meaning a disturbance with streamwise wavenumber $k \cdot \alpha$ and spanwise wavenumber $l \cdot \beta$. If we instead consider specific downstream position x we will have modes (m, l), representing frequency $m \cdot \omega$ and spanwise wavenumber $l \cdot \beta$. They however represent the same type of disturbance in the flow. Some examples are displayed in figure 2.3.

2.3. Navier-Stokes equations and stability concepts

The development and interaction in space and time of the flow and the disturbance wave modes studied in this thesis, are governed by the Navier-Stokes equations and a continuity equation saying that fluid is not created and cannot disappear. The viscosity, which is a measure of the fluids internal friction or "resistance to flow" is considered constant (Newtonian fluid) as well as the density of the fluid (incompressible fluid).

If only the linear part of the Navier-Stokes equations is considered each mode will develop individually and the total flow will be the sum of all involved modes. In the full nonlinear case the modes will exchange energy within triplets. An interacting triplet is formed by three modes, where two may be identical, (a, b), (c, d) and (e, f) and energy is exchanged if $a + c + e = 0$ and $b + d + f = 0$ and at least two of the modes have non-zero energy. If a mode will gain or lose energy depends on the relation between them at the considered instant. When the energy in one mode is increased we frequently say that it is generated by the nonlinear interaction with two others for example $(1, -1)$ and $(1, 1)$ generates $(0, 2)$.

Except when comparisons has been made with experiments, the velocities and lengths used in this thesis are non-dimensional. All the information specific for a particular flow is gathered in the non-dimensional Reynolds number $R = U_\infty \delta^*/\nu$, which also appears in the Navier-Stokes equations. The Reynolds number can be defined in several ways, but we have chosen to base it on the kinematic viscosity ν, the displacement thickness δ^* and the free-stream velocity U_∞, which thus become the quantities used to scale the lengths and velocities, respectively. The displacement thickness is a measure of the boundary layer thickness and for a Blasius boundary layer it takes the form $\delta^* = 1.72\sqrt{\nu x/U_\infty}$. The point of using non-dimensional quantities is that we in different flows or fluids will observe the same physical phenomena as long as the Reynolds number is equal, and the results will therefore become more general.

When the Navier-Stokes equations equations are analyzed for possible disturbance growth in boundary layer flows the decomposition (1) is used in most cases together with two simplifications. The nonlinear terms are neglected and the base flow is assumed to have only one non-zero component $U(y)$, which only depend on the wall normal y direction. That leads to what we call the disturbance equations, which are initial value problems. The further assumption of exponential time dependence (complex) leads to the Orr-Sommerfeld and Squire equations, which constitutes eigenvalue problems. There is a disturbance that can grow exponentially if an unstable eigenvalue is found, and we talk about exponential instability. If the base flow is unstable and deformed by the growth of a first disturbance the stability of the deformed flow may be analyzed. If that is found unstable, it is regarded as a secondary instability and transition to turbulence usually follows.

2.4. Numerical solution procedures

The results in this thesis are, however, not from theoretical analysis of linear stability equations but from computer solutions of the complete Navier-Stokes equations so called direct numerical simulations (DNS). Both a temporal and a spatial solution procedure has been used. In the temporal method, a localized disturbance or wave is followed in time as it travels downstream. The thickness of the surrounding boundary layer does not vary in the streamwise direction but it grows slowly in time to approximate the real downstream growth. The extent of the computational domain is small as only one wave length of the largest disturbance is included in the streamwise and spanwise directions. A much larger streamwise region is included in the spatial method, which makes it considerably more computer demanding. The boundary layer growth and pressure gradients are, however, correctly accounted for and the flow develops downstream as in experiments, with which spatial results can be directly compared.

We are fortunate to know the equations that are believed to model the studied flow. Our numerical solver, which excludes the leading edge, is very accurate, efficient and well suited for the parallel super computers that have been used. Even so, only a small region of the very simple geometry could be solved at low flow velocities. This demonstrates the need for more understanding, in order to develop simple models applicable to complex flows, for which computers will be too slow to solve the Navier-Stokes equations for a long time yet.

CHAPTER 3

Theoretical background and previous findings

3.1. Stability

3.1.1. Inviscid flows. Traditional stability analysis of boundary layer flow has dealt with three questions: under what circumstances can a small disturbance grow such that it at any later time is larger than it was at time $t = 0$, which disturbances are that and which disturbance grows the most. The first results were obtained by dropping the nonlinear terms in the disturbance equations and neglecting viscosity. Rayleigh found the necessary condition that the base flow profile had to have an inflection point. Fjørtoft improved the condition by including that $\partial U/\partial y$ should have a maximum at the inflection point. The first high frequency oscillations observed in transition to turbulence are often found in connection with inflection points.

3.1.2. Stability of Tollmien-Schlichting waves. Later viscosity was included and the disturbance equations analyzed in the form of the Orr-Sommerfeld equation for exponentially growing disturbances. The first solutions for two-dimensional eigenfunctions of the Orr-Sommerfeld equation were presented by Tollmien (1929) and Schlichting (1933). If such Tollmien-Schlichting waves or TS-waves existed were debated until they were identified in experiments by Schubauer & Skramstad (1947). Thereafter the focus of transition research were set on TS-waves. The neutral stability curve was calculated. It defines the domain of disturbance frequencies and Reynolds numbers for which a TS-wave may grow. The theory assumes that the boundary layer has a constant thickness whereas it actually grows downstream and experimental results did not completely agree with the theory. Several corrections for non-parallel effects to the original theory were suggested. Spatial simulations by Fasel & Konzelmann (1990) gave insight to how discrepancies between theory and experiments were caused by differences in the evaluation of the growth rate. Klingmann *et al.* (1993) pointed at experimental errors caused by the leading edge geometry and pressure gradients. Bertolotti, Herbert & Spalart (1992) found non-parallel effects to be larger for oblique waves and non-linearity to be destabilizing. They also computed the neutral stability curve for a growing Blasius boundary calculated by parabolic stability equations (PSE). DNS calculations of the non-parallel neutral stability curve is presented in paper 1.

Since turbulence is three-dimensional, an important issue is to understand how the flow becomes three-dimensional from the growing two-dimensional TS-waves. Two basic scenarios were identified by experimental investigators. Each has a characteristic three-dimensional “non-linear stage”, after the linear growth of the TS-wave, but before the flow is fully turbulent. Klebanoff, Tidstrom & Sargent (1962) observed what today is called K-type transition after Klebanoff or fundamental breakdown. In its non-linear stage rows, aligned with the stream direction, of "Λ-shaped" vortices appears in the flow (see figure 6.7(c)). The other scenario was first observed by Kachanov, Kozlov & Levchenko (1977) and is called subharmonic or H-type transition after the theoretical work by Herbert (1983, 1983). In the three-dimensional stage of that scenario Λ-vortices are found to create a staggered pattern (see figure 6.7(b)). Kachanov (1994) calls the latter scenario N-type transition, after "New" or "Novosibirsk", in his review over the physical mechanisms involved in transition. Theoreticians have explained the three-dimensional stage as wave resonance Craik (1971) or secondary instability and a review over the theoretical efforts concerning the secondary instabilities has been written by Herbert (1988). Kleiser & Zang (1991) has reviewed the numerical work in the area, which up to that date mostly used a temporal approach. Since then e.g. Rist & Fasel (1995) have presented a spatial simulation of K-type transition in boundary layer flow.

3.1.3. Transient growth and sensitivity to forcing. Before the 1940's experimental investigators were unable to identify TS-waves and the following secondary instability in both boundary layers and channel flows. Transition was instead often caused by other disturbances and other growth mechanisms. These are obviously as likely now as they were then. Morkovin (1969) stated "We can bypass the TS-mechanism altogether", and transition caused by growth mechanisms other than exponential instabilities are often named *bypass-transition*. Oblique transition is an example of bypass-transition.

An important observation is that the nonlinear terms of Naiver-Stokes equations conserve energy. The instantaneous growth mechanisms behind bypass transition can therefore be found by examining the linearized disturbance equations. The existence of growth mechanisms other than those associated with exponential growth were known already to Orr (1907) and Kelvin (1887). Those mechanisms can cause disturbances growth for a limited time, but the disturbances will eventually decay in the linear viscous approximation. The Navier-Stokes equations are however nonlinear and if the transient growth creates a disturbance large enough, transition to turbulence will occur. The investigations by for example Gustavsson (1991), Butler & Farell (1992), Reddy & Henningson (1993), Trefethen *et al.* (1993) showed the possible magnitude of transient growth and clearly indicated the potential of non-modal mechanisms for causing transition.

The physical mechanism behind this growth is the *lift-up* mechanism, weak streamwise counter rotating vortices in the boundary layer lift up fluid with low streamwise velocity from the wall and bring high speed fluid down towards the wall. As this process continues at constant spanwise position, large amplitude streaks in the streamwise velocity component will be created. In the inviscid case the corresponding perturbation amplitude grows linearly with time, something recognized by Ellingsen & Palm (1975).

Mathematically, transient growth can be explained by the fact that the eigenfunctions of the linearized disturbance equation has non-orthogonal eigenfunctions. This mathematical property has another consequence, the linear system may show a large response to forcing. This means that a small energy input through an outer source of the flow or through the nonlinear terms may cause large disturbance growth.

In most of the theoretical work on transient growth and the sensitivity to forcing (both non-modal mechanisms), a temporal formulation has been used. The disturbances are then thought to grow in time, which simplifies analysis and calculations. In a physical experiment or a spatial simulation, disturbances grow in space. Recently transient growth in boundary layers, or maybe better non-modal growth, has been considered in spatial formulations by Luchini (1996, 1997) and Andersson, Berggren & Henningson (1997). They found that the maximum possible energy growth scales linearly with the distance from the leading edge.

Growing TS-waves causes disturbances that vary periodically in the streamwise direction and are elongated in the spanwise. The non-modal mechanisms causes disturbances that vary periodically in the spanwise direction and are elongated in the streamwise. Nonlinear mechanisms are needed for development of more complicated flow structures and the occurrence of transition to turbulence. The development of theories concerning this process associated with streaks have just started and Reddy *et al.* (1997) have for channel flows found that streak breakdown is caused by an inflectional secondary instability, normally in the spanwise direction but for some cases in the wall-normal direction.

The possibilities of strong non-modal growth discussed above explains that transition do occur even when no exponential instabilities exist. In cases where exponential instabilities are present, there will be a competition or combination between the different mechanisms depending on the disturbances present. And obviously the nonlinear coupling between different disturbances will play an important role.

3.2. Receptivity mechanisms

3.2.1. TS-wave receptivity. To understand and predict boundary layer transition, knowledge in how the disturbances can enter or interact with the boundary layer is necessary. Receptivity researchers have therefore investigated how TS-waves can be generated in the boundary layer by outer disturbances. The disturbances are often characterized as either acoustic disturbances or vortical disturbances convected by the free-stream. Both types of disturbances has been theoretically investigated by asymptotic methods and a summary of the results can be found in the reviews by Goldstein & Hultgren (1989) and Kerschen (1990). They find that the receptivity to both disturbance types are of the same order and is found in the leading edge region, associated with rapid geometry changes or local roughness. The experimental findings on TS-wave receptivity has been reviewed by Nishioka & Morkovin (1986) and generally compare well with the theoretical ones. The effect of free-stream sound has also been investigated numerically by Lin, Reed & Saric (1992). They found receptivity at their elliptical leading edge and that a sharper leading edge gave less receptivity and that the sudden pressure gradients appearing at the junction of the leading edge and the flat plate was an important receptivity source. Buter & Reed (1994) investigated the effect of vortical disturbances at the leading edge numerically and found the same sources of receptivity as Lin, Reed & Saric (1992).

3.2.2. Receptivity to free-stream turbulence. Experiments of laminar boundary layers developing in a turbulent free-stream are characterized by disturbances very different from TS-waves, namely streamwise elongated streaks. These were first observed as low-frequency oscillations in hot-wire signals, caused by slow spanwise oscillations of the streaks. They are commonly referred to as Klebanoff-modes after Klebanoff's (1971) mainly unpublished experimental findings (Kendall 1985). After comparing data from several experiments Westin (1994) *et al.* drew the conclusion that there is no general correlation between the level of free-stream turbulence, the fluctuation level in the boundary layer and the transitional Reynolds number. They compared results for the streamwise velocity component, which is what is normally reported from the experimental investigations. Yang & Voke's (1993) numerical experiment however, indicated that the wall normal velocity component of the free-stream turbulence is more important for the response in the boundary layer. Experimental findings concerning scaling relations and effects of the leading edge are inconclusive.

Choudhari (1996) used asymptotic methods to study the receptivity of oblique disturbances and found the receptivity by the leading edge and local humps to increase with increased obliqueness of vortical disturbances. He also noted that the wall normal distribution response to the oblique disturbances was similar to the Klebanoff mode. Bertolotti (1997) assumed free-stream modes, periodic in all directions, of which he calculated the boundary layer receptivity in a "linear region" excluding the the leading edge. He found receptivity to modes with zero streamwise wavenumber. These modes are used as forcing in PSE calculations of the downstream disturbance development and the results agree fairly well with experimental results. Bertolotti (1997) found it most likely that the growth of streaks is related to non-modal growth. Andersson, Berggren & Henningson (1998) and Luchini (1997) used an optimization technique to determine what disturbance present at the leading edge will give the largest disturbance in the boundary layer. They also found streamwise vortices causing growth of streaks and both the wall normal disturbance shape and growth rates agreed with the findings of Bertolotti (1997) and was also close to the experimental results. There are, however, some discrepancies between calculations and experiments concerning the growth rate and the slightly downstream increasing spanwise scale of the streaks in the experiment.

The importance of TS-waves for transition caused by free-stream turbulence is not clear. Generally, fluctuations with a frequency close to the most unstable TS-waves are found at the boundary layer edge and have a mode shape different from the unstable eigenmode. At high turbulence levels TS-waves are difficult to identify, but for low free-stream turbulence levels Kendall (1990) did identify wave packets traveling with the same phase speed as TS-waves. Boiko *et al.*

(1994) introduced additional TS-waves in an experiment of free-stream turbulence and found their amplification rate to be smaller than in the undisturbed boundary layer.

3.3. Oblique transition

Oblique transition is a transition scenario initiated by two oblique waves with opposite wave angle and in which non-modal growth plays an important role. Lu & Henningson (1990) first noted the potential of oblique disturbances in incompressible flows in their study of subcritical transition in Poiseuille flow. Schmid & Henningson (1992) then calculated oblique transition in channel flow using a temporal DNS code. They showed, for plane Poiseuille flow, that initial forcing and subsequent transient growth caused the rapid growth of the $(0,2)$ mode. They calculated the relation between the energy transfered to the $(0,2)$ mode by the nonlinear terms and the energy growth by transient linear mechanisms and found the latter to be the significant part. Joslin, Streett and Chang (1992,1993) calculated oblique transition in an incompressible boundary layer using both parabolized stability equations (PSE) and spatial DNS. They chose two different amplitudes of the oblique waves. In the low amplitude case the $(0,2)$ mode grew rapidly and then decayed whereas they noted both the rapid growth of the $(0,2)$ mode and a subsequent growth of other modes in the high amplitude case.

That was the state when the present work begun, but the interest in oblique transition and streak breakdown is increasing and several investigators have been active with parallel work. Reddy *et al.* (1997) found that the energy needed in channel flow to initiate oblique transition is substantially lower than that needed in the transition scenarios caused by the two-dimensional TS-wave. Similar results have also been found in boundary layer flow by Schmid, Reddy & Henningson (1996). Experimentally oblique transition has been investigated in Poiseuille flow by Elofsson (1995) and those results were compared with calculations by Elofsson & Lundbladh (1994). In boundary layers experimental investigations has been made by Wiegel (1996) and Elofsson (1997)

Oblique transition has also been studied in compressible flows, where Fasel & Thumm (1991) noted that it is a "powerful process". Using nonlinear PSE Chang & Malik (1992, 1994) studied this scenario in a supersonic boundary layer and found oblique-wave breakdown to be a more viable route to transition and that it could be initiated by lower amplitude disturbance, compared to traditional secondary instability. Using DNS Fasel, Thumm & Bestek (1993) and Sandham, Adams & Kleiser (1994) studied oblique transition in compressible boundary layers and all investigators observed, first the nonlinear interaction of the oblique waves generating the streamwise vortex mode $(0,2)$ and then its rapid growth. The fact that the rapid growth of the $(0,2)$ mode was caused by non-modal growth and the non-normality of the linear operator was shown by Hanifi, Schmid & Henningson (1996).

3.4. Transition control

Delaying laminar-to-turbulent transition has many obvious advantages and the simplest method is perhaps to shape the surface on which the boundary layer develop such that a suitable pressure distribution is obtained. Common means for flow control such as combinations of blowing, suction, heating, cooling and magneto-hydrodynamic (MHD) forces have been used to obtain transition delay. The efforts has been reviewed by Gad-el-Hak (1989). The control has either aimed for a more stable mean flow profile or for cancellation of growing Tollmien-Schlichting (TS) waves or waves associated with the secondary instability caused by TS-waves, see for example Thomas (1983), Kleiser & Laurien (1985), and Danabasoglu, Biringen & Streett (1991).

Reports on transition control of oblique transition or transition caused by free-stream turbulence that are both characterized by streaks and streamwise vortices are not found. However, smaller scale streamwise vortices in the near-wall region of turbulent boundary layers have in recent studies (Choi, Moin & Kim 1993) been shown responsible for high skin-friction drag. Successful control strategies have been found to reduce their strength. A simple control strategy that by Akhavan, Jung & Mangiavacchi (1993) was shown to reduce turbulence and skin-friction was the generation of a spanwise oscillatory flow.

CHAPTER 4

Numerical method

The direct numerical simulations presented in this thesis have all been performed with the spectral algorithm described in detail in paper 6. In spectral methods the solution is approximated by an expansion of smooth functions. The mathematical theories concerning the functions we have used, dates back to the nineteenth century and the works by Fourier and Tjebysjov. The idea of using them for numerical solutions of ordinary differential equations is attributed to Lancos (1938). The earliest applications to partial differential equations were developed by Kreiss & Oliger (1972) and Orzag (1972), who termed the method pseudo-spectral. The reason was that the multiplications of the nonlinear terms were calculated in physical space to avoid the evaluation of convolution sums. The transformation between physical and spectral space can be efficiently done by Fast Fourier Transform (FFT) algorithms that became generally known in the 1960's (Cooley & Turkey 1965).

The fast convergence rate of spectral approximations of a function, results in very high accuracy per included spectral mode compared to the accuracy produced by finite-element or finite difference discretizations with corresponding number of grid points. Efficient implementations of pseudo-spectral methods can be made thanks to the low costs of performing FFTs. Moreover, the data structure makes the algorithms suitable for both vectorization and parallelization, which obviously stretches the applicability. The high density of points close to boundaries in the physical domain naturally obtained by Chebyshev series is also profitable for wall bounded flows. The spectral approximation and the associated boundary conditions limts the applications to simple geometries. A disadvantage is also that the method is "global", which means that poor resolution in one part of the computational domain corrupts the whole calculation.

Pseudo-spectral methods became widely used for a variety of flows during the 1980's. Early boundary layer results for transitional flow were presented by Orszag & Patera (1983). They used a temporal formulation and the first spatial boundary layer computations were presented by Bertolotti, Herbert & Spalart (1992).

The numerical code used for the calculations presented in this thesis is a development of the channel code by Lundbladh, Henningson & Johansson (1992) and solves the full three-dimensional incompressible Navier-Stokes equations. It handles pressure gradients and can be used for both temporal and spatial simulations.

The algorithm is similar to that for channel geometry of Kim, Moin & Moser (1987), using Fourier series expansion in the wall parallel directions and

Chebyshev series in the normal direction and pseudo-spectral treatment of the non-linear terms. The time advancement used is a four-step low storage third-order Runge-Kutta method for the nonlinear terms and a second-order Crank-Nicholson method for the linear terms. Aliasing errors from the evaluation of the nonlinear terms are removed by the $\frac{3}{2}$-rule when the horizontal FFTs were calculated. In order to set the free-stream boundary condition closer to the wall, a generalization of the boundary condition used by Malik, Zang & Hussaini (1985) was implemented. It is an asymptotic condition applied in Fourier space with different coefficients for each wavenumber that exactly represents a potential flow solution decaying away from the wall. To enable spatial simulations with a downstream growing boundary layer and retain periodic boundary conditions in the streamwise direction a "fringe region", similar to that described by Bertolotti, Herbert & Spalart (1992) has been implemented. In this region, at the downstream end of the computational box, the function $\lambda(x)$ in equation (4) is smoothly raised from zero and the flow is forced to a desired solution $\mathbf{v}$ in the following manner,

$$\frac{\partial \mathbf{u}}{\partial t} = NS(\mathbf{u}) + \lambda(x)(\mathbf{v} - \mathbf{u}) + \mathbf{g} \tag{4}$$

$$\nabla \cdot \mathbf{u} = 0 \tag{5}$$

where $\mathbf{u}$ is the solution vector and $NS(\mathbf{u})$ the right hand side of the (unforced) momentum equations. Both $\mathbf{g}$, which is a disturbance forcing, and $\mathbf{v}$ may depend on the three spatial coordinates and time. $\mathbf{v}$ is smoothly changed from the laminar boundary layer profile at the beginning of the fringe region to the prescribed inflow velocity vector, which in our case is a Blasius boundary layer flow. This method damps disturbances flowing out of the physical region and smoothly transforms the flow to the desired inflow state in the fringe, with a minimal upstream influence. Figure 4.1 illustrates the variation of the boundary layer thickness and the meanflow profile in the computational box for a laminar case.

Disturbances to the laminar flow can be introduced by three methods: They could be included in the flow filed $\mathbf{v}$ and forced in the fringe region, a body force $\mathbf{g}$ can be applied at any position of the box or a blowing and suction boundary condition at the wall can be used.

The code has been thoroughly checked and used in several investigations by a number of users on a variety of workstations and supercomputers.

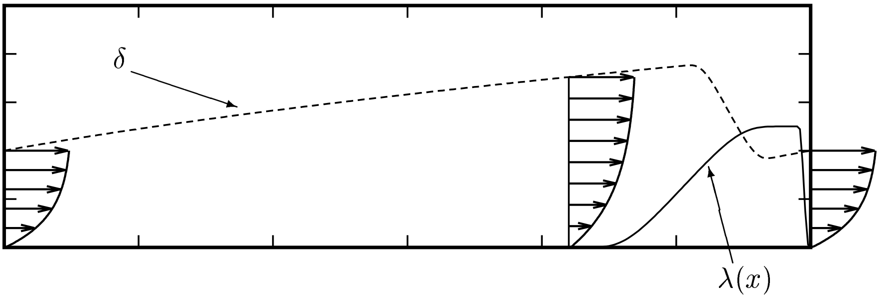

FIGURE 4.1 The boundary layer thickness δ (dashed) of a laminar mean flow grows downstream in the physical domain and is reduced in the fringe region by the forcing. The flow profile is returned to the desired inflow profile in the fringe region, where the fringe function $\lambda(x)$ is nonzero.

CHAPTER 5

The neutral stability curve for non-parallel boundary layer flow

The aim of the present part of the thesis has been to determine the complete neutral stability curves and critical Reynolds numbers by DNS, for growth in both the wall normal as well as the streamwise velocity components, in zero-pressure gradient, incompressible, non-parallel boundary layer flow. Results that have not been presented before and they are compared with results from PSE calculations.

We have put great effort into reducing disturbances caused by the generation of the waves and numerical issues in our DNS calculations. Such disturbances can influence the determination of the neutral points, something noted by previous investigators who at some occasions were forced to use smoothing to suppress oscillations.

When a TS-wave develops downstream, not only does its amplitude change but also the wall normal mode shape. Following a wall normal maxima downstream gives a result that cannot be misleading and is well suited for comparison with both theory and experiments. We have followed the lower/inner maxima of u and the single maxima of v, when evaluating the growth and neutral points in our calculations.

The results are presented in figure 5.1 in a diagram with the Reynolds number on the horizontal axis and on the vertical axis the non-dimensional frequency $F = 2\pi f\nu/U_\infty \times 10^6$, where f is the dimensional frequency, U_∞ the free-stream velocity and ν the kinematic viscosity. The dashed grey curves in the figure represent the DNS results. The curve enclosing a larger region represents the neutral curve for v, whereas the neutral curve for u encloses a smaller unstable region. The two solid lines in figure 5.1 represents the neutral curves of u and v found by the PSE method. The agreement between PSE and DNS is excellent. Based on both methods we determined the critical Reynolds number to 456 for v and 518 for u, with a uncertainty of respectively, ± 2 and ± 1.

Figure 5.1 also contains neutral stability points presented by Fasel & Konzelmann (1990) and we find good agreement between those results and our calculations. The circles represent experimental data obtained by Klingmann *et al.* The experimental flow is more unstable at higher frequencies than the calculations predict, but is considerably closer to the calculations than previous experimental results. The difficulty of obtaining experimental results that agree well with calculations for this very simple flow, is ominous of more complicated flows or disturbances.

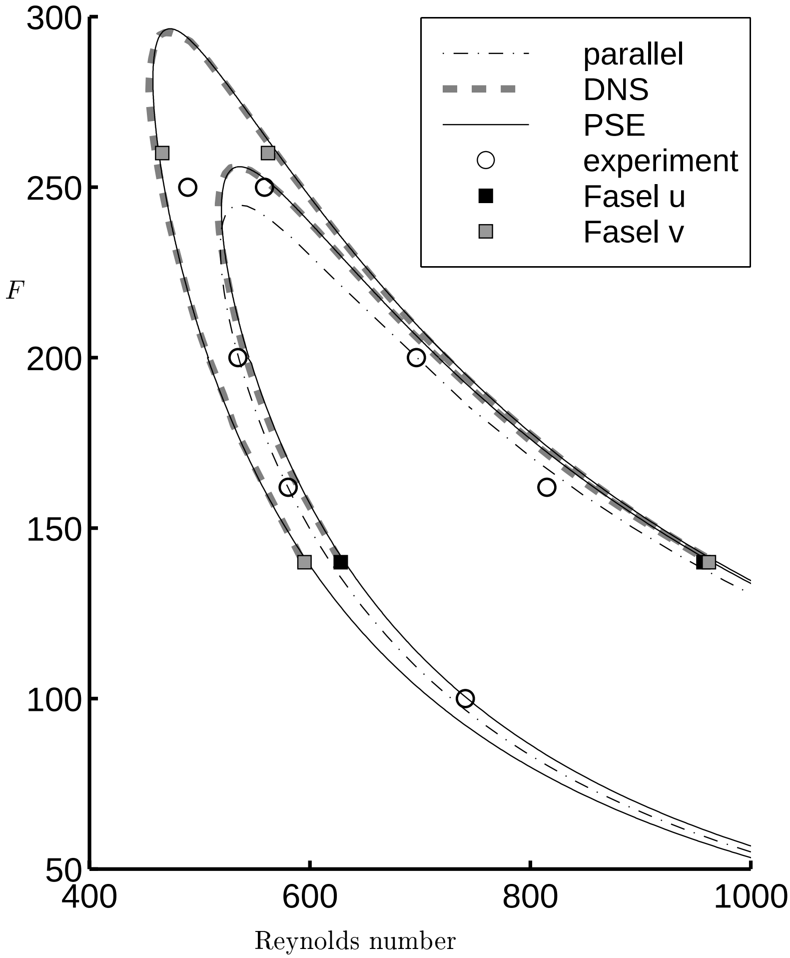

FIGURE 5.1 Neutral stability curves for non-parallel boundary layer, grey dashed curve: DNS, solid: PSE. The outer curves represent maximum fo v and the inner maximum of u. DNS results by Fasel & Konzelmann (1990) are represented by squares, grey: maximum of u and black maximum of u. Experimental data are represented by circles.

CHAPTER 6

Oblique transition

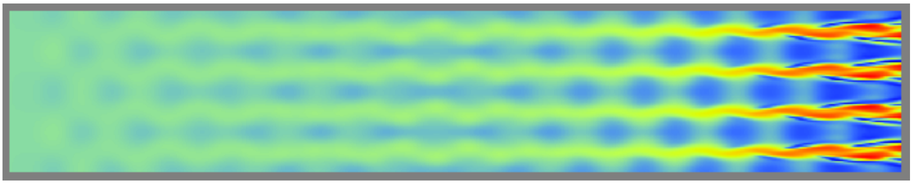

FIGURE 6.1 Oblique waves at the inflow (left) are seen to cause streak growth. Low streamwise velocity is represented by dark blue it increases over green and yellow to red representing the highest velocity.

Two oblique waves, with opposite wave angle, present in a laminar boundary layer may cause oblique transition. The streamwise disturbance velocity from a simulation of oblique transition is displayed in figure 6.1, where the flow is from left to right and low velocities are represented by dark blue. The velocity then increases over green and yellow to red representing the highest velocity. The checked standing wave pattern produced by the oblique waves can be observed in the left inflow region. Note that there are two spanwise wave lengths included in the figure. As the oblique waves slowly decay in the background, streamwise streaks can be seen to grow and become the dominant flow structure at the outflow. There we clearly see four streaks, which means that the wavenumber is twice that at the inflow. This change of scale can only be caused by nonlinear interaction of the involved disturbance modes.

Oblique waves are found to nonlinearly generate streamwise vortices in the boundary layer and the streamwise vortices force the growth of the streaks by the lift-up effect. This is a powerful process, which cause large amplitude streaks even if the vortices are generally week and decay after the first nonlinear generation. As the vortices are stationary we can study them by observing the mean values of the disturbance velocities. The vectors in figure 6.2 shows the direction and the amplitude of the disturbance velocities in a plane perpendicular to the flow. Four centers of rotation belonging to two pairs of counter rotating vortices can be identified. In the center of the figure, vectors are pointing up and fluid with low streamwise velocity is lifted upwards causing a negative streamwise velocity disturbance. That is indicated by the dark shading and the brighter patches indicate an increased streamwise velocity where the vectors are pointing down.

Whether or not transition from laminar to turbulent flow occurs depends on the final strength of the streaks. Due to the non-linearity their amplitude scale quadratically with the initial amplitude of the oblique waves. A doubled

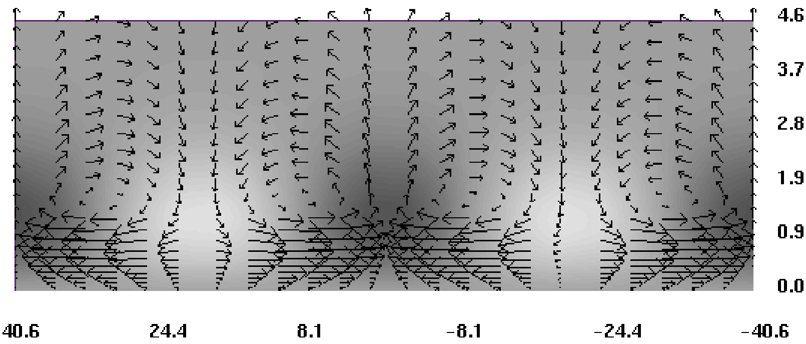

FIGURE 6.2 The vectors shows the direction and amplitude of the mean disturbance flow in a plane perpendicular to the flow direction. Dark shading represent negative streamwise velocity disturbance and white shading positive.

amplitude of the oblique waves means four times stronger vortices and forcing of the streaks. It is when the streaks reach a threshold amplitude that other disturbances start to grow and the flow breaks down to a turbulent state. Decay of the streaks will otherwise be observed after they reach a maximum, and the flow will remain laminar.

In figure 6.3 the energy of the most important disturbance modes are shown during the process of oblique transition. The energy has in the figure been normalized by the initial energy of the oblique waves $(1,1)$, which therefore is 1 at the inflow where they are the only present disturbance. The initial energy of the oblique waves have in this simulation been chosen to just push the streaks over the threshold amplitude for transition to occur. The streak mode $(0,2)$ is generated and grows rapidly to $x = 100$ and when it reaches its maximum at

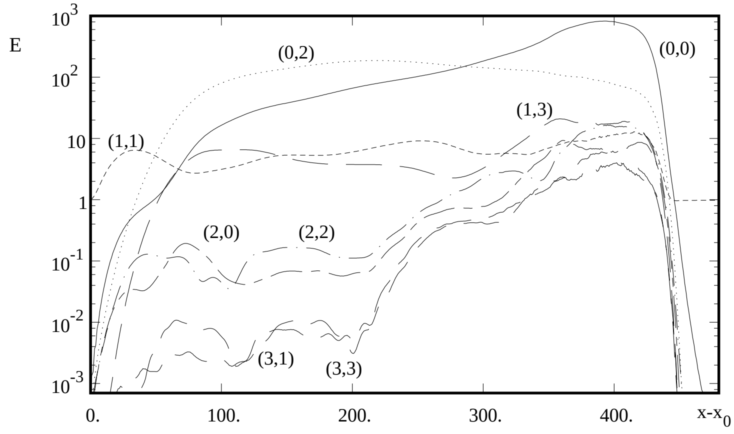

FIGURE 6.3 Energy in Fourier components with frequency and spanwise wavenumber $(\omega/\omega_0, \beta/\beta_0)$ as shown. The curves are normalized such that the energy of the (1,1) mode at inflow is set to unity.

$x = 200$ the modes with lower energy suddenly starts to grow. Those modes were also generated nonlinearly but did not have the same potential of initial growth as the $(0, 2)$ mode. Recall that the non-modal theory predicts large sensitivity to forcing of modes with zero streamwise wavenumber. The results in figure 6.3 are obtained from a simulation that was fully turbulent at $x = 400$ (see paper 2) and was computed for a very low Reynolds number, $R = 400$ at the inflow. A subcritical Reynolds number at which no exponentially growing mode exists. The total disturbance growth seen in this simulation is due to non-modal growth effects, which cause growth at much lower Reynolds numbers than the TS-mechanism.

The first experimental results of oblique transition in boundary layer flow was presented by Wiegel (1996) and a comparison is obviously interesting. Even a carefully built experiment will differ from the mathematical precision of a numerical simulation. The mean flow in a windtunnel will contain disturbances at some level, pressure variations at the leading edge will effect the flow and the generation of the desired disturbances may not be ideal. All these effects influence the transition scenario and are normally unknown to the numerical investigator. After verifying that the qualitative aspects of the oblique transition scenario was the same in the simulations and the experiment by Wiegel (1996), we investigated how the transition scenario was effected by changes in the oblique wave generation and streamwise pressure gradient. Imposing an adverse pressure gradient (increasing pressure with downstream distance) was found to shift all stages of the transition scenario upstream and changes in the generation method for oblique waves primarily altered the amplitude and phase relation between the individual modes of the generated disturbance. When a blowing and suction technique, closely modeling the device used in the experiment by Wiegel (1996), was used in the simulation it was shown that not only were oblique waves $(1, \pm 1)$ generated but also higher spanwise harmonics like $(1, \pm 5)$.

The experimental disturbance generator was closely modeled in a simulation and a pressure variation added to give the same initial growth of the oblique waves as in the experiment. This led to good agreement for u_{rms} to $x = 320$ (mm) and for the streak amplitude to $x = 340$ (mm), which is displayed in figure 6.4. Further downstream the pressure gradient cause earlier transition in the simulation. A comparison of the late stages of the transition process was, however, possible by choosing downstream positions with equal u_{rms} maxima and the agreement was then still found to be good, thanks to the close modeling of the disturbance generator. Figure 6.5 shows the spanwise variation of both the streamwise mean velocity and the streamwise fluctuations from such a comparison. Note that the peaks of u_{rms} are found at the spanwise position where $\bar{u}$ has its steepest spanwise gradient.

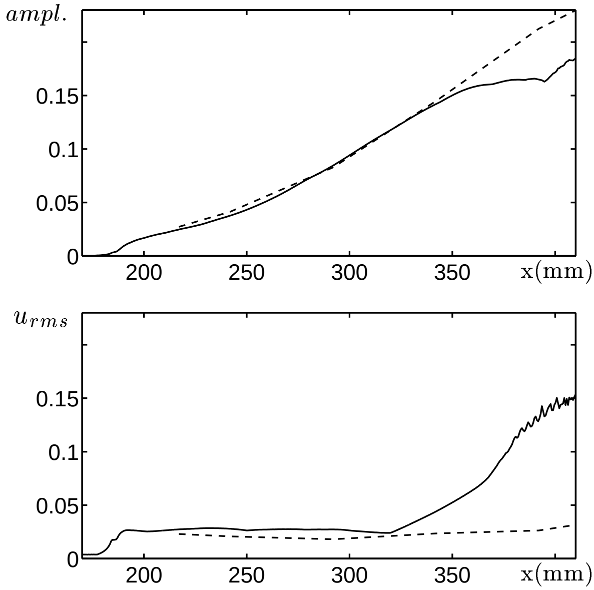

FIGURE 6.4 (*a*) streak amplitude (*b*) u_{rms} of experiment (solid) and simulation (dashed) with closely modeled generation mechanism and pressure gradient to match initial u_{rms} development.

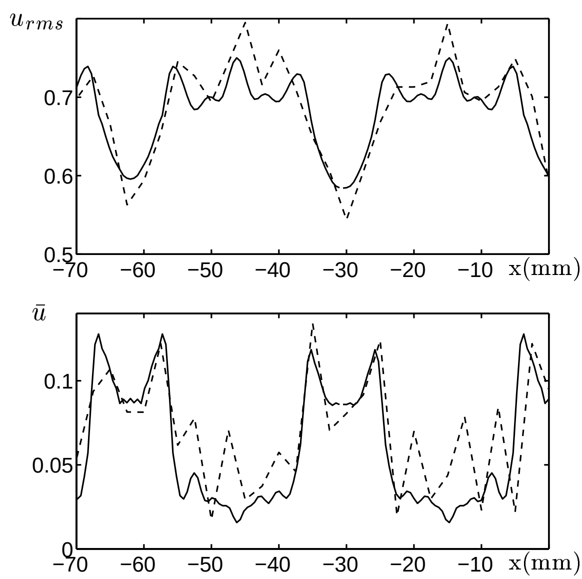

FIGURE 6.5 Spanwise variation of $\bar{u}$ (left) and u_{rms} (right) of simulation closely modeled generation device (solid) and experiment (dashed). Because of the earlier transition in simulation, downstream positions were chosen to get equal maximum of u_{rms}. The downstream positions were $x = 391$ in the simulation and $x = 514$ in the experiment.

Before the flow reaches a fully turbulent state Λ-shaped structures consisting of pairs of streamwise counter rotating vortices are formed. The front parts of the vortices are lifted towards the free-stream and their tips are drawn towards each other. These Λ-vortices are much stronger than the mean vortices causing the streak growth and one is displayed in figure 6.6, where blue and yellow surfaces represent constant negative and positive streamwise vorticity, respectively. On the outside of the vorticity surfaces the disturbance flow is directed downward, whereas there is a upward motion between them. The lift-up of slow streamwise velocity between the vortices causes strong gradients in the streamwise velocity, which is shown as a green surface of constant $\partial u/\partial y$ in the figure. Λ-vortices are closely associated with the final breakdown. Inflectional velocity profiles are found in the Λ-vortices and the first large velocity fluctuations and high u_{rms} values are first detected in their vicinity. This is the same region where the strongest spanwise shear is located, which is consistent with what is observed in figure 6.5

The structures found in the late stage of oblique transition are very similar to those of the nonlinear stages in the transition scenarios initiated by TS-waves. We mentioned in §3.1.2 that they were characterized by different patterns of Λ-vortices. The secondary instability, which leads to three-dimensionality in the TS transition scenarios, generates both oblique waves and streamwise vortices, which we have shown to be the important components in oblique transition, and the similarities are therefore not very surprising. Flow visualizations of the three scenarios are shown in figure 6.7 and both streakyness and the dark blue Λ-patches can be seen in for all cases, with varying relation between the two disturbance types. TS-waves are not observed, which is in agreement with the results in literature showing that the energy in the oblique waves and streamwise streaks are larger than the TS-wave at late TS transition stages. Non-modal effects may also be involved in the strong streak growth observed in TS transition. The similarities between TS-breakdown and oblique breakdown are many but a very important difference is that no TS-wave is needed or present in oblique transition. Oblique waves are however needed in TS secondary instability transition.

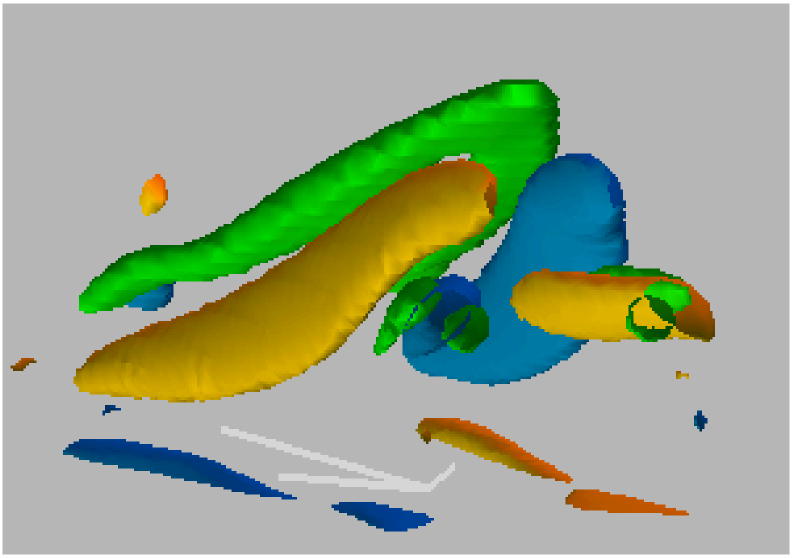

FIGURE 6.6 Positive (yellow) and negative (blue) isosurfaces of streamwise vorticity in a Λ-vortex together with the associated high streamwise shear-layer (green). The black arrow at the wall marks the direction of the mean flow.

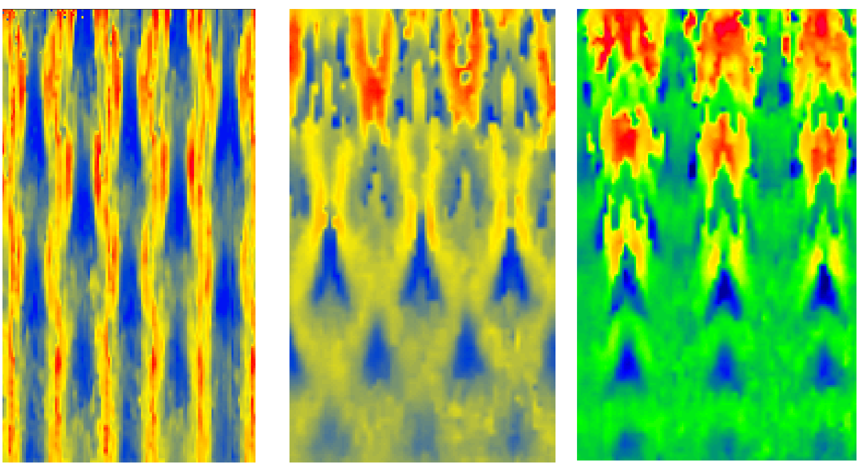

FIGURE 6.7 PIV pictures from three transition scenarios, from left to right: oblique transition, H-type transition and K-type transition. The flow direction is from the bottom to top of the figures. Both Λ-shapes and streaks can be observed in all three scenarios.

CHAPTER 7

Receptivity to oblique waves

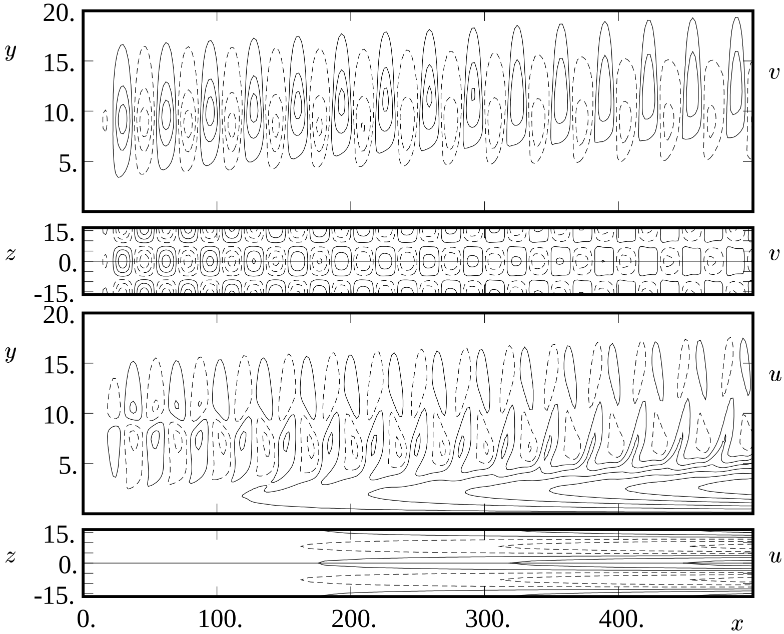

FIGURE 7.1 Contours of velocity from spatial simulation with oblique waves in the free-stream. Top: v at $z = 0$, spacing 0.005, Second: v at $y = 9$, spacing 0.005, Third: u at $z = 0$, spacing 0.0075, Bottom: u at $y = 2$, spacing 0.025.

Oblique waves was found to cause rapid transition and it is interesting to investigate their role in the receptivity process. In addition, the growth of streamwise streaks has been found to be the dominant feature of both oblique transition and transition caused by free-stream turbulence. Oblique waves were therefore generated in the free-stream above the boundary layer in a spatial simulation and the downstream development is shown in figure 7.1. The two top figures contain contours of the wall normal disturbance velocity v in planes perpendicular and parallel to the wall. The second frame from the top contains a wall parallel plane selected at $y = 9.0$. It shows the typical chequered disturbance pattern produced by two oblique waves and that the wave amplitude decreases downstream. The downstream decay is also seen in the perpendicular symmetry plane $z = 0$, from which it is clear that the main part of the oblique disturbances remain in the free-stream. Contours of the streamwise disturbance velocity u is displayed in

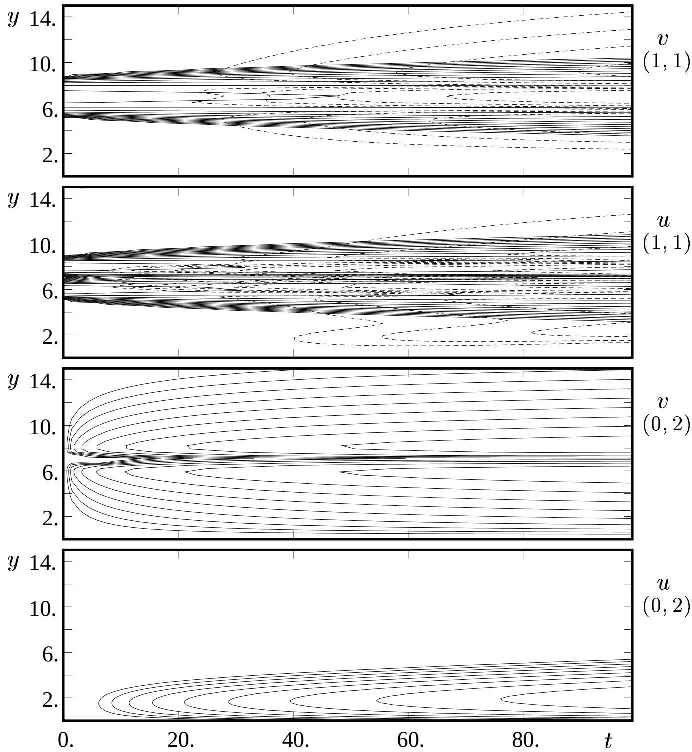

FIGURE 7.2 Logarithmic contours of energy starting at $1 \cdot 10^{-12}$, where two contours represent an increase with a factor of 10. Top: v in the $(1,1)$ mode. Solid represents the linear part and dashed the cubicly generated part, Second: u in the $(1,1)$ mode. Solid represents the linear part and dashed the cubicly generated part,Third: v in the quadratically generated $(0,2)$ mode, Bottom: u in the quadratically generated $(0,2)$ mode. Note how the $(0,2)$ mode is nonlinearly generated in the hole domain and itself generates growing streaks.

the two bottom frames of figure 7.1. The perpendicular plane is $z = 0$ and we can again see the downstream decay in the free-stream, but also disturbance growth inside the boundary layer. A wall parallel plane inside the boundary layer at $y = 2$ reveals growing streamwise streaks with half the spanwise wavelength of the initially generated oblique waves. These streaks are forced through a nonlinear mechanism and their growth is due to linear non-modal mechanisms.

Temporal simulations were used in a thorough investigation of the the nonlinear mechanism and how it is influenced by changes in disturbance characteristics.

By studying the energy in the velocity components as function of both time and the wall normal coordinate the new non-linear mechanism can be understood. The first and the second frame from the top in figure 7.2 shows the energy in v and u respectively, for an oblique wave. We have separated the parts of $(1,1)$ that have a linear (solid) and cubic (dashed) dependence on the energy in the initial disturbance. Quadratic dependence on the initial disturbance is found for the main nonlinearly generated mode $(0,2)$ and higher order terms are negligible at the low amplitudes we have used. The linear part of the oblique waves, both u and v, diffuses slowly and decays rapidly with time. The cubicly generated part is seen to be more spread out vertically. In the second frame from the bottom we display the v component of the $(0,2)$ mode, which is rapidly generated by the non-linearities in a large wall-normal domain. It is not damped and only slightly affected by the boundary layer and the wall. The v component is associated with vortices that immediately interact with the shear in the boundary layer to form streaks. This is observed as growing energy in the u component inside the boundary layer in the bottom frame.

The same study of the initial receptivity was also done for two other types of free-stream disturbances. No strong growth was found when the initial disturbance was a two-dimensional wave. When streamwise vortices $(0,1)$ were initiated in the free-stream the nonlinear mechanism worked as for oblique waves and the $(0,2)$ mode grew in the boundary layer. In addition the $(0,1)$ vortices slowly diffused into the boundary layer and also caused strong streak growth.

In figure 7.3 we compare the continued development of the oblique waves and the streamwise vortices, and the corresponding non-linearly generated modes (curves with additional markers). The oblique waves (solid) decay. The vortex/streak $(0,2)$ mode (solid with markers), nonlinearly generated by the oblique waves, grows substantially until its maximum is reached shortly before $t = 1000$. The disturbance development caused by the initial generation of the vortex/streak mode $(0,1)$ (dashed) shows a significant difference from the initiated oblique waves after $t = 200$. At that time the initially generated vortices have diffused deep enough into the boundary layer to cause streak growth. The $(0,2)$ mode, non-linearly generated by the initiated $(0,1)$, also grows and is up to $t = 450$ actually slightly larger than the $(0,1)$ mode for this initial energy, which corresponds to a v_{rms} of about 1%.

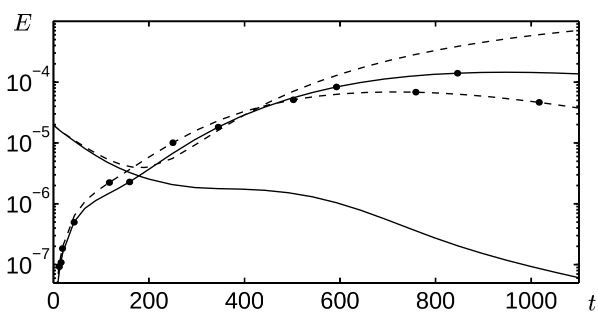

FIGURE 7.3 Long behavior of the energy for two disturbance types, initiated with the same energy in the free-stream. Solid: oblique waves, dashed: streamwise vortices. Curves representing non-linearly generated modes are marked with dots.

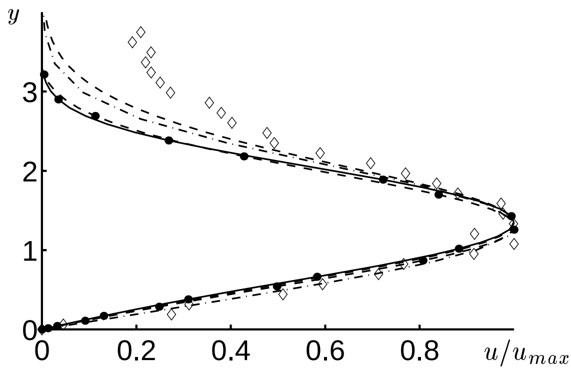

FIGURE 7.4 Wall normal mode shape in the u-component of growing streaks. Solid with marker: $(0, 2)$ mode generated by oblique free-stream waves, dashed: $(0, 1)$ initiated in the free-stream, dashed with marker: $(0, 2)$ mode generated by streamwise vortices in the free-stream and diamonds: u_{rms} distribution from experiment by Westin *et al.* (1994) $R = 890$.

The wall normal mode shape in the u component of the three growing streak modes previously discussed are plotted figure 7.4. The shape of what is commonly referred to as a Klebanoff mode is found for all three cases, with the linear mode reaching slightly further into the free-stream. The original Klebanoff mode is the wall normal variation of u_{rms} in experiments with free-stream turbulence and we have included experimental data from Westin *et al.* (1994) in the figure. The fluctuations found in the experiment are caused by the random oscillations of the dominant streaks and the agreement in mode shape between the streak modes and u_{rms} is therefore natural. A consequence of the free-stream turbulence in the experiments are that u_{rms} does not go to zero in the free-stream and whether the experimental mode is associated with the linear or the nonlinear mode shape or both can not be determined.

The growth of the quadratically generated streaks depends on the initial disturbance characteristics and we have investigated both the dependence on the wavenumbers α and β and the wall normal disturbance distribution. Changes of α had the smallest effect on the growth and the optimal α was close to zero. The best β for the free-stream disturbance depends on α and lies in the interval $0.2 < \beta < 0.35$ and the selectivity for a specific β within that interval was not found to be very strong. Note that the nonlinear generation results in streaks with β between 0.4 and 0.7. The wall normal velocity component was found to be important and redistribution of disturbance energy from the streamwise velocity component to the wall normal increased the streak growth, under the condition that the spanwise and wall normal size of the generated streamwise vortex were comparable.

The importance of the wall normal velocity component in the receptivity process was also shown in the numerical experiments by Yang & Voke (1993). Westin *et al.* (1994) examined experimental data on the streamwise velocity component reported in literature and could not find a correlation between turbulence level, streak amplitude and transitional Reynolds number. There is unfortunately a great lack of experimental information concerning the wall normal velocity component, such data could explain observation and improve transition prediction models.

An important feature of the new nonlinear receptivity mechanism is that it can cause streak growth from both oblique disturbances and streamwise vortices. We have studied receptivity mechanism that continuously interact with the boundary layer, whereas many previous investigators considers the receptivity to take place at the leading edge. A continuous forcing of streaks could explain the discrepancy in the growth rate between those calculations and experimental findings. It could also, from a spectra of scales in the free-stream contribute to the downstream increase of the spanwise streak scale found in experiments.

CHAPTER 8

Control of oblique transition

The mechanisms behind oblique transition and the associated streak breakdown are now known and also that they are a potential cause of rapid transition. A natural next step is to investigate the possibilities of controlling oblique transition.

We used two methods to generate a oscillating spanwise flow in order to delay oblique transition. The first was the use of a oscillating spanwise body force that decayed exponentially away from the boundary layer wall. Gailitis & Lielausis (1961) showed that periodically distributed magnetic fields and electric currents can generated such a force (Tsinober 1989) and we assume that the force is given by

$$F_z = f_0 e^{-y/c} \cos(\omega t), \tag{6}$$

where f_0 is an amplitude, ω the oscillation frequency and c a parameter controlling the wall normal decay. We will use the triplet (f_0, c, ω) to refer to these force parameters. The force itself is not significant for the control but rather the spanwise flow that it causes, which has the form

$$w(y, c, \omega) = A\sqrt{e^{-2\gamma y} + e^{-2y/c} - 2\cos(\gamma y)e^{-(\gamma+1/c)y}} \tag{7}$$

where

$$A = \sqrt{\frac{(f_0 R)^2 c^4}{1 + (\omega R)^2 c^4}}, \quad \gamma = \sqrt{\frac{\omega R}{2}} \tag{8}$$

The expressions (8) reveal that a change of the oscillation frequency or the decay parameter c will effect both amplitude and wall normal distribution of the spanwise flow. To study the effects of changes in the spanwise flow profile several parameters often have to be adjusted at the same time.

The other method of generating a spanwise oscillating flow was to oscillate the wall. The expression for w is then

$$w = Ce^{-\gamma y} \cos(\gamma y), \tag{9}$$

where γ is given above and C is the amplitude.

For both control strategies we found that the achieved transition delay increased with spanwise flow amplitude to an optimal value of 50-60% of the streamwise free stream velocity. The transition delay was less if the spanwise flow amplitude was raised above that value. The body force was more successful in delaying transition and the maximum delay found for our case was 35%, whereas

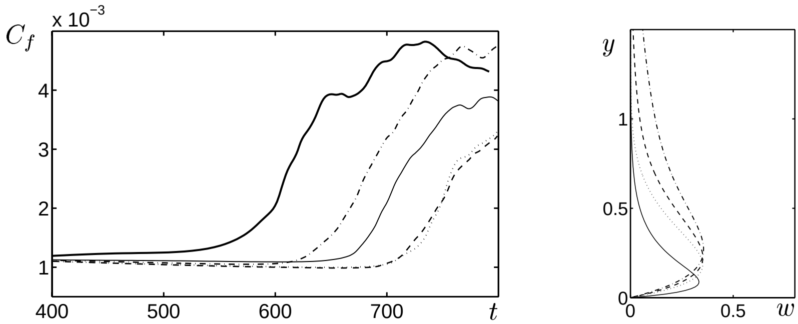

FIGURE 8.1 Left: coefficient of friction Right: oscillating spanwise flow profiles, for force parameters $(0.43, 0.05, 0.09)$ (solid), $(0.086, 0.22, 0.09)$ (doted), $(0.060, 0.38, 0.09)$ (dashed) and $(0.046, 0.7, 0.09)$ (dash-doted). The thick curve in the left figure represents the uncontrolled case.

the oscillating wall could only delay transition with 15%. The explanation for this can be found by studying the wall normal profile of the control flow. The transition time was taken as the instant when the wall friction reached 1.7 times the laminar value.

In the left frame of figure 8.1 the friction coefficient is plotted as a function of time for four control cases together with a thicker curve representing the case without control. The body force was in the controlled cases adjusted to produce different wall normal profiles of the spanwise oscillating flow. The profiles are found in the right frame of figure 8.1. The two middle flow profiles perform best. The transition delay is less if the spanwise flow is concentrated close to the wall or a too large wall normal proportion of the boundary layer is oscillating. The purpose of the control is to break the flow structures causing transition, and one may interpret these results in the following manner. If the whole structure is moved (the highest flow profile) or if the relevant structures not affected (the lowest profile), they will not be destroyed by the spanwise flow oscillations and therefor the resulting transition delay will be less. It is natural that the oscillating wall achieves less transition delay, as its profile has its maximum at the wall.

The optimal oscillation frequency of the oscillations was found to be in the range $0.09 < \omega < 0.17$ for the body force and slightly lower for the moving wall.

For comparison the discussed control strategies were also applied to a case where the energy of the initial disturbance causing transition was randomly distributed. The total energy was then twice that of the oblique waves in order to cause transition at approximately the same time.

The observed transition scenario was also found to be characterized by streaky structures, but of smaller spanwise scale. That scenario was considerably easier to effect by the flow oscillations and both the body force and the oscillating wall could prevent transition. The optimal oscillation frequency and also the best wall normal profiles for the spanwise flow were the same as for oblique transition. This indicates that our results my be generally true for transition dominated by streamwise streaks and not only applicable to the particular case of oblique transition we have concentrated our study on.

Bibliography

AKHAVAN, R., JUNG, W. J. & MANGLIAVACCHI, N. 1993. Turbulence control in wall-bounded flows by spanwise oscillations. *Applied Scientific Research.* **51**, 299–303.

ANDERSSON, P., BERGGREN, M. & HENNINGSON, D. 1997. Optimal disturbances in boundary layers. In *Progress in Systems Control.* Birkhäuser.

ANDERSSON, P., BERGGREN, M. & HENNINGSON, D. 1998. Optimal disturbances and bypass transition in boundary layers. *Phys. Fluids.* . (Submitted).

BERTOLOTTI, F. P. 1997. Response of the blasius boundary layer to free-stream vorticity. *Phys. Fluids.* **9** (8), 2286–2299.

BERTOLOTTI, F. P., HERBERT, T. & SPALART, P. R. 1992. Linear and nonlinear stability of the Blasius boundary layer. *J. Fluid Mech.* **242**, 441–474.

BOIKO, A. V., WESTIN, K. J. A., KLINGMANN, B. G. B., KOZLOV, V. V. & ALFREDSSON, P. H. 1994. Experiments in a boundary layer subject to free-stream turbulence. Part II: The role of TS-waves in the transition process. *J. Fluid Mech.* **281**, 219–245.

BUTER, T. A. & REED, H. L. 1994. Boundary layer receptivity to free-stream vorticity. *Phys. Fluids.* **6**, 3368–3379.

BUTLER, K. M. & FARRELL, B. F. 1992. Three-dimensional optimal perturbations in viscous shear flow. *Phys. Fluids A.* **4**, 1637–1650.

CHANG, C.-L. & MALIK, M. R. 1992. Oblique-mode breakdown and secondary instability in a supersonic boundary layers using nonlinear pse. In *Instability, Transition and Turbulence* (HUSSAINI, M. Y., KUMAR, A. & STREETT, C. L., editors), pp. 231–241. Springer-Verlag.

CHANG, C.-L. & MALIK, M. R. 1994. Oblique-mode breakdown and secondary instability in supersonic boundary layers. *J. Fluid Mech.* **273**, 323–360.

CHOI, H., MOIN, P. & KIM, J. 1993. Active turbulence control for drag reduction in wall-bounded flows. *J. Fluid Mech.* **262**, 75.

CHOUNDHARI, M., 1996. Boundary-layer receptivity to three-dimensional unsteady vortical disturbances in free stream. AIAA Paper 96-0181.

COOLEY, J. W. & TUKEY, J. W. 1965. An algorithm for the machine calculation of complex Fourier series. *Math. Comput.* **19**, 297–301.

CRAIK, A. D. D. 1971. Nonlinear resonant instability in boundary layers. *J. Fluid Mech.* **50**, 393–413.

DANABASOGLU, G., BIRINGEN, S. & L., S. C. 1991. Spatial simulation of instability by periodic suction blowing. *Phys. Fluids A.* **3** (9), 2138–2147.

ELLINGSEN, T. & PALM, E. 1975. Stability of linear flow. *Phys. Fluids.* **18**, 487–488.

ELOFSSON, P. A. & ALFREDSSON, P. H. 1995. Experiments on nonlinear interaction between oblique Tollmien-Schlichting waves. In *Laminar-Turbulent Transition*, pp. 465–472.

ELOFSSON, P. A. & ALFREDSSON, P. H. 1997. An experimental investigation of oblique transition in a Blasius boundary layer. In *EUROMECH Colloquium 359.*

ELOFSSON, P. A. & LUNDBLADH, A. 1994. Ribbon induced oblique transition in plane poiseulle flow. In *Bypass transition - proceedings from a mini-workshop* (HENNINGSON, D. S., editor), pp. 29–41. TRITA-MEK Technical Report 1994:14, Royal Institute of Technology, Stockholm, Sweden.

FASEL, H. & KONZELMANN, U. 1990. Non-parallel stability of a flat-plate boundary layer using the complete navier-stokes equations. *J. Fluid Mech.* **221**, 311–347.

FASEL, H. & THUMM, A. 1991. Direct numerical simulation of three-dimensional breakdown in supersonic boundary layer transition. *Bull. Am. Phys. Soc.* **36**, 2701.

FASEL, H., THUMM, A. & BESTEK, H. 1993. Direct numerical simulation of transition in supersonic boundary layers: Oblique breakdown. In *Transitional and turbulent compressible flows* (KRAL, L. & ZANG, T., editors), pp. 77–92.

GAD-EL HAK, M. 1989. Flow control. *Appl. Mech. Rev.* **42** (10), 261–293.

GAILITIS, A. K. & LIELAUSIS, O. A. 1961. On the possibility of drag reduction of a flat plate in an electrolyte. *Trudy Instituta Fisiky Akademii Nauk. Latviisky SSR.* **12**, 143–146. (in Russian).

GOLDSTEIN, M. E. & HULTGREN, L. S. 1989. Boundary-layer receptivity to long-wave free-stream disturbances. *Ann. Rev. Fluid Mech.* **21**, 137–166.

GUSTAVSSON, L. H. 1991. Energy growth of three-dimensional disturbances in plane Poiseuille flow. *J. Fluid Mech.* **224**, 241–260.

HANIFI, A., SCHMID, P. J. & HENNINGSON, D. S. 1996. Transient growth in compressible boundary layer flow. *Phys. Fluids.* **8**, 51–65.

HERBERT, T. 1983. Secondary instability of plane channel flow to subharmonic three-dimensional disturbances. *Phys. Fluids.* **26**, 871–874.

HERBERT, T. 1983. Subharmonic three-dimensional disturbances in unstable shear flows.

HERBERT, T. 1988. Secondary instability of boundary layers. *Ann. Rev. Fluid Mech.* **20**, 487–526.

JOSLIN, R. D., STREETT, C. L. & CHANG, C. L. 1992. Oblique wave breakdown in an incompressible boundary layer computed by spatial dns and pse theory. In *Instability, Transition and Turbulence* (HUSSAINI, M. Y., KUMAR, A. & STREETT, C. L., editors), pp. 304–310. Springer-Verlag.

JOSLIN, R. D., STREETT, C. L. & CHANG, C. L. 1993. Spatial direct numerical simulations of boundary-layer transition mechanisms: Validation of PSE theory. *Theoret. Comput. Fluid Dyn.* **4**, 271–288.

KACHANOV, Y. S. 1994. Physical mechanisms of laminar-boundary-layer transition. *Ann. Rev. Fluid Mech.* **26**, 411–482.

KACHANOV, Y. S., KOZLOV, V. & LEVCHENKO, V. Y. 1977. Nonlinear development of a wave in a boundary layer. *Izv. Akad. Nauk SSSR, Mekh. Zhidk. Gaza.* **3**, 49–53. (in Russian).

KELVIN, L. 1887. Stability of fluid motion - rectilinear motion of a viscous fluid between two parallel planes. *Philosophical Magazine.* **24**, 188–196.

KENDALL, J. M., 1985. Experimental study of disturbances produced in a pre-transitional laminar boundary layer by weak freestream turbulence. AIAA Paper 85-1695.

KENDALL, J. M., 1990. Boundary layer receptivity to freestream turbulence. AIAA Paper 90-1504.

KERSCHEN, E. J. 1990. Boundary layer receptivity theory. *Appl Mech Rev.* **43** (5, Part 2), S152–157.

KIM, J., MOIN, P. & MOSER, R. 1987. Turbulence statistics in fully developed channel flow. *J. Fluid Mech.* **177**, 133–166.

KLEBANOFF, P. S. 1971. Effect of freestream turbulence on the laminar boundary layer. *Bull. Am. Phys. Soc.* **10**, 1323.

KLEBANOFF, P. S., TIDSTROM, K. D. & SARGENT, L. M. 1962. The three-dimensional nature of boundary layer instability. *J. Fluid Mech.* **12**, 1–34.

KLEISER, L. & LAURIEN, E., 1985. Numerical investigation of interactive transition control. AIAA Paper 85-0566.

KLEISER, L. & ZANG, T. A. 1991. Numerical simulation of transition in wall-bounded shear flows. *Ann. Rev. Fluid Mech.* **23**, 495–537.

KLINGMANN, B. G. B., BOIKO, A., WESTIN, K., KOZLOV, V. & ALFREDSSON, P. 1993. Experiments on the stability of Tollmien-Schlichting waves. *Eur. J. Mech., B/Fluids.* **12**, 493–514.

KREISS, H.-O. & OLIGER, J. 1972. Comparison of accurate methods for the integration of hyperbolic equations. *Tellus.* **XXIV**, 199–215.

LANCOS, C. 1938. Trigonometric interpolation of empirical and analytical functions. *J. Math. Phys.* **17**, 123–199.

LIN, N., REED, H. L. & SARIC, W. S. 1992. Effect of leading-edge geometry on boundary-layer receptivity to freestream sound. In *Instability, Transition and Turbulence* (HUSSAINI, M. Y., KUMAR, A. & STREETT, C. L., editors), pp. 356–366. Springer-Verlag.

LU, Q. & HENNINGSON, D. S. 1990. Subcritical transition in plane Poiseuille flow. *Bull. Am. Phys. Soc.* **35**, 2288.

LUCHINI, P. 1996. Reynolds number independent instability of the Blasius boundary layer over a flat surface. *J. Fluid Mech.* **327**, 101–115.

LUCHINI, P. 1997. Reynolds number independent instability of the Blasius boundary layer over a flat surface. part 2: optimal pertubations. Submitted to jfm.

LUNDBLADH, A., HENNINGSON, D. S. & JOHANSSON, A. V., 1992. An efficient spectral integration method for the solution of the Navier-Stokes equations. FFA-TN 1992-28, Aeronautical Research Institute of Sweden, Bromma.

MALIK, M. R., ZANG, T. A. & HUSSAINI, M. Y. 1985. A spectral collocation method for the Navier-Stokes equations. *J. Comp. Phys.* **61**, 64–88.

MORKOVIN, M. V. 1969. The many faces of transition. In *Viscous Drag Reduction* (WELLS, C. S., editor). Plenum Press.

NISHIOKA, M. & V., M. M. 1986. Boundary-layer receptivity to unsteady pressure gradients: experiment and overview. *J. Fluid Mech.* **171**, 219–261.

ORR, W. M. F. 1907. The stability or instability of the steady motions of a perfect liquid and of a viscous liquid. Part I: A perfect liquid. Part II: A viscous liquid. *Proc. R. Irish Acad. A.* **27**, 9–138.

ORSZAG, S. A. 1972. Comparison of pseudospectral ans spectral approximations. *Stud. Appl. Math.* **51**, 253–259.

ORSZAG, S. A. & PATERA, A. T. 1983. Secondary instability of wall-bounded shear flows. *J. Fluid Mech.* **128**, 347–385.

REDDY, S. C. & HENNINGSON, D. S. 1993. Energy growth in viscous channel flows. *J. Fluid Mech.* **252**, 209–238.

REDDY, S. C., SCHMID, P. J., BAGGET, J. S. & HENNINGSON, D. S., 1997. On stability of streamwise streaks and transition thresholds in plane channel flow. submitted to jfm.

RIST, U. & FASEL, H. 1995. Direct numerical simulation of controlled transition in a flat-plate boundary layer. *J. Fluid Mech.* **298**, 211–248.

SANDHAM, N. D., ADAMS, N. A. & KLEISER, L., 1994. Direct simulation of breakdown to turbulence following oblique instability waves in a supersonic boundary layer. First ERCOFTAC workshop on direct and large eddy simulation, Guildford, England, March 28-30.

SCHLICHTING, H., 1933. Zur Entstehung der Turbulenz bei der Plattenströmung. Nachr. Ges. Wiss. Göttingen, 181–208.

SCHMID, P. J. & HENNINGSON, D. S. 1992. Channel flow transition induced by a pair of oblique waves. In *Instability, Transition and Turbulence* (HUSSAINI, M. Y., KUMAR, A. & STREETT, C. L., editors), pp. 356–366. Springer-Verlag.

SCHMID, P. J., REDDY, S. C. & HENNINGSON, D. S. 1996. Transition thresholds in boundary layer and channel flow. In *Advances in Turbulence VI* (GAVRILAKIS, S., MACHIELS, L. & MONKEWITZ, P. A., editors), pp. 381–384. Kluwer Academic Publishers.

SCHUBAUER, G. B. & SKRAMSTAD, H. F. 1947. Laminar boundary layer oscillations and the stability of laminar flow. *J. Aero. Sci.* **14**, 69–78.

THOMAS, A. S. 1983. The control of boundary-layer transition using a wave superposition principle. *J. Fluid Mech.* **137**, 233–250.

TOLLMIEN, W., 1929. Über die Entstehung der Turbulenz. Nachr. Ges. Wiss. Göttingen, 21–44. (English translation NACA TM 609, 1931).

TREFETHEN, L. N., TREFETHEN, A. E., REDDY, S. C. & DRISCOLL, T. A. 1993. Hydrodynamic stability without eigenvalues. *Science.* **261**, 578–584.

TSINOBER, A. 1989. Mhd flow drag reduction. In *Viscous Drag Reduction in Boundary Layers*, volume 123, pp. 327–349. Progress in Astronautics and Aeronautics, American Institute of Aeronotical and Astronautics, Inc.

WESTIN, K. J. A., BOIKO, A. V., KLINGMANN, B. G. B., KOZLOV, V. V. & ALFREDSSON, P. H. 1994. Experiments in a boundary layer subject to free-stream turbulence. Part I: Boundary layer structure and receptivity. *J. Fluid Mech.* **281**, 193–218.

WIEGEL, M. 1996. *Experimentelle Untersuchung von kontrolliert angeregten dreidimensionalen Wellen in einer Blasius-Grenzschicht.* PhD thesis, Der Fakultät für Maschinenwesen der Universität Hannover, Hannover (Germany). Also available as VDI Fortschritt-Bericht Reihe 7, Vol 312, 1997.

YANG, Z. Y. & VOKE, P. R. 1993. Large-eddy simulation of transition under turbulence. Technical Report ME-FD/93.12, University of Surrey, Dept. Mech. Eng.

Paper 1

THE NEUTRAL STABILITY CURVE FOR NON-PARALLEL BOUNDARY LAYER FLOW

S. Berlin
Dept. of Mech., KTH, S-10044 Stockholm, Sweden

A. Hanifi
FFA, Box 11021, S-16111 Bromma, Sweden

D. S. Henningson
FFA, Box 11021, S-16111 Bromma, Sweden

Abstract. The complete neutral stability curve for non-parallel boundary layer flow is presented. The results are produced by both carefully performed DNS and PSE calculations, that are in excellent agreement. Agreement is also found with the few points on the neutral stability curve that have been reported previously and with the latest experiments. Based on the displacement thickness and the free-stream velocity the critical Reynolds number for growth of u and v in non-parallel boundary layer flow is determined to $R_{crit-u} = 518$ and $R_{crit-v} = 456$, respectively.

Traditional stability theory for Blasius boundary layers are based on the assumption of a locally wall parallel flow. Large discrepancies in the points of neutral stability determined in experiments, to the theoretical predictions, has often been considered as non-parallel effects. Several investigators has proposed theories that include non-parallel effects. Fasel & Konzelmann (1990) examined the non-parallel theories and compared them to both experiments and spatial direct numerical simulations (DNS). They simulated Tollmien-Schlichting (TS) waves with four different frequencies and found Gaster's (1974) theory to agree well with their calculations and the non-parallel effects to be comparatively small. They concluded that the large discrepancies in experiments were not caused by non-parallel effects. The same was found by Bertolotti, Herbert & Spalart (1992), who simulated two frequencies with DNS and calculated the neutral stability curve for non-parallel flow with parabolized stability equations (PSE). By carefully designing the leading edge to avoid pressure gradients and controlling the pressure gradient along their experimental boundary layer, Klingmann *et al.* (1993) obtained neutral points that agreed well with theory and calculations.

The aim of the present investigation has been to determine the complete neutral stability curves and the critical Reynolds numbers based on both the wall normal as well as the streamwise velocity components, in zero-pressure gradient, incompressible, non-parallel boundary layer flow. To our knowledge, such results based on DNS calculations has not been presented before. We also compare them with our PSE results and results of previous investigators.

The DNS program (1992, 1994) uses Fourier-Chebyshev spectral methods, similar to those of Kim, Moin & Moser (1987). To combine a spatially growing boundary layer, with periodic boundary condition in the streamwise direction, a "fringe region", similar to that described by Bertolotti, Herbert & Spalart

(1992) is used. In the fringe region, a forcing term is added to the Navier-Stokes equations, that eliminates disturbances flowing out of the box and returns the flow to its laminar inflow state. The studied TS-waves were generated by a body force applied in the boundary layer a short distance from the inflow.

The nonlocal stability calculations (based on PSE methodic) are performed using the NOLOT code, for description see Hanifi *et al.* (1994). The normal derivatives are approximated by a fourth-order compact difference scheme. The stability equations are integrated in the streamwise direction using a first-order backward Euler scheme. The stability calculations are started far upstream of the first branch of the neutral curve using the eigenvalues and eigenvectors from local theory as the initial conditions.

An instantaneous flow field from the DNS will register the maximum amplitude of the downstream traveling TS-wave at only a few locations separated by a half TS-wavelength. By Fourier transforming several consecutive flow fields in time, the amplitude variation in both the streamwise and wall normal direction can be found. In figure 1 both the streamwise u and the wall normal velocity v of a TS-wave is plotted as function of Reynolds number and wall normal position. The non-dimensional frequency of the TS-wave is $F = 220$, where $F = 2\pi f \nu / U_\infty^2 \times 10^6$, f the dimensional frequency, U_∞ the free-stream velocity and ν the kinematic viscosity. The Reynolds number is defined as $R = U_\infty \delta^* / \nu$, where δ^* is the displacement thickness. We have used the displacement thickness at $R = 300$ to non-dimensionalize the wall normal coordinate in figure 1. The amplitude in both velocity components are seen to first decay as R increases and then grow as the wave reaches the unstable Reynolds number region, to finally decay again when that region ends.

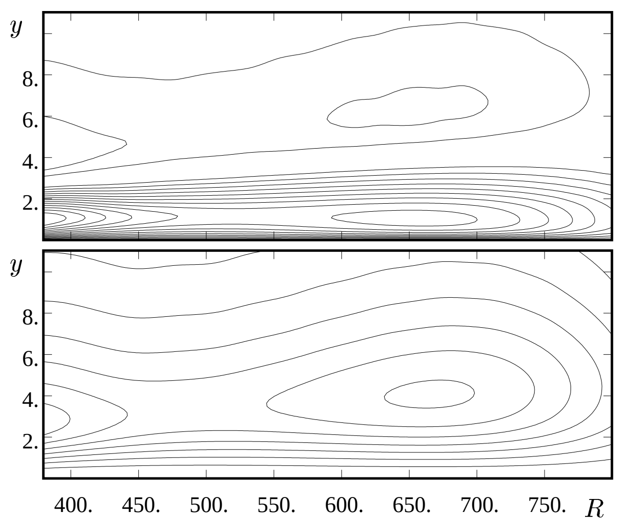

FIGURE 1. Contours of the amplitude in a TS-wave with non-dimensional frequency F=220. Top: u component first contour value $1.5 \cdot 10^{-5}$ and spacing $9 \cdot 10^{-6}$; Bottom: v component, first contour value $5 \cdot 10^{-6}$ and spacing $5 \cdot 10^{-6}$

When a TS-wave develops downstream, not only does its amplitude change, but also the wall normal mode shape. u has two maxima in the wall normal direction and v one and they are not found at a constant wall normal position, even if the wall normal coordinate is scaled with displacement thickness, as in figure 1. The growth rate and the neutral points with zero growth depends on what flow quantity is studied and how that quantity is followed downstream, something clearly demonstrated by Fasel & Konzelmann (1990). Following a wall normal maxima downstream gives a result that cannot be misleading and is well suited for comparison with both theory and experiments. We have followed the lower/inner maxima of u and the single maxima of v, when evaluating the growth and neutral points in our calculations.

The disturbance generation in the DNS will not only generate a TS-wave but also other modes at low amplitude. That can be seen in figure 1 as slight oscillations in some of the contours. We have minimized the level of other disturbance modes by careful modeling of the disturbance generation and did not, as Fasel & Konzelmann (1990) did, have to use any smoothing in the evaluations of the DNS results. Oscillations in the growth rate was also noted by Bertolotti *et al.* (1992) when they perturbed the initial eigenmode in their PSE calculations. The oscillations influenced the results further downstream for higher frequency eigenmodes.

A better view of the wall normal amplitude variation of the TS-waves u-component is given in figure 2. It displays normalized values measured by Klingmann *et al.* (1993) for $F = 250$ and $R = 574$ and the corresponding curves from DNS and PSE. The calculations are in perfect agreement and the experimental points follow the calculations well up to the outer maxima. As the amplitude of the inner maxima is three times larger than the outer and the mean flow component is lower close to the wall, the inner maxima should be easier to determine experimentally. Thus, the growth of the inner maximum is an appropriate choice

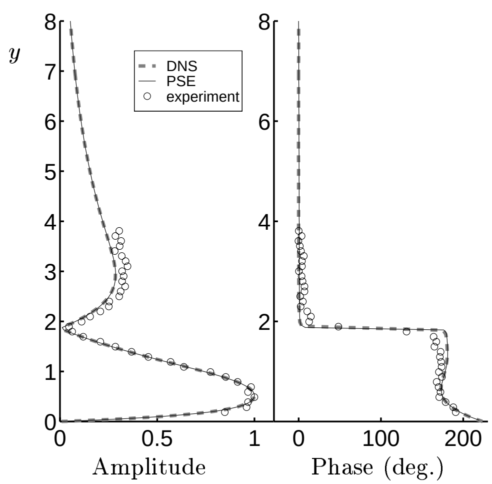

FIGURE 2. Amplitude (left) and phase (right) of TS-wave with $F = 250$ at $R = 574$, grey dashes: DNS, solid: PSE, circles: experiment.

for comparisons. It is probably also less effected by outer disturbances in the experimental environment. If we express the streamwise velocity signal of the TS-wave at a fixed downstream position by $u(y,t) = \tilde{u}(y)\sin(\omega t + \phi(y))$ that defines the phase $\phi(y)$, which is plotted in figure 2. There is a perfect agreement between PSE and DNS also in the phase and minor differences to the experimental results. Klingmann *et al.* (1993) found differences between their phase profiles and those of linear parallel theory. Those were, however, artificial and caused by a sign difference in the definition of $\phi(y)$ (1997). We have not included results of the linear parallel theory in figure 2 as they are very close to the DNS and PSE results, which can be seen in Fasel & Konzelmann (1990).

To produce neutral stability curves, DNS were performed for frequencies in the range $140 < F < 300$ with an interval of 10. Additional simulations were made close to tip of the unstable regions displayed in figure 3. The dashed grey curves in the figure represent the DNS results and cubic splines has been used to obtain plot data between the calculated points. The curve enclosing a larger region represents the neutral curve for v, whereas the neutral curve for u encloses a smaller unstable region. In the DNS calculations, the Reynolds number resolution was 1.2 and a cubic spline interpolation was used to find the neutral points. The two solid lines in figure 3 represents the neutral curves of u and v found by the PSE method. The low cost of PSE calculations allowed

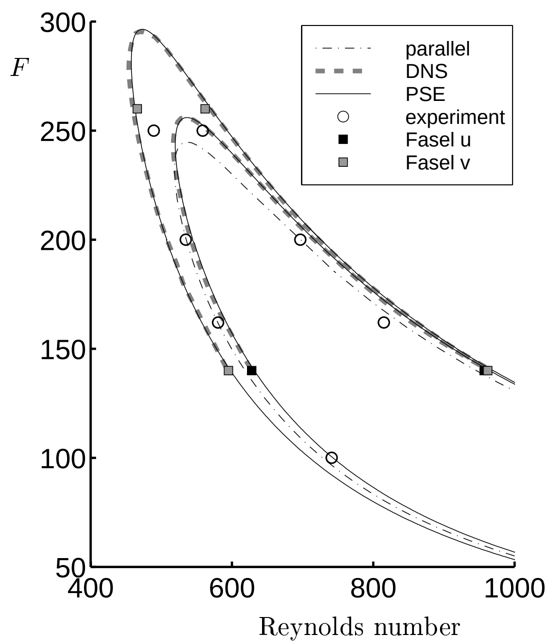

FIGURE 3. Neutral stability curves for non-parallel boundary layer, grey dashed curve: DNS, solid: PSE. The outer curves represent maximum of v and the inner maximum of u. DNS results by Fasel & Konzelmann (1990) are represented by squares, grey: maximum of u and black maximum of u. Experimental data are represented by circles.

calculations to a frequency as low as $F = 30$ and also high resolution in F. The resolution in F was 1 in the region $200 < F < 300$ and 5 below $F = 200$. Here, the step size in the streamwise direction was $\Delta R = 4.3$ and a cubic interpolation was used to find the neutral points. The agreement between PSE and DNS is excellent but a small difference can be found at branch I for v at the highest frequencies. Based on the results obtained using both methods, we determined the critical Reynolds number to 456 for v and 518 for u, with a uncertainty of respectively, ± 2 and ± 1.

Figure 3 also contains neutral stability points that we have read from the figures presented by Fasel & Konzelmann1990 and the agreement between those results and our calculations is good. The circles represent experimental data obtained by Klingmann *et al.* 1993 and for lower frequencies they actually agree better with parallel theory than with the non-parallel results. The experimental flow is more unstable at higher frequencies than the calculations predict, but is considerably closer to the calculations than previous experimental results. The accuracy of the experimental points is not estimated by Klingmann *et al.* 1993, but it must be a difficult task to find the points of zero derivative on a very flat experimental curve with some scatter and we question if better agreement can be anticipated with present measurement techniques.

To produce neutral stability curves for non-parallel boundary layer flow with highest possible accuracy, we have put great effort into reducing disturbances caused by wave generation and numerical issues in our DNS calculations. The results agree well with experiments, previous DNS calculations and present PSE calculations. From the neutral stability curves calculated by both DNS and PSE we have found the critical Reynolds numbers for growth of the streamwise u and wall normal v velocity components to be 518 and 456, respectively.

We are grateful to Mr. P. Andersson for his aid with the PSE calculations and Dr. J. Westin for making the experimental data available to us. This work has been supported by TFR (Swedish Research Council for Engineering Sciences).

References

Bertolotti, F. P., Herbert, T. & Spalart, P. R. 1992. Linear and nonlinear stability of the Blasius boundary layer. *J. Fluid Mech.* **242**, 441–474.

Fasel, H. & Konzelmann, U. 1990. Non-parallel stability of a flat-plate boundary layer using the complete navier-stokes equations. *J. Fluid Mech.* **221**, 311–347.

Gaster, M. 1974. On the effects of boundary-layer growth on flow stability. *J. Fluid Mech.* **66**, 465–480.

Hanifi, A., Henningson, D. S., Hein, S., Bertolotti, F. & Simen, M., 1994. Linear nonlocal instability analysis – the linear NOLOT code. FFA TN 1994-54, Technical Report from the Aeronautical Research Institute of Sweden (FFA), Bromma.

Kim, J., Moin, P. & Moser, R. 1987. Turbulence statistics in fully developed channel flow. *J. Fluid Mech.* **177**, 133–166.

Klingmann, B. G. B., Boiko, A., Westin, K., Kozlov, V. & Alfredsson, P. 1993. Experiments on the stability of Tollmien-Schlichting waves. *Eur. J. Mech., B/Fluids.* **12**, 493–514.

Lundbladh, A., Henningson, D. S. & Johansson, A. V., 1992. An efficient spectral integration method for the solution of the Navier-Stokes equations. FFA-TN 1992-28, Aeronautical Research Institute of Sweden, Bromma.

LUNDBLADH, A., SCHMID, P. J., BERLIN, S. & HENNINGSON, D. S., 1994. Simulation of bypass transition in spatially evolving flows. Proceedings of the AGARD Symposium on Application of Direct and Large Eddy Simulation to Transition and Turbulence, AGARD-CP-551.

WESTIN, K. J., . 1997. *Laminar-trubulent boundary layer transition influenced by free stream turbulence*. PhD thesis, Royal Institute of Technology, Stockholm, Sweden.

P2

Paper 2

SPATIAL SIMULATIONS OF OBLIQUE TRANSITION IN A BOUNDARY LAYER

S. Berlin
Dept. of Mech., KTH, S-10044 Stockholm, Sweden

A. Lundbladh
FFA, Box 11021, S-16111 Bromma, Sweden

D. S. Henningson
FFA, Box 11021, S-16111 Bromma, Sweden

Abstract. Simulations of oblique transition in the spatial domain are presented, covering the complete transition process into the turbulent regime. It is conjectured that the three stages identified here and elsewhere are universal for oblique transition in all shear flows: first a non-linear generation of a streamwise vortex by the oblique waves, second a transient growth of streaks from the vortex by the lift-up effect, and third a breakdown of the streaks due to secondary instability.

We will present an investigation of *bypass* transition, i.e. transition emanating from linear growth mechanisms other than exponential instabilities. This definition is in line with the original idea of Morkovin (1969), but is formulated in view of results on nonmodal transient growth (Hultgren &Gustavsson 1981, Gustavsson 1991 Butler & Farrell 1992, Reddy &Henningson 1993 Trefethen *et al.* 1993). In these investigations it was shown that significant growth of the disturbance energy is possible for certain two- (2-D) and three-dimensional (3-D) disturbances in shear flows at subcritical Reynolds numbers, where the largest growth was obtained for the 3-D perturbations. Physically, the growth is due to the Orr (1907) and *lift-up* mechanisms (Landahl 1975). Mathematically it can be explained by the fact that the linearized Navier-Stokes operator has non-orthogonal eigenfunctions, a necessary condition for subcritical transition to occur (Henningson & Reddy 1994).

In the investigation of Henningson, Lundbladh & Johansson (1993) the lift-up mechanism was found to play an important role in the growth of both infinitesimal and finite amplitude disturbances. In the study by Schmid & Henningson (1992) temporal simulations starting from a pair of oblique finite amplitude waves were performed. It was found that non-linearity rapidly excited components with zero streamwise wavenumber, i.e. streamwise vortices. By the lift-up effect the vortices generated large amplitude low and high-speed streaks. The breakdown to turbulence, which has recently been found to result from a secondary instability of the streaks (Kreiss, Lundbladh & Henningson 1994, Lundbladh, Henningson &Reddy 1994), occurs more rapidly than traditional transition initiated by the growth of 2-D waves.

Oblique transition has also been found in compressible flows. Fasel & Thumm (1991) and Chang & Malik (1994) found a similar scenario for a compressible boundary layer on a flat plate. In the latter investigation the "streamwise vortex mode" also played an important role and the initial amplitude necessary to trigger transition was found to be lower than for comparable secondary instability scenarios. The oblique transition scenario has also been found for flow in a compressible confined shear layer (Gathmann, Si-Ameur & Mathey 1993). In their study the oblique waves appeared naturally from noise introduced at the inflow boundary.

In the present study the oblique transition scenario has been simulated spatially for a zero-pressure gradient incompressible boundary layer. Joslin, Streett & Chang (1993), in a study aimed at validating the PSE approach, considered a similar case but ended their calculations before transition occurred. We will use a numerical simulation program solving the full three-dimensional incompressible Navier-Stokes equations developed by Lundbladh, Henningson & Johansson (1992). The program uses Fourier-Chebyshev spectral methods, similar to those of Kim, Moin & Moser (1987). The simulation program has recently been modified to handle spatial development of disturbances in channel and boundary layer flows. In a fringe region a forcing term was added to the Navier-Stokes equations. It was implemented such that the disturbances flowing out of the box were eliminated and the flow returned to its laminar state. In the fringe region wave disturbances can also be generated, simulating a vibrating ribbon 1993. This technique, which allows the streamwise expansion in Fourier modes to be retained while prescribing inflow and outflow conditions, is similar to that of Bertolotti, Herbert & Spalart (1992).

The inflow conditions for the present simulation consists of the Blasius mean flow plus a pair of oblique waves, each with an amplitude A (based on the maximum RMS of the streamwise velocity) of 0.01. They are taken as the least damped Orr-Sommerfeld mode for $\omega_0 = 0.08$ ($F_0 = \omega_0/R = 200 \times 10^{-6}$) and $\beta_0 = 0.192$, excluding the associated normal vorticity. Here ω_0 and $\pm\beta_0$ are the angular frequency and spanwise wavenumbers of the generated waves. The Reynolds number at the inflow ($R = U_\infty \delta_0^*/\nu$) is 400, based on the inflow displacement thickness (δ_0^*) and free-stream velocity (U_∞), which in the following are used to non-dimensionalize all quantities. The inflow position will in the following be denoted x_0.

Two calculations of the same scenario were performed. The first used $480 \times 97 \times 80$ modes in the streamwise, normal and spanwise directions, respectively, and the second used $720 \times 121 \times 120$ modes. (Note that spanwise symmetry was assumed and that dealiasing, using the 3/2 rule, was also applied in the horizontal directions.) As a test of the convergence, four maxima in the streamwise shear in the outer part of the boundary layer were compared [$x - x_0 \approx 200, 250, 300, 350, y \approx 5$ in Figure 2(b)]. The differences in the values were below 1% in the four maxima, although the position of the last maximum has changed slightly. The higher resolution corresponds to a grid step of 14 wall units in the streamwise direction, 6 for the spanwise and 4 for the largest step in the wall normal direction, based on the wall friction in the turbulent region.

Figure 1 shows the development of the coefficient of friction ($c_f = 2\tau_w/\rho U_\infty^2$, τ_w is the time and spanwise averaged wall shear stress) for the simulation. It

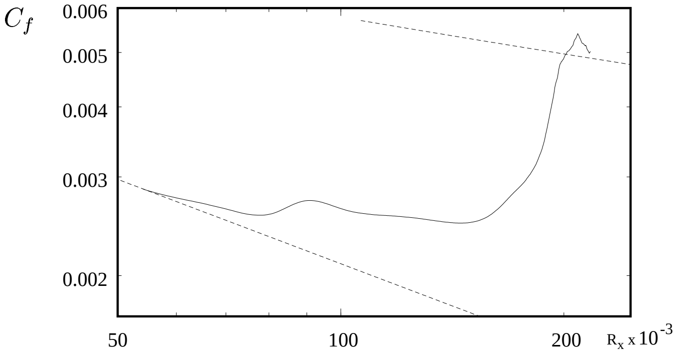

FIGURE 1. Coefficient of friction $c_f = 2\tau_w/\rho U_\infty^2$, τ_w is the averaged wall shear stress. $R_x = xU_\infty/\nu$ where x is the distance from the leading edge. Lower dashed line shows the value for a laminar Blasius boundary layer ($0.664R_x^{-1/2}$) and the upper curve is the turbulent friction $0.370(\log R_x)^{-2.584}$ by Shultz-Grunow (see Schlichting 1933 p. 643)

is evident that the simulation captures the complete transition process, all the way into the turbulent regime.

Figure 2 shows the breakdown to turbulence of the two oblique waves generated at the inflow boundary. In figure 2a, which shows the streamwise velocity in a wall-parallel plane, the appearance of streamwise streaks is observed at about $x - x_0 = 50$. The streaks subsequently grow to a large amplitude and become

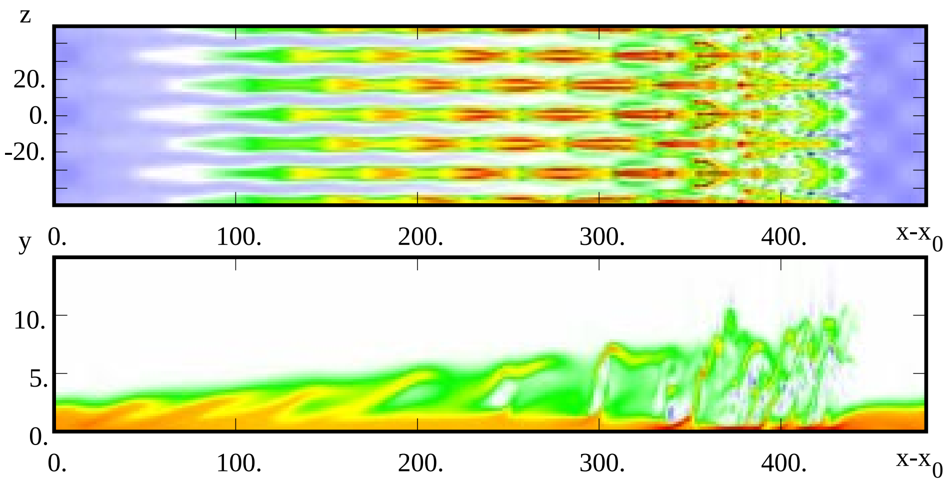

FIGURE 2. Instantaneous velocity fields. (a) Streamwise velocity at $y = 2.93$. Values range from red at 0.34 to blue at 1.08. (b) Streamwise shear at $z = 0$. Values range from blue at -0.18 to red at 1.9. Note the fringe region starts at $x - x_0 = 408$, at the right part of the computational box.

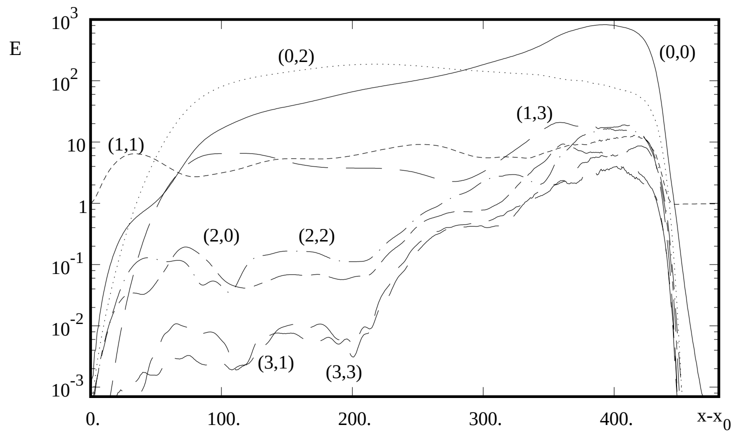

FIGURE 3. Energy in Fourier components with frequency and spanwise wavenumber $(\omega/\omega_0, \beta/\beta_0)$ as shown. The curves are normalized such that the energy of the (1,1) mode at inflow is set to unity.

unstable to a non-stationary disturbances, resulting in a breakdown to turbulence at about $x - x_0 = 350$. Figure 2b shows the streamwise shear in a side view of the boundary layer. Shear layers are seen to intensify and become unstable prior to the breakdown.

Figure 3 shows the energy in some of the excited Fourier components during the transition process. At the inflow only the $(1, \pm 1)$ components are excited. They show a rapid initial growth similar to that in the simulations by Schmid & Henningson (1992), who also set the initial normal vorticity to zero. The $(0, 0)$ $(0, \pm 2)$ $(2, 0)$ $(2, \pm 2)$ components subsequently increase due to nonlinear effects, since they are directly generated by the $(1, \pm 1)$ modes through the quadratic nonlinearity. The $(0, \pm 2)$ components grow more rapidly than the other modes and continues to grow to grow until about $x - x_0 = 100$. The latter part of this growth was found by Schmid & Henningson to be due to a linear forcing of the streak (u component) from the vortex (v, w components) for the same wavenumber. A second phase of rapid growth starts for modes with nonzero ω, eventually completing the transition process. This growth can best be described as a secondary instability on the base flow with a spanwise variation given by the $(0, \pm 2)$ streaks. A similar rapid growth of oblique modes from a state of streamwise streaks was found for transition in plane Couette flow by Kreiss, Lundbladh & Henningson (1994).

In order to put the present simulation in perspective, data from a number of recent spatial simulations have been compiled in table 1. The transition process in the present simulation occupies about the same streamwise domain as in the simulations of secondary instability induced breakdown by Kloker & Fasel (1993), in spite of the exponential growth of the 2-D mode and higher input amplitude in the latter case. This is accentuated by the results of Spalart & Yang (1987) who simulated an even larger domain by following a streamwise periodic box,

Ref.	R	R_{x_0}	R_{x_E}	A_{2D}	A_{3D}	ω_0	β_0	Trans.
Present	400	54000	220000	—	0.01	0.080	0.192	yes
JSC	733	182000	447000	0.0048	0.0000145	0.091	0.242	no
JSC	900	238000	489000	—	0.01	0.0774	0.2	no
KF	679	155000	304000	0.03	0.002	0.075	0.29	yes
SY	1260	532000	1390000	0.01	noise	0.095	—	no

TABLE 1. Comparison of recent spatial simulations of instability and transition. JSC refers to Joslin, Streett & Chang (1993), KF to Kloker & Fasel (1993) and SY to Spalart & Yang (1987). The last column indicates whether the simulation included the complete transition region. x_0 is the position of the disturbance generator and x_E is the end of the simulated region.

accounting for the streamwise growth of the boundary layer and disturbance in an approximate manner. In spite of covering a larger Reynolds number range their simulations did not reach the turbulent state.

In the present investigation the wave amplitude at the inflow is low, resulting in a long growth region before breakdown. This initial amplitude represents the lowest amplitude disturbance of the chosen form, giving transition in this computational box. In a simulation with $A = 0.0086$ the secondary instability was not strong enough, and thus no transition occurred. For the same initial amplitude Joslin, Streett & Chang (1993)) did not find that the growth was sufficiently rapid to cause transition within their computational box, although the domain was longer and the inflow at a higher Reynolds number than the present study. The reason may be their use of complete eigenmodes as inflow condition (i.e. including the normal vorticity part of the eigenmode), which implies that they do not have the rapid transient growth of the oblique $(1, \pm 1)$ modes seen in the present case.

The oblique transition scenario in the boundary layer is quite similar to that seen in channel flow (Schmid & Henningson 1992). In addition the streaks seem to break down due to the same a secondary instability mechanism (Kreiss, Lundbladh &Henningson 1994, Lundbladh, Henningson & Reddy 1994). In light of these findings, and those of other investigations discussed here, we conjecture that the following three stages occurs during oblique transition in shear flows:

- Initial non-linear generation of a streamwise vortex by the two oblique waves.
- Generation of streaks from the interaction of the streamwise vortex with the mean shear by the lift-up effect.
- Breakdown of the flow due to a secondary instability of the streaks, when these exceed a threshold amplitude.

Note that if the amplitude of the inflow disturbance is large enough the breakdown may be so rapid that the second and the third stage overlap.

Acknowledgments

The computer time for the present simulations were provided by the National Center for Supercomputing Applications, Urbana, IL and the Pittsburgh Supercomputer Center, Pittsburgh, Pennsylvania. The research was funded by The Swedish Research Council for the Engineering Sciences (TFR) and the Swedish National Board for Industrial and Technical Development (NUTEK).

References

Bertolotti, F. P., Herbert, T. & Spalart, P. R. 1992. Linear and nonlinear stability of the Blasius boundary layer. *J. Fluid Mech.* **242**, 441–474.

Butler, K. M. & Farrell, B. F. 1992. Three-dimensional optimal perturbations in viscous shear flow. *Phys. Fluids A.* **4**, 1637–1650.

Chang, C.-L. & Malik, M. R. 1994. Oblique-mode breakdown and secondary instability in supersonic boundary layers. *J. Fluid Mech.* **273**, 323–360.

Fasel, H. & Thumm, A. 1991. Direct numerical simulation of three-dimensional breakdown in supersonic boundary layer transition. *Bull. Am. Phys. Soc.* **36**, 2701.

Gathmann, R. J., Si-Ameur, M. & Mathey, F. 1993. Numerical simulations of three-dimensional natural transition in the compressible confined shear layer. *Phys. Fluids A.* **5**, 2946–2968.

Gustavsson, L. H. 1991. Energy growth of three-dimensional disturbances in plane Poiseuille flow. *J. Fluid Mech.* **224**, 241–260.

Henningson, D. S., Lundbladh, A. & Johansson, A. V. 1993. A mechanism for bypass transition from localized disturbances in wall bounded shear flows. *J. Fluid Mech.* **250**, 169–207.

Henningson, D. S. & Reddy, S. C. 1994. On the role of linear mechanisms in transition to turbulence. *Phys. Fluids.* **6**, 1396–1398.

Hultgren, L. S. & Gustavsson, L. H. 1981. Algebraic growth of disturbances in a laminar boundary layer. *Phys. Fluids.* **24**, 1000–1004.

Joslin, R. D., Streett, C. L. & Chang, C. L. 1993. Spatial direct numerical simulations of boundary-layer transition mechanisms: Validation of PSE theory. *Theoret. Comput. Fluid Dyn.* **4**, 271–288.

Kim, J., Moin, P. & Moser, R. 1987. Turbulence statistics in fully developed channel flow. *J. Fluid Mech.* **177**, 133–166.

Kloker, M. & Fasel, H., 1993. Numerical simulation of transition in a boundary layer with strong adverse pressure gradient. Ninth Symposium on Turbulent Shear Flows, Kyoto, Japan.

Kreiss, G., Lundbladh, A. & Henningson, D. S. 1994. Bounds for threshold amplitudes in subcritical shear flows. *J. Fluid Mech.* **270**, 175–198.

Landahl, M. T. 1975. Wave breakdown and turbulence. *SIAM J. Appl. Math.* **28**, 735–756.

Lundbladh, A. & Henningson, D. S., 1993. Numerical simulation of spatial disturbance development in rotating channel flow. FFA-TN 1993-30, Aeronautical Research Institute of Sweden, Bromma.

Lundbladh, A., Henningson, D. S. & Johansson, A. V., 1992. An efficient spectral integration method for the solution of the Navier-Stokes equations. FFA-TN 1992-28, Aeronautical Research Institute of Sweden, Bromma.

Lundbladh, A., Henningson, D. S. & Reddy, S. C. 1994. Threshold amplitudes for transition in channel flows. In *Transition, Turbulence and Combustion, Volume I* (Hussaini, M. Y., Gatski, T. B. & Jackson, T. L., editors), pp. 309–318. Kluwer, Dordrecht.

Morkovin, M. V. 1969. The many faces of transition. In *Viscous Drag Reduction* (Wells, C. S., editor). Plenum Press.

Orr, W. M. F. 1907. The stability or instability of the steady motions of a perfect liquid and of a viscous liquid. Part I: A perfect liquid. Part II: A viscous liquid. *Proc. R. Irish Acad. A.* **27**, 9–138.

Reddy, S. C. & Henningson, D. S. 1993. Energy growth in viscous channel flows. *J. Fluid Mech.* **252**, 209–238.

Schlichting, H., 1933. Zur Entstehung der Turbulenz bei der Plattenströmung. Nachr. Ges. Wiss. Göttingen, 181–208.

Schmid, P. J. & Henningson, D. S. 1992. A new mechanism for rapid transition involving a pair of oblique waves. *Phys. Fluids A.* **4**, 1986–1989.

Spalart, P. R. & Yang, K. 1987. Numerical study of ribbon induced transition in blasius flow. *J. Fluid Mech.* **178**, 345–365.

Trefethen, L. N., Trefethen, A. E., Reddy, S. C. & Driscoll, T. A. 1993. Hydrodynamic stability without eigenvalues. *Science.* **261**, 578–584.

Paper 3

P3

NUMERICAL AND EXPERIMENTAL INVESTIGATIONS OF OBLIQUE BOUNDARY LAYER TRANSITION

S. Berlin
Dept. of Mech., KTH, S-10044 Stockholm, Sweden

M. Wiegel
Institut für Strömungsmechanik Bunsenstraße 10, D-37073 Göttingen, Germany

D. S. Henningson
FFA, Box 11021, S-16111 Bromma, Sweden

Abstract. A transition scenario initiated by two oblique waves is studied in an incompressible boundary layer. Hot-wire measurements and flow visualizations of this scenario are reported for the first time. The experimental results are compared with spatial direct numerical simulations and a good qualitative agreement is found. Also quantitative agreement is found when the experimental device for disturbance generation is closely modeled and pressure gradient effects taken into account. The oblique waves are found to interact nonlinearly to produce streamwise streaks growing downstream, related to non-modal linear growth mechanisms. The same has previously been observed in channel flows and calculations of both compressible and incompressible boundary layers. The flow structures of oblique transition have many similarities to K- and H-type transition, for which two-dimensional Tollmien-Schlichting waves are the starting point. However, two-dimensional Tollmien-Schlichting waves are usually not initiated or observed in oblique transition and consequently the similarities are due to the oblique waves and streamwise streaks appearing in all three scenarios.

1. Introduction

1.1. Tollmien-Schlichting waves. Transition from laminar to turbulent flow in viscous boundary layers is of great practical interest and is far from understood. One possible route to transition that has been observed in low noise environments is the “Tollmien-Schlichting (TS) secondary instability scenario”. A majority of the research efforts on laminar-turbulent transition has been focused on this scenario. Its first stage, or primary instability, is the growth of two-dimensional TS-waves and can be predicted by solving the Orr-Sommerfeld equation for exponential instabilities. The two-dimensional state has been found to develop into one of two basic three-dimensional stages, then to turbulence. Herbert (1983*a*, 1983*b*) found that the two three-dimensional stages were caused by secondary instabilities of the two-dimensional state. These occurs if the amplitude of the two-dimensional TS-wave is above a given threshold. One of the three-dimensional stages was observed experimentally by Klebanoff, Tidstrom & Sargent (1962) and is called K-type or fundamental breakdown. The other was first observed by Kachanov, Kozlov & Levchenko (1977) and goes under the names H-type or subharmonic breakdown. Kachanov (1994) calls it N-type transition in his review over the physical mechanisms involved in transition. A review over the theoretical efforts concerning the secondary instabilities has been written by Herbert (1988). Kleiser & Zang (1991) has reviewed the numerical work in the area. Details of these scenarios are presented in section 4, where the results on oblique transition presented here are discussed in light of previous findings.

1.2. Transient Growth. Before the 1940's experimental investigators were unable to identify TS-waves and the following secondary instability in both boundary layers and channel flows. Transition was instead caused by other disturbances and other growth mechanisms. These are obviously as likely now as they were then. Morkovin (1969) stated "We can bypass the TS-mechanism altogether", and transition caused by growth mechanisms other than exponential instabilities are often named *bypass-transition*. The growth mechanisms behind bypass transition can be found by examining the linearized Navier-Stokes equations. Since the nonlinear terms are conservative in the Naiver-Stokes equations they cannot by themselves be responsible for production of disturbance energy. In fact, considering the evolution equation for the total disturbance energy, the so called Reynolds-Orr equation, all of the nonlinear terms drop out, implying that the instantaneous growth rate is independent of the disturbance energy (see e.g. Joseph 1976, Henningson 1996).

The existence of growth mechanisms other than those associated with exponential growth were known already to Orr (1907) and Kelvin (1887), but the investigations by Gustavsson (1991), Butler & Farell (1992), Reddy & Henningson (1993), Trefethen *et al.* (1993) showing the possible magnitude of the transient growth, clearly indicated their potential for causing transition.

In order to briefly discuss the concept of transient growth and relate it to the mathematical characteristics of the governing equations we will consider the horizontally Fourier transformed linear disturbance equations. We have

$$\frac{d\hat{\mathbf{u}}}{dt} = \mathcal{L}\hat{\mathbf{u}}(t), \qquad \hat{\mathbf{u}}(0) = \hat{\mathbf{u}}_0 \tag{1}$$

where $\mathcal{L}$ is the linearized Navier-Stokes operator around a parallel mean flow. The solution can be written $\hat{\mathbf{u}}(t) = \exp(t\mathcal{L})\hat{\mathbf{u}}_0$ and the maximum growth experienced at time t as

$$\max_{\hat{\mathbf{u}}_0} \frac{\|\hat{\mathbf{u}}(t)\|}{\|\hat{\mathbf{u}}_0\|} = \| \exp(t\mathcal{L}) \| \tag{2}$$

The norm is here taken as the disturbance energy integrated over the wall-normal direction

$$\| \hat{\mathbf{u}}(t) \| = \left(\int |\hat{\mathbf{u}}(y,t)|^2 dy \right)^{1/2}. \tag{3}$$

It is possible to obtain a bound on the maximum growth of the following form

$$\exp(Re\{\lambda_{max}\}) \leq \| \exp(t\mathcal{L}) \| \leq \kappa \exp(Re\{\lambda_{max}\}) \tag{4}$$

The constant κ can be thought of as the condition number of the "matrix of eigenvalues", which can be generalized to infinite dimensional operators (Trefethen 1997). If $\mathcal{L}$ were a normal operator or equivalently if all of its eigenfunctions were orthogonal, this condition number would be unity, i.e. $\kappa = 1$. For streamwise independent disturbances or streaks, which experience the largest transient growth, it can be shown that $\kappa = \mathcal{O}(R)$, where R is the Reynolds number based on a suitable boundary layer thickness. The physical mechanism behind this growth is the *lift-up* effect (Landahl 1975). Weak streamwise counter rotating vortices in the shear layer can lift up fluid with low streamwise velocity from the wall and bring high speed fluid down towards the wall. This will create streaks of large amplitude in the streamwise velocity component. In the inviscid case the corresponding perturbation amplitude grows linearly with time, something recognized by Ellingsen & Palm (1975).

Another consequence of a non-normal operator is that the corresponding linear system may show a large response to forcing, although the forcing is not at a resonance condition. Let us consider the linear problem above, driven by a real frequency ω

$$\frac{d\hat{\mathbf{u}}}{dt} = \mathcal{L}\hat{\mathbf{u}}(t) + e^{i\omega t}\hat{\mathbf{v}}(x,y,z), \tag{5}$$

the time asymptotic response is given by

$$\hat{u}(t) = e^{i\omega t}(i\omega I - \mathcal{L})^{-1}\hat{\mathbf{v}} \tag{6}$$

The response is given by the resolvent $(i\omega I - \mathcal{L})^{-1}$, which can be given the following bound,

$$\frac{1}{|\lambda - i\omega|} \leq \|(i\omega I - \mathcal{L})^{-1}\| \leq \frac{\kappa}{|\lambda - i\omega|}, \tag{7}$$

where $|\lambda - i\omega|$ represents the closest distance between $i\omega$ and the spectrum of $\mathcal{L}$. For streamwise independent disturbances the distance between ω and the closest eigenvalue to $\mathcal{L}$ is $\mathcal{O}(1/R)$, which together with the size of the condition number κ implies that the response is bounded by $\mathcal{O}(R^2)$. A summary of results on optimal transient growth and optimal forcing, from several shear flows, is found in table 1. In most of the theoretical work on transient growth and the sensitivity to forcing (non-modal growth), a temporal formulation has been used. The disturbances are then thought to grow in time, which simplifies analysis and calculations. In a physical experiment or a spatial simulation, however, disturbances grow in space. Recently transient growth in boundary layers, or maybe better non-modal growth, has been considered in spatial formulations by Luchini (1996, 1997) and Andersson, Berggren & Henningson (1997). They found that the maximum possible energy growth scales linearly with the distance from the leading edge.

The possibilities of strong growth discussed above explains that transition do occur even when no exponential instabilities exist. In cases where exponential instabilities are present, there will be a competition or combination between the different mechanisms depending on the disturbances present. And obviously the nonlinear coupling between different disturbances will play an important role. The non-modal growth of streamwise streaks is just the first step of transition. The possibility of a subsequent secondary instability of streaks and growth of three-dimensional disturbances has been investigated by Reddy *et al.* (1997) for channel flows. They found that streak breakdown is caused by an inflectional

Flow	Quantity	Value	α	β
Couette	max resonance $\sup_{\omega\in\mathcal{R}} \|\|(\omega I-\mathcal{L})^{-1}\|\|$	$(R/8.12)^2$	0	1.18
	max growth $\sup_{t<0} \|\|exp(-it\mathcal{L})\|\|$	$R/29.1$	$35.7/R$	1.60
Poiseuille	max resonance $\sup_{\omega\in\mathcal{R}} \|\|(\omega I-\mathcal{L})^{-1}\|\|$	$(R/17.4)^2$	0	1.62
	max growth $\sup_{t<0} \|\|exp(-it\mathcal{L})\|\|$	$R/71.5$	0	2.04
Blasius	max resonance $\sup_{\omega\in\mathcal{R}} \|\|(\omega I-\mathcal{L})^{-1}\|\|$	$(R/1.83)^2$	0	0.21
	max growth $\sup_{t<0} \|\|exp(-it\mathcal{L})\|\|$	$R/25.7$	0	0.65

TABLE 1. Maximum resonance and transient growth for selected shear flows and the corresponding streamwise α and spanwise β wavenumber. For Couette and Poiseuille flow the half channel width and the centerline velocity are used to make the quantities non-dimensional and for Blasius the displacement thickness and the free-stream velocity have that role. The values are taken from Trefethen *et al.* (1993), Butler & Farrell (1992) and Schmid (private communication).

secondary instability, normally in the spanwise direction but for some cases in the wall-normal direction.

1.3. Oblique Transition. Oblique transition is a transition scenario initiated by two oblique waves with opposite wave angle. We call these the $(1, \pm 1)$ modes, where the first 1 stands for the generated fundamental frequency in the spatial cases and for the fundamental streamwise wavenumber in the temporal cases. The second 1 stands for the fundamental spanwise wavenumber. Lu & Henningson (1990) first noted the potential of oblique disturbances in incompressible flows in their study of localized disturbances in Poiseuille flow. Schmid & Henningson (1992) calculated oblique transition in channel flow using a temporal direct numerical simulation (DNS) code. They showed, for plane Poiseuille flow, that initial forcing and subsequent transient growth caused the rapid growth of the $(0, 2)$ mode. They calculated the relation between the energy transfered to the $(0, 2)$ mode by the nonlinear terms and the energy growth by transient linear mechanisms and found the latter to be the significant part. Joslin, Streett and Chang (1992,1993) calculated oblique transition in an incompressible boundary layer using both parabolized stability equations (PSE) and spatial DNS. They chose two different amplitudes of the oblique waves. In the low amplitude case the $(0, 2)$ mode grew rapidly and then decayed whereas they noted both the rapid growth of the $(0, 2)$ mode and a subsequent growth of other modes in the high amplitude case. Berlin, Lundbladh & Henningson (1994) chose the parameters of the oblique waves to avoid any exponential instability in their spatial DNS calculation. They pointed out that the rapid transient growth of the $(0, 2)$ mode was associated with high- and low speed streaks in the streamwise velocity component and conjectured that the onset of the growth of time-dependent modes was caused by secondary instability of the streaks when these reached a threshold value. For channel flow Reddy *et al.* (1997) found that the energy needed to initiate oblique transition is substantially lower than that needed in the transition scenarios caused by the two-dimensional TS-wave. Similar results have also been found in boundary layer flow by Schmid, Reddy & Henningson (1996).

Oblique transition has also been studied in compressible flows, where Fasel & Thumm (1991) noted that it is a"powerful process". Using nonlinear PSE Chang & Malik (1992, 1994) studied this scenario in a supersonic boundary layer and found oblique-wave breakdown to be a more viable route to transition and that it could be initiated by lower amplitude disturbance, compared to traditional secondary instability. Using DNS Fasel, Thumm & Bestek (1993) and Sandham, Adams & Kleiser (1994) studied oblique transition in compressible boundary layers and all investigators observed, first the nonlinear interaction of the oblique waves generating the streamwise vortex mode $(0, 2)$ and then its rapid growth. The fact that the rapid growth of the $(0, 2)$ mode was caused by transient growth and the non-normality of the linear operator discussed above was shown by Hanifi, Schmid & Henningson (1996).

Experimentally oblique transition has been investigated in Poiseuille flow by Elofsson (1995) and by Wiegel (1997) and Elofsson (1997) in zero-pressure gradient boundary layers. In the present investigation of oblique transition further details has been studied using both experiments and numerical simulations. A similar comparison between experiment and simulation has been done for plane Poiseuille flow by Elofsson & Lundbladh (1994).

The tools used in the physical and numerical experiments are covered in §2. §2.1 contains a description of the experimental set-up and the measurement techniques adopted for the present experiment and §2.2 the numerical method. Results from experiments and simulations are compared in §3 to explain the different stages of oblique transition. In §4 the oblique transition is compared to K- and H-type transition and the reason for the similarities of the structures observed at the late transition state are discussed. Concluding remarks are given in §5.

2. Investigational Tools

2.1. Experimental method.

2.1.1. *Experimental set-up and measurement technique.* The experimental investigation was performed in the low turbulence wind tunnel (TUG) at DLR Göttingen. It is an open windtunnel with the fan at the inlet. A honeycomb and turbulence damping screens damp the turbulence level together with a plane 16:1 contraction to 0.065 % for the used windspeed of $U_\infty = 12$ m/s.

The measurements were performed on a flat Plexiglas plate 1500 mm wide, 1175 mm long and 40 mm thick, which was mounted vertically in the test section. The plate had an elliptic leading edge and a flap at the trailing edge. The device used to generate controlled three-dimensional disturbances is displayed in figure 1. It was situated 206 mm downstream of the leading edge and consisted of 40 slots, 10 mm wide and 0.3 mm in the streamwise direction, placed beneath each other with a spacing of 0.5 mm in the spanwise direction. Each slot led to a pressure chamber inside the plate, in which pressure fluctuations from a loudspeaker were introduced through a plastic tube. We make use of the effect

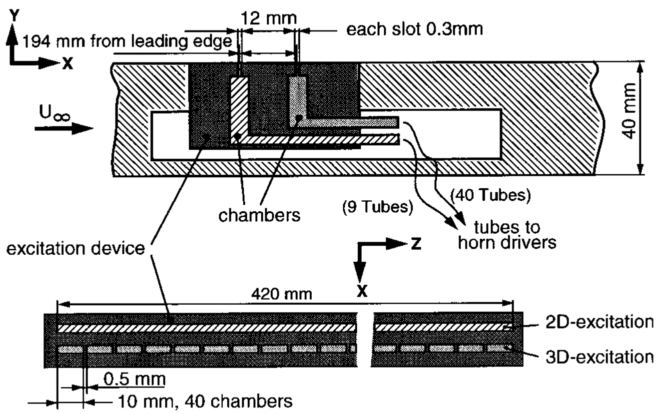

FIGURE 1. Device fore disturbance generation. Note that the distance to the virtual leading edge is 20 mm less than the distance to the actual leading edge given in the figure.

that small periodic pressure oscillations produced by the loudspeakers cause small periodic velocity fluctuations which can be used for a well defined excitation of the boundary layer. A signal generator with 20 channels followed by amplifiers supplied the excitation signals for the loudspeakers. It was possible to address each loudspeaker separately, nevertheless all channels were phase-locked. By prescribing the phase shift between the channels one or two oblique waves could be generated. More details of the set-up and the excitation device can be found in Wiegel (1997).

Detailed measurements were then made by both hot-wire anemometry and particle image velocimetry (PIV). Flow visualizations gave a good overview of the transition scenario and were useful to choose suitable spanwise wavelength, frequency and amplitude for the oblique waves. For PIV measurements and flow visualizations a laser system created a light sheet, which was aligned parallel to the surface of the plate and could be manually scanned through the boundary layer. The light sheet was 0.6 mm thick and illuminated tracer particles in the observation area stroboscopicly with a repetition-rate of 10 Hz. Each illumination actually consisted of two lightpulses with a duration of 20 ns. The time-delay between the two pulses could be varied in a wide range but for our set-up it was chosen to 100 μs. The mean diameter of the tracer particles in the flow was approximately 1 μm and the seeding-rake was located upstream of the turbulence damping screens. The pictures could be recorded with a CCD camera or with a standard 35 mm camera. The recorded area was of the order of 0.2 m by 0.1 m. The signal of the CCD camera was digitized by means of a frame grabber. The frame grabber, or the shutter release of the 35 mm camera, and the laser light-pulses as well were triggered by the signal generator for the excitation, so that a fixed phase relation between excitation and recorded picture was guaranteed. It was also possible to set an additional phase shift to acquire pictures at various phases over one period. The inaccuracy of the velocity readings produced by the utilized evaluation procedure is, averaged over the entire PIV recording, less than 1 % of the mean flow velocity.

A three-axis traversing system were used for single hot-wire sensors. The traversing mechanisms were driven by computer-controlled stepper motors with a wall-normal resolution of 0.001 mm and a spanwise resolution of 0.01 mm. Velocity, temperature, and dynamic pressure data were directly digitized through a 12-bit A/D converter. The fluctuating velocities at the desired frequency was filtered in a 1 Hz band pass by computing the autospectral density function using an FFT. The cross spectrum between the hot-wire signal and the forcing signal of the signal generator provided phase information.

2.1.2. *Flow quality and wave parameters.* The flap at the trailing edge of the plate was adjusted to achieve as close to zero pressure gradient boundary layer in the measurement region as possible. The measured pressure gradient is presented in figure 2 and the scatter of order 0.001 in the experimental data around the fit is probably due to low frequency velocity fluctuations. For comparison the predicted pressure gradient from a boundary layer calculation is presented. The boundary layer program (Rotta 1971) accounts for the shape of the leading edge but not the walls of the windtunnel and the flap. It takes the pressure distribution form a potential flow solution as indata. As the boundary layer develops under a pressure gradient around the leading edge the boundary layer thickness at a certain downstream coordinate will differ form that of a theoretical Blasius boundary layer. Therefore a virtual leading edge is calculated from the actual displacement thickness in the measurement region to fit a theoretical leading edge. This is situated 20 mm downstream of the real leading edge and we will from now on refer all downstream distances to the virtual leading edge both in the experimental and numerical results presented. All wall-normal coordinates y will either be normalized by the Blasius reference length $\delta_r = (\nu x/U_\infty)^{1/2}$ at the local x or given in millimeters. Figure 3 displays the velocity profiles

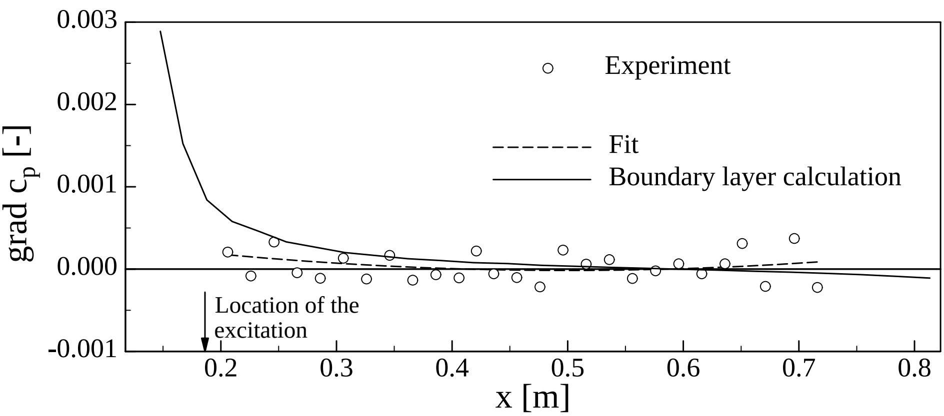

FIGURE 2. Pressure gradient in streamwise direction without excitation, z = 0

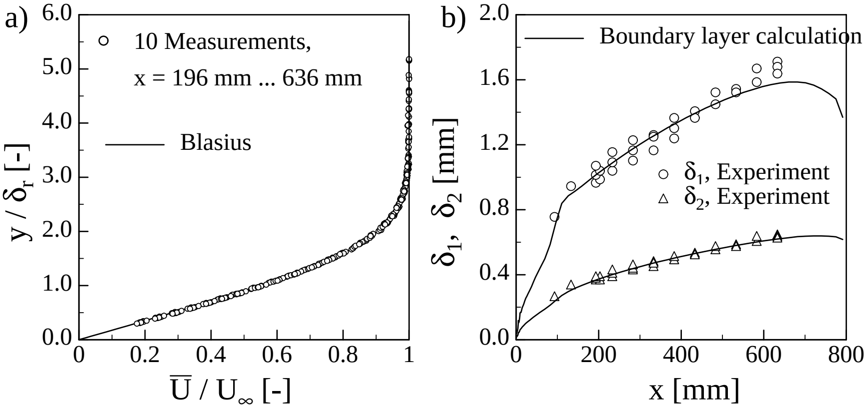

FIGURE 3. (*a*) Mean velocity profile, (*b*) Variation of the integral flow parameters , δ_1 and δ_2, without excitation

achieved in the measurement section as well as the downstream development of the displacement thickness. This figure also shows that we can assume a Blasius boundary layer downstream of the excitation. The spanwise spectra of the undisturbed meanflow of both free-stream and boundary layer were checked to make sure that there were no peaks at the spanwise wavelengths excited later in the experiment.

The excitation device introduces locally a wall-normal velocity but the goal is to have controlled oblique eigenmodes moving downstream. Therefore the calibration of the excitation is based on measuring the disturbance level inside the boundary layer downstream of the excitation. Setting the same phase of the excitation signal for all 40 slots a two-dimensional wave was generated, which made it possible to check that the amplitude was evenly distributed in the spanwise direction. The frequency of the generated oblique waves was 90 Hz corresponding to a non-dimensional frequency in the current setting of F=59 ($F = 2\pi f\nu/(U_\infty^2 \times 10^{-6})$) and setting the phase shift between adjacent slots to ± 60 degrees a spanwise wavelength of 63 mm was obtained. The modeshape of the generated waves were compared to that calculated by linear theory and good agreement was found as shown in figure 4, where also the mean velocity profiles are displayed.

Setting frequency and spanwise wavelength the waveangle was from flow visualizations found to be 35 ± 3 degrees well in accordance with the theoretical value of 38 degrees. The fact that the generation device was directly forcing the desired eigenmode was established by showing that the amplitude of the oblique waves was a linear response of the excitation amplitude A. This is shown in figure 5 (*b*), where A is linearly related to the loudspeaker input. A bandpass filter selected the frequency of the oblique waves for the u_{rms} displayed in the figure and as the measurements were done close (x=217 mm) to the disturbance generation device higher harmonics had very low amplitude. Figure 5 (*a*) demonstrates that the modeshape was independent of the forcing amplitude.

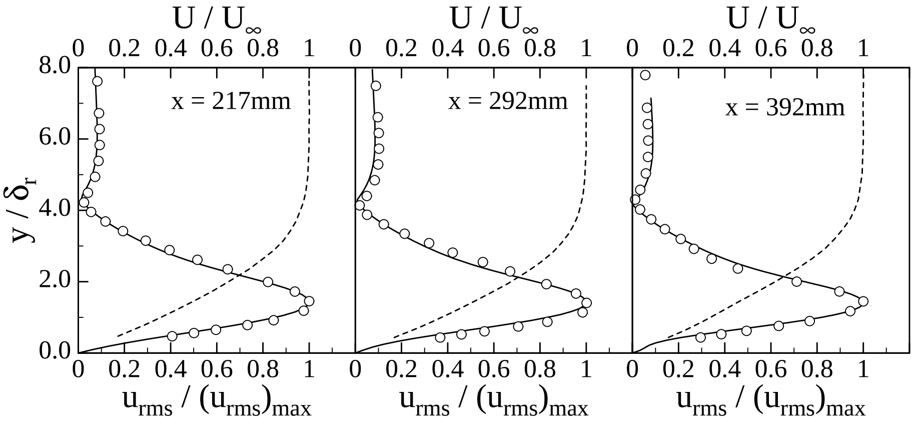

FIGURE 4. Modeshape at various downstream locations for f=90 Hz and U_∞=12 m/s, solid lines represents linear theory and dashed lines mean velocity.

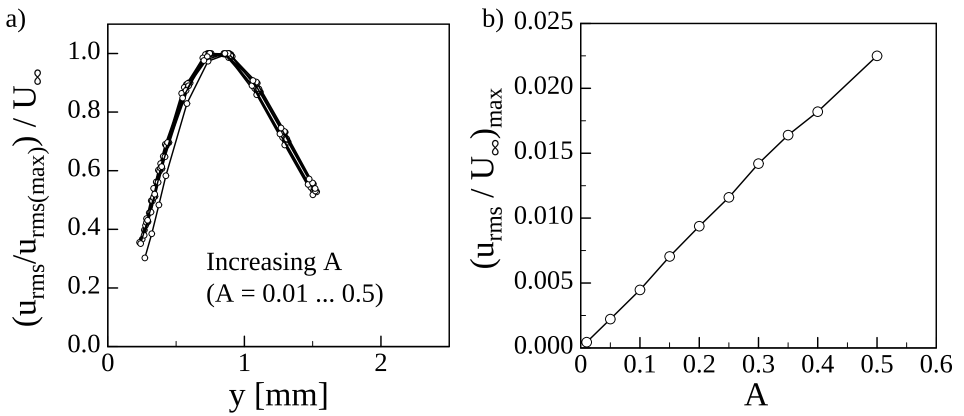

FIGURE 5. (a) Wall-normal variation of the normalized u_{rms} for various excitation levels, (b) Maximum of u_{rms} at x=217 mm and z= 0 amplitude versus excitation level.

2.2. Numerical method.

2.2.1. *Numerical scheme.* The simulation code (see Lundbladh, Henningson & Johansson 1992 and Lundbladh *et al.* 1994) used for the present computations uses spectral methods to solve the three-dimensional, time dependent, incompressible Navier-Stokes equations. The algorithm is similar to that of Kim, Moin & Moser (1987), i.e. Fourier representation in the streamwise (x) and spanwise (z) directions and Chebyshev polynomials in the wall-normal (y) direction and pseudo-spectral treatment of the nonlinear terms. The time advancement used was a four-step low storage third-order Runge-Kutta method for the nonlinear terms and a second-order Crank-Nicholson method for the linear terms. Aliasing errors from the evaluation of the nonlinear terms were removed by the $\frac{3}{2}$-rule when the horizontal FFTs were calculated.

To correctly account for the downstream boundary layer growth and pressure gradient effects a spatial technique is necessary. That requirement was combined with the periodic boundary condition in the streamwise direction by the implementation of a "fringe region", similar to that described by Bertolotti, Herbert & Spalart (1992). In this region, at the downstream end of the computational box, the function $\lambda(x)$ in equation (8) is smoothly raised from zero and the flow is forced to a desired solution $\mathbf{v}$ in the following manner,

$$\frac{\partial \mathbf{u}}{\partial t} = NS(\mathbf{u}) + \lambda(x)(\mathbf{v} - \mathbf{u}) + \mathbf{g} \tag{8}$$

$$\nabla \cdot \mathbf{u} = 0 \tag{9}$$

where $\mathbf{u}$ is the solution vector and $NS(\mathbf{u})$ the right hand side of the (unforced) momentum equations. Both $\mathbf{g}$, which is a disturbance forcing, and $\mathbf{v}$ may depend on the three spatial coordinates and time. $\mathbf{v}$ is smoothly changed from the laminar boundary layer profile at the beginning of the fringe region to the prescribed inflow velocity vector. This is normally a boundary layer profile of a chosen Falkner-Skan flow, but can also contain a disturbance. This method damps disturbances flowing out of the physical region and smoothly transforms the flow to the desired inflow state, with a minimal upstream influence.

In order to set the free-stream boundary condition closer to the wall, a generalization of the boundary condition used by Malik, Zang & Hussaini (1985) was implemented. Since it is applied in Fourier space with different coefficients for each wavenumber, it is nonlocal in physical space and takes the following from,

$$\frac{\partial \hat{\mathbf{u}}}{\partial y} + |k|\hat{\mathbf{u}} = \frac{\partial \hat{\mathbf{v}}}{\partial y} + |k|\hat{\mathbf{v}}. \tag{10}$$

Here k is the absolute value of the horizontal wavenumber vector and $\hat{\mathbf{u}}$ is the Fourier transforms of $\mathbf{u}$. The Fourier transform $\hat{\mathbf{v}}$ of $\mathbf{v}$ is usually the local solution to a Falkner-Skan flow, with the streamwise free-stream velocity varying as

$$U = U_0 x^m. \tag{11}$$

$\mathbf{v}$ can also be chosen arbitrarily in order to simulate other pressure variations than those found in Falkner-Skan flow. On the wall the boundary condition is either no slip or a time dependent wall-normal velocity.

2.2.2. *Disturbance generation and box dimensions.* The presented numerical implementation provides several possibilities for disturbances generation. Oblique waves with a frequency $\omega_0 = 90$ Hz and a spanwise wavenumber of $\beta_0 = 99.73$ m^{-1} has in this investigation been generated with five different methods. In the presentation of results we will transform the non-dimensional variables used in the simulation code to dimensional ones, using the kinematic viscosity for air and free-stream velocity $U_\infty = 12$ m/s. We will also refer the downstream coordinate

x to the virtual leading edge of the experiment. We have given the five different generation methods of oblique waves the following abbreviations:

FRIN : Generation in the fringe region by adding the least damped Orr-Sommerfeld mode for the chosen parameters to the forcing vector $\mathbf{v}$ in equation 8. The computational box was in this case designed such that the inflow was at $x = 186$ mm.

BODY : Generation by a body force. $\mathbf{g}$ was in the volume $184 \leq x \leq 187$ mm, $0 \leq y \leq 1.55$ mm assigned to: $g_x = A\,cos(\beta_0 z)cos(\omega_0 t)/(2\omega_0)$, $g_y = A\,cos(\beta_0 z)sin(\omega_0 t)$, $g_z = -A\,sin(\beta_0 z)sin(\omega_0 t)/(2\beta_0)$, where the amplitude A was smoothly reduced to be zero at the top boundary of the forcing volume.

BLOW : Generation by blowing and suction. The wall-normal velocity component (v) was on the wall in the interval $184 \leq x \leq 187$ mm specified to $v = A\,cos(\beta_0 z)sin(\omega_0 t)$.

STEP : Generation by stepwise blowing and suction. The wall-normal velocity component was on the wall in the interval $184 \leq x \leq 187$ mm set to vary as $v = A\,step(z)sin(\omega_0 t)$, where the "step" function for each spanwise wavelength has six levels: 1, 0.5, -0.5, -1, -0.5, 0.5. The change-over between the levels were smooth.

DAMP : Generation by blowing and damped suction. The wall-normal velocity component was on the wall in the interval $184 \leq x \leq 187$ mm set to vary as
$v = max(A\,cos(\beta_0 z)sin(\omega_0 t), A\,d\,cos(\beta_0 z)sin(\omega_0 t))$, where $0 \leq d \leq 1$ is a damping factor reducing negative values of the wall-normal velocity at the wall.

The DNS code for the boundary layer geometry is a development of the channel code by Lundbladh, Henningson and Johansson (1992), which has been extensively tested and used. To verify the spatial boundary layer version comparisons has been made with the results reported by Fasel and Konzelmann (1990). It was also possible to compare with linear parallel theory by adding a body force:

$$\mathbf{g} = -\frac{1}{R}\frac{\partial^2 U(x,y)}{\partial y^2}, \tag{12}$$

which produces a parallel mean flow in the whole computational domain.

The box sizes and resolutions used for the simulations presented in this paper are displayed in table 2. The displacement thickness at the position where the oblique waves were generated was 0.83 mm and this was 30 mm downstream of the inflow boundary in all but the FRIN case. The width of the box was set to fit one spanwise wave length of the oblique waves. Since an initial symmetry is preserved by the Navier-Stokes equations we could save computational costs by only calculating one half of each wall parallel (x, z) plane. Box1 was used for the calculations presented in § 3.1.1 and § 3.1.2. The lower forcing amplitude was used to prolong the transition development and clarify the initial part. The flow visualization presented in § 3.1.1 was also made with a lower forcing amplitude. The transition stages and development observed were the same as for the other cases. Box2 was used for the simulations in § 3.1.3 and § 3.2. The flow in Box1

	xl × yl × zl (mm)	nx × ny × nz (resolution)	forcing u_{rms}%
Box1	775× 63× 11.6	1200 × 65 × 96	1.4
Box2	397× 63× 11.6	512 × 65 × 80	2.3
Box3	310× 63× 11.6	512 × 65 × 120	2.3
Box4	310× 63× 11.6	720 × 97 × 192	2.3

TABLE 2. Resolution and box dimensions for the simulations presented. The box dimensions includes the fringe region, which took up 62 mm at the downstream end of the box in all cases. The forcing is given as the u_{rms} of the oblique waves at $x = 217$ mm

and Box2 did not reach as far in the transition process as in the other two boxes and the calculations were therefore over resolved. Box3 and Box4 were used for the results in § 3.3 and § 3.4. The amplitudes of the disturbances and the flow observed in these cases were the same, but the resolution of Box3 was marginal whereas that of Box4 was sufficient.

3. Results

In order to better demonstrate the coherence of experiment and simulations, we do sometimes present data from both investigations in the same figure. In general, we want to give a good description of oblique transition and therefore alternate experimental and DNS results depending on what is most suitable for describing a certain property. The presentation of results is in §3.1 show the basic mechanisms of oblique transition and establish that we observe the same qualitative development in both experiment and calculations. In §3.2 we present a numerical investigation of how the different disturbance generation techniques and changes in the pressure gradient effect the transition scenario. Those results are in §3.3 used to closely model the experiment using the DNS. Finally a combination of numerical and DNS results are used in §3.4 to give a good picture of the late stages of oblique transition.

3.1. Basic Features.

3.1.1. *The emergence of large amplitude streaks.* The dominating feature observed in a flow visualization of oblique transition, is the spanwise periodic streamwise streaks, growing inside the boundary layer (figure 6 *a*). These are associated with regions of low and high speed streamwise velocity and a snapshot of this velocity component from the simulation displays a similar picture (figure 6 *b*). The initially generated oblique waves are noticed as a checkboard pattern of dark and light patches in the left upstream part of both figures. The development of the oblique waves are, however, easier studied when the mean streamwise velocity U is subtracted from the flow field.

(*a*)

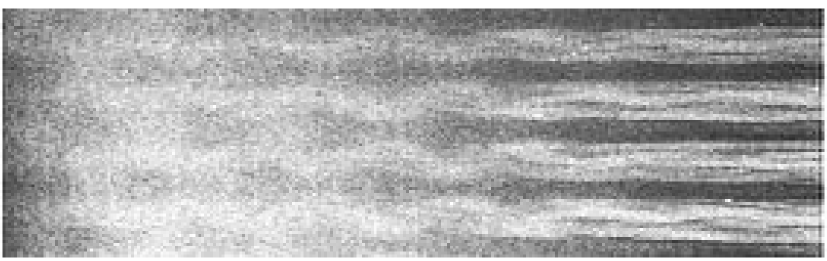

(*b*)

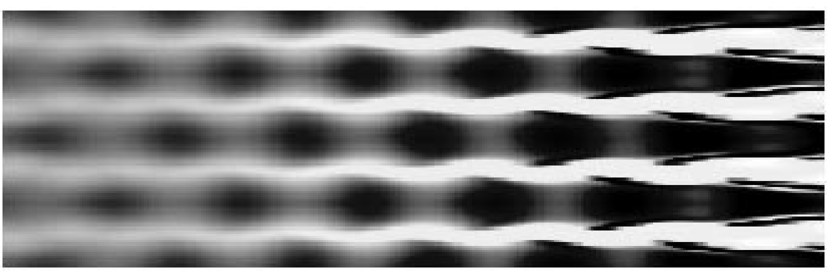

FIGURE 6. (*a*) Photo from flow visualization of oblique transition. (*b*) Instantaneous streamwise velocity from numerical simulation, plane parallel to the wall, flow from left to right

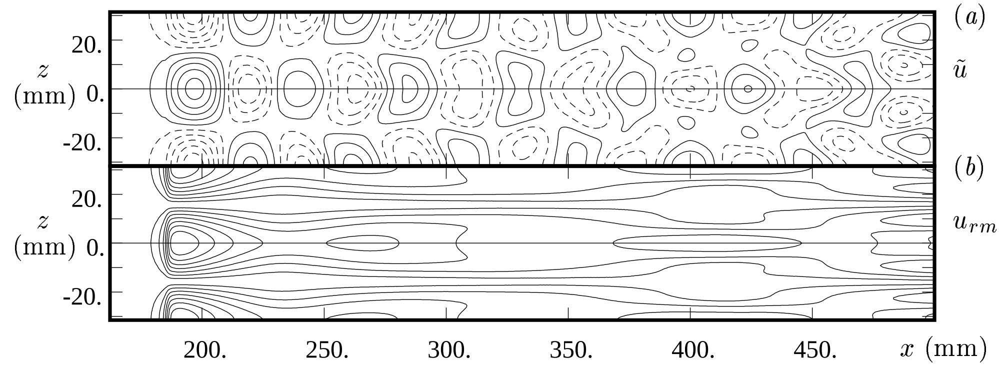

FIGURE 7. (*a*) Fluctuating streamwise velocity at y=0.98 mm, contour spacing 0.005. (*b*) Contours of u_{rms} at y=0.98 mm, spacing 0.0025.

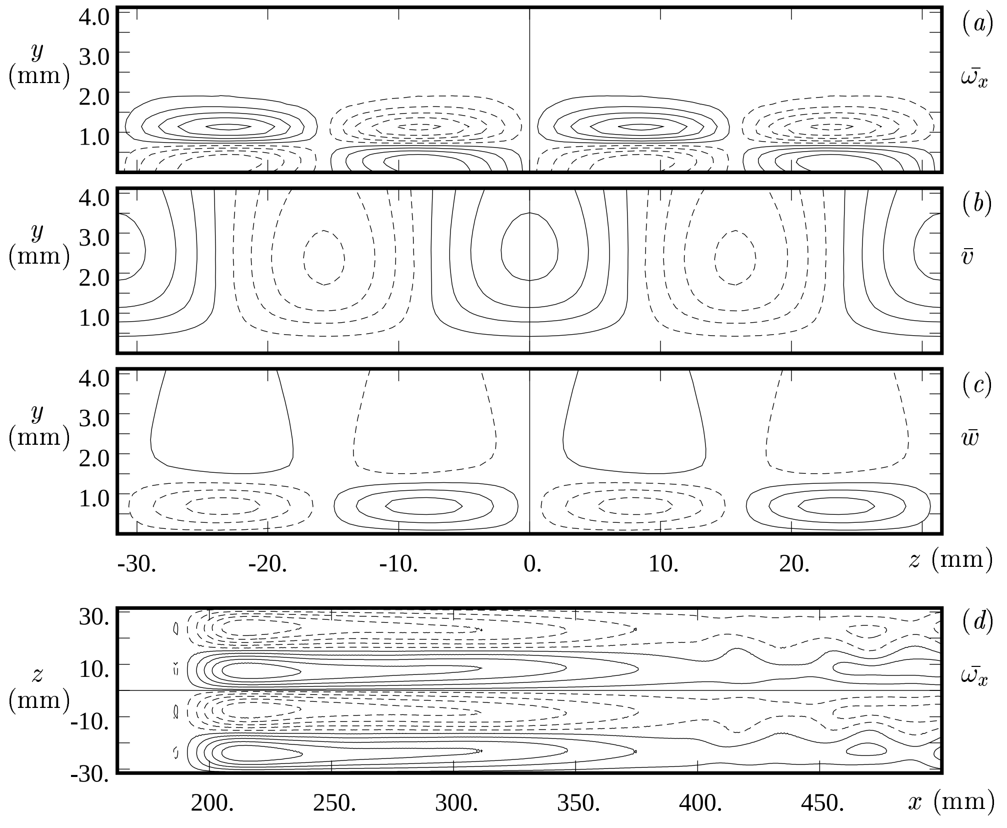

FIGURE 8. Mean quantities from which a laminar Blasius profile has been subtracted. (*a*) Contours of streamwise vorticity with 2×10^{-4} steps. (*b*) Contours of wall-normal velocity with 0.5×10^{-4} steps. (*c*) Contours of spanwise velocity with 2×10^{-4} steps. (*d*) Contours of streamwise vorticity with 2.5×10^{-4} steps. (*a*-*c*) are in the plane $x = 317$ perpendicular to the flow and (*d*) are in wall parallel plane $y = 0.98$ mm.

In figure 7 (*a*), where only the fluctuating part of the streamwise velocity $\tilde{u} = \tilde{u}(t,x,y,z)$ remains, the oblique waves are seen to decay slowly after the generation point. Further downstream the pattern changes as disturbances with higher spanwise wavenumber reach an amplitude comparable to that of the oblique waves. Since the alternating maxima and minima of the oblique waves are aligned in the streamwise direction, the figure of root mean square of the streamwise velocity (u_{rms}) will also show structures aligned in the streamwise direction (figure 7 *b*).

The nonlinear interaction of the oblique waves generates counter rotating streamwise vortices. The time averaged mean of the streamwise vorticity is shown in figure 8 (*a,d*) together with the mean of the wall-normal and spanwise velocity components (figure 8 *b,c*). The spanwise wavelength of the vortex pattern is half that of the oblique waves. The vortices decay downstream, but in spite of that they generate the growing high and low speed streaks by the *lift-up* mechanism described in the introduction. By subtracting the spanwise mean from the mean streamwise velocity in both experiment and simulation and plotting in a plane perpendicular to the flow, comparable figures of the streamwise velocity perturbation are shown in figure 9 (*a,b*). The small arrows symbolize the rotation direction of the associated vortices.

If the amplitude of the initiating oblique waves are to low, the streak amplitude will grow and thereafter decay. For larger amplitudes transition to turbulence will be observed. Figure 10 shows wall-normal profiles of streak amplitude for several downstream positions in the experimental set-up. The shape is the same as the so called Klebanoff mode (Klebanoff 1971, Kendall 1985), which consists of low frequency oscillations observed in boundary layers subjected to free-stream turbulence. The maximum of the profiles are found at a constant y/δ_r. The streak amplitude decreases after $x = 467$ when the disturbance level in the flow

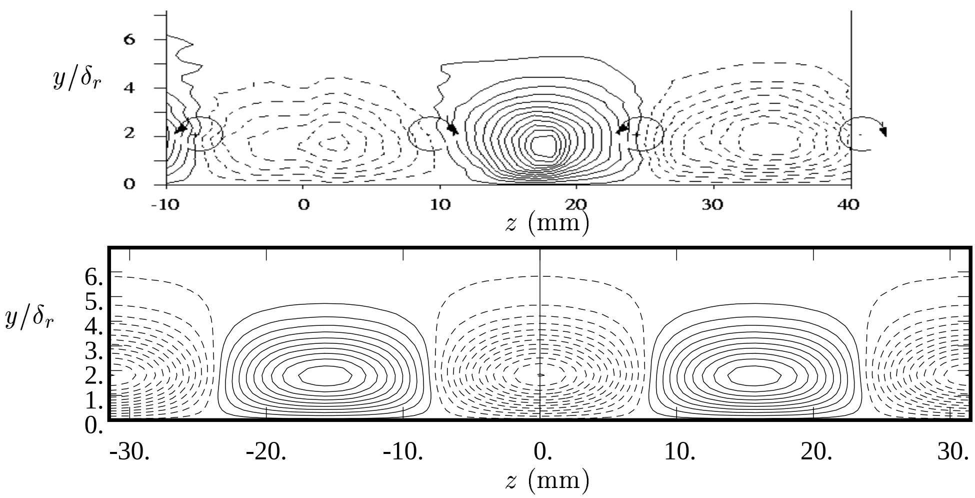

FIGURE 9. Contours of mean streamwise velocity disturbance (*a*) Experiment (*b*) Simulation, solid lines represent positive values and dashed negative values.

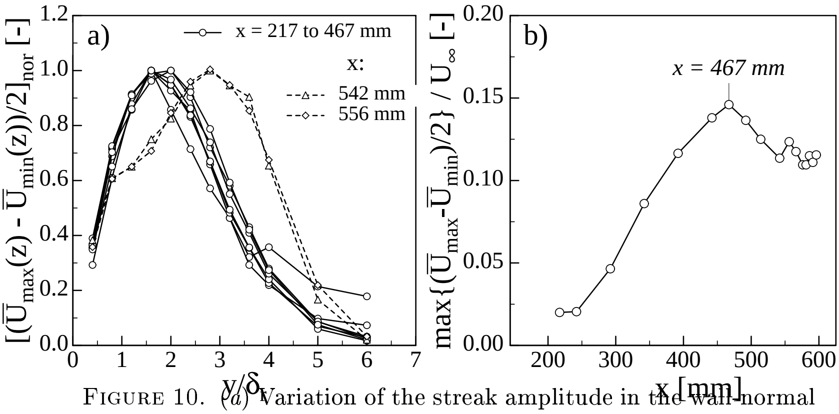

FIGURE 10. (*a*) Variation of the streak amplitude in the wall-normal direction at several downstream positions. (*b*) Development of the streak amplitude in the streamwise direction.

reaches high values (figure 10 *b*) and the maximum of the wall-normal profile moves away form the wall (figure 10 *a*).

3.1.2. *Development of Fourier components.* We transform the velocity fields in time and in the spanwise direction to Fourier space and use the notation (ω, β), where ω and β are the frequency and spanwise wavenumber respectively, each normalized with the corresponding fundamental frequency/wavenumber. Thus the oblique waves are represented by $(1,1)$ and $(1,-1)$ and the streaks by $(0,2)$. In figure 11 the slow decay of $(1,1)$ after the peak at the generation point $x = 186$ is clear as well as the upstream influence of the generation. As the flow is symmetric and (ω, β) equal to $(\omega, -\beta)$, we only show modes with positive β. The first generation of nonlinearly excited modes $(2,0)$, $(2,2)$ and $(0,2)$ are represented by dashed lines and the the second generation modes $(3,1)$, $(3,3)$ and $(1,3)$ are

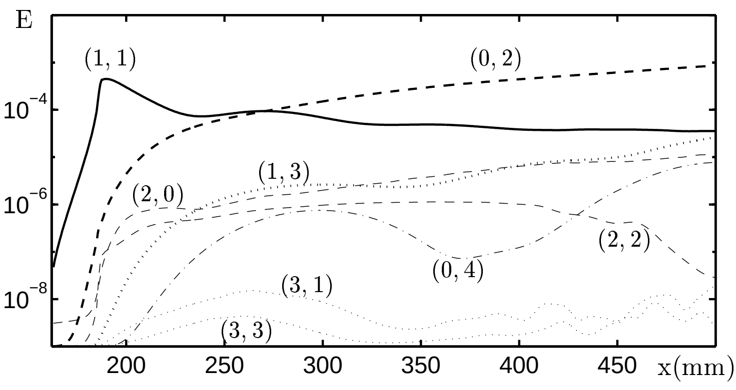

FIGURE 11. Energy in the initially generated Fourier mode $(1,1)$, solid. The modes exited after the first generation of nonlinear interaction $(0,2)$, $(2,2)$ and $(2,0)$, dashed. Modes exited after the second step of nonlinear interactions are dotted, $(1,3)$, $(3,3)$ and $(3,1)$. Dash dotted are $(0,4)$

dotted. According to the results on transient growth, disturbances with zero or low frequency should have the greatest growth potential, which is precisely what we find. The $(0, 2)$ and $(1, 3)$ modes gains approximately two orders of magnitude more energy than the other modes of their respective nonlinear generation. This is also true for the $(0, 4)$ mode which is the only mode of higher nonlinear generation displayed in figure 11. After $x = 350$ the curves representing the $(1, 1)$ and $(1, 3)$ modes approach each other, which is also evident in figure 7 (*a*) were the fluctuating velocity field is gradually complicated by shorter spanwise wavelengths.

3.1.3. *Quadratic dependence of streak amplitude.* In figure 12 the development of the energy in the $(1, 1)$ and $(0, 2)$ modes are compared using simulations with three different initial wave amplitudes. If the amplitudes are scaled with the maximum of $(1, 1)$ for each run (figure 12 *a*), the $(1, 1)$ curves collapses showing the linear relation between the forcing and the downstream amplitude. The energy in $(0, 2)$ for the case with the strongest initial forcing reaches a level where nonlinear saturation occurs at approximately x=400 mm. Scaling with the maximum of $(1, 1)$ squared instead, as in 12 (*b*), the $(0, 2)$ curves collapses up to the downstream position of saturation, showing the quadratic nonlinear generation of $(0, 2)$ from $(1, \pm 1)$.

The same observations can be made in the experiment. It was shown in figure 5 (*b*) that the oblique waves scales linearly with the forcing amplitude of the loudspeakers. That the streak amplitude depends quadratically on the forcing amplitude in the experimental investigation is shown in figure 13, where the streak amplitude at a fixed downstream position is plotted against the square of the forcing amplitude. The experimental curve follows the straight line until the forcing is strong enough to cause nonlinear saturation of the streaks.

In the next section we will discuss how the flow reacts to changes of input parameters and how to understand discrepancies between experiment and simulation.

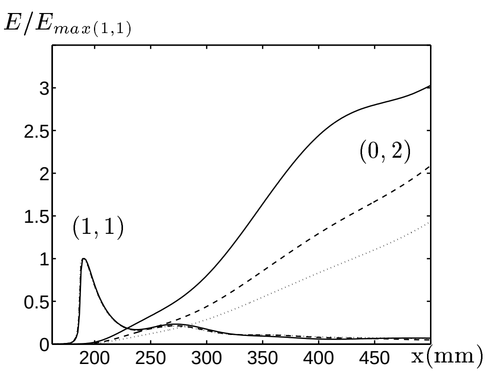

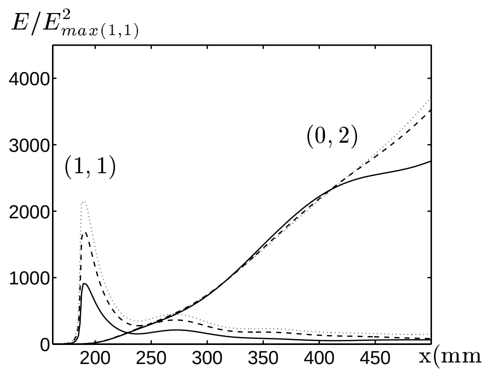

FIGURE 12. Energy in $(1, 1)$ and $(0, 2)$ components from simulations with increasing initial wave amplitude, dotted curves correspond to the lowest amplitude and solid to the highest. (*a*) curves scaled with $max(1, 1)$ (*b*) curves scaled with $max(1, 1)^2$

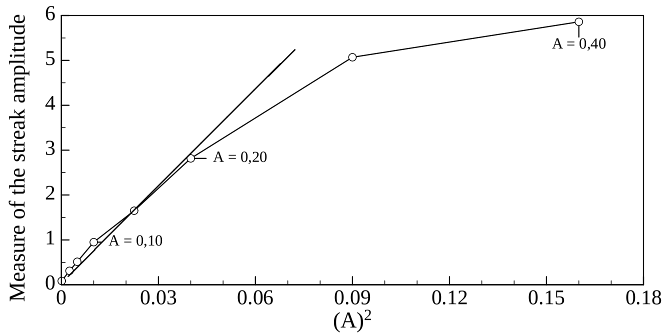

FIGURE 13. Streak amplitude at $x = 478$ in the experiment as function of the squared forcing amplitude of oblique waves, showing the quadratic dependence of the streak response to the forcing. At higher forcing amplitudes the streaks saturate and therefore do not follow the quadratic behavior.

3.2. Dependence of the disturbance evolution on physical and numerical parameters.

3.2.1. *Effects of different disturbance generation methods.*

Rms dependence
Both an experimental and a numerical investigator may consider different designs or methods for disturbance generation. We have therefore compared the five generation methods mentioned in § 2.2 and the experimental results. An experimental correspondence to the FRIN method is hard to think of, but the methods BLOW, STEP and DAMP are certainly connected to experimental blowing and suction devices and the BODY method could be connected to an experiment with vibrating ribbons. Indeed Elofsson and Lundbladh (1994) managed to closely model vibrating ribbons in a channel flow by the use of an oscillating body force.

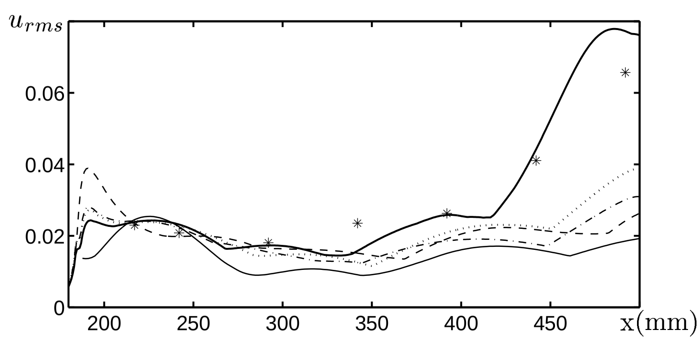

FIGURE 14. Downstream development of u_{rms} for five different generation methods of the oblique waves and experimental results. FRIN, thin; BODY, dashed; BLOW, doted; STEP, dash doted; DAMP, thick; experiment, star.

Figure 14 shows the downstream development of the rms amplitude in the streamwise velocity component (u_{rms}) for the five different generation methods as well as for the experiment. The strength of the generation in the simulations was set such that the maximum u_{rms} at $x = 217$ was equal to the experimentally measured value at that position. The signal in both the experiment and the simulation was filtered to select the generation frequency, and in the following the curves of u_{rms} will only contain that frequency. The difference between the total u_{rms} and the filtered u_{rms} in the simulations presented in this section never exceed 14% and that occurs when the flow is almost turbulent.

The overall downstream development of u_{rms} is similar for all five cases, despite the fact that the initial development strongly depends on the type of forcing and that matching was done at a single downstream position. The curve for the FRIN case lies slightly below the others and u_{rms} grows significantly more after x=400 mm in the DAMP case. The damping factor of suction in the DAMP simulation presented in this section was $d = 0.4$.

Rms modes and their phase

In frequency-wavenumber space the modes contributing to the filtered u_{rms} will be $(1, \beta)$, where β is any integer. Note that as the flow is symmetric the modes (ω, β) and $(\omega, -\beta)$ have the same amplitude and in the following the we will denote the sum of these modes by $(1, \pm\beta)$. We find that the dominating modes are $(1, \pm1)$, $(1, \pm3)$ and $(1, \pm5)$. Figure 15 shows u_{rms} and the rms of the mentioned modes of the BLOW case together with the phase difference between the $(1, 1)$ and the $(1, 3)$ modes. The generated $(1, \pm1)$ mode decays downstream but

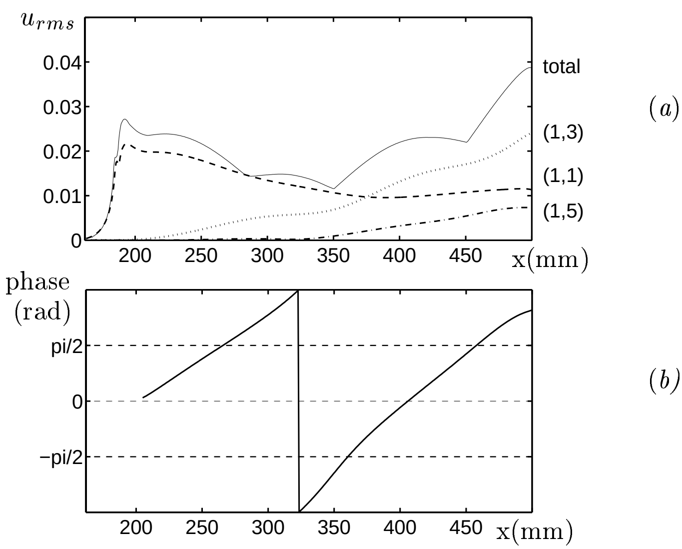

FIGURE 15. (*a*) Filtered u_{rms} and rms of the $(1, 1)$, $(1, 3)$ and $(1, 5)$ modes for a case with oblique waves generated by blowing and suction, BLOW. (*b*) Phase difference between the $(1, 1)$ and $(1, 3)$ modes. Note the correspondence between zero and $\pm\pi/2$ phase shift and the local extrema in the u_{rms} curve.

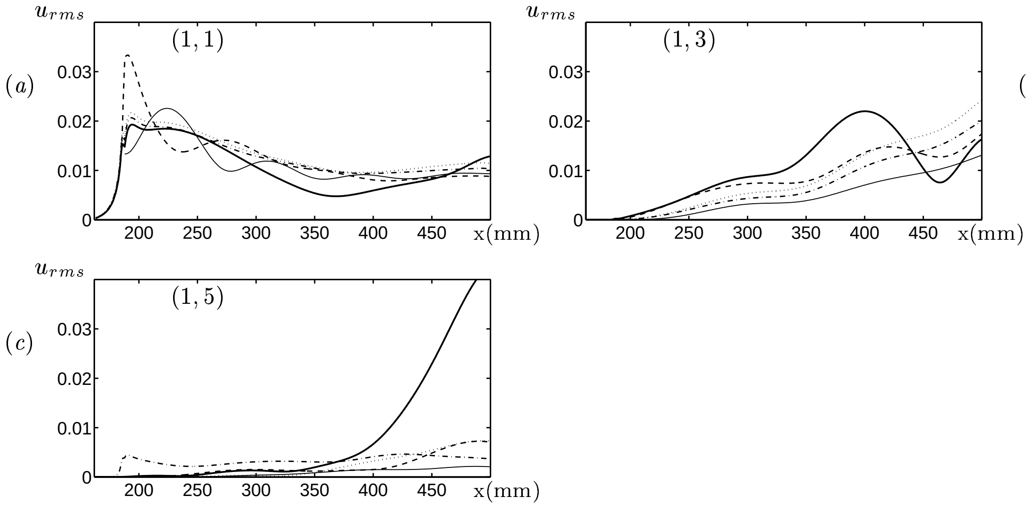

FIGURE 16. u_{rms} for various modes (a) $(1, \pm 1)$ mode (b) $(1, \pm 3)$ mode (c) $(1, \pm 5)$ mode and different generation methods FRIN, thin; BODY, dashed; BLOW, doted; STEP, dash doted; DAMP, thick.

the $(1, \pm 3)$ and $(1, \pm 5)$ modes grows and after $x = 380$ $(1, \pm 3)$ dominates. The phase relation explains the local extrema appearing in the u_{rms} curve, where a minimum appears when the phase shift is $\pm \frac{\pi}{2}$ and a maximum when it is 0. The extremum is sometimes slightly off the location with $\pm \frac{\pi}{2}$ or 0 phase shift, which is caused by the fact that $(1, 1)$ mode is decaying and the $(1, 3)$ increasing.

To further study the differences between the generation methods, the dominating frequency-wavenumber modes are compared in figure 16. It is clear that the downstream differences in the filtered u_{rms} are accounted for by the higher modes $(1, \pm 3)$ and $(1, \pm 5)$. Particularly the strong growth in the DAMP case is associated with the $(1, \pm 5)$ modes. The BODY and DAMP cases initially generates more of the $(1, \pm 3)$ modes and there is a significant generation of $(1, \pm 5)$ initially in the STEP case. Comparing with the experimental results one finds that generation with a stepwise amplitude variation in the spanwise direction is necessary to get close agreement. This is illustrated in figure 17 where the spanwise variation of both u_{rms} and the phase is plotted. The u_{rms} curve for both the

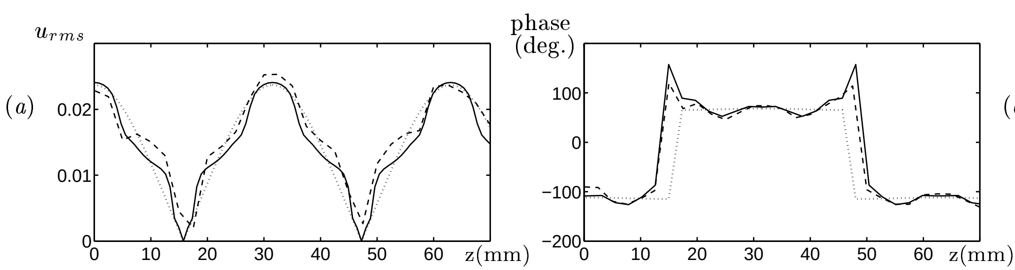

FIGURE 17. Spanwise variation of u_{rms} (a) and phase (b) form STEP (solid), experiment (dashed) and BLOW (dotted).

experiment and the STEP simulation show a typical bottle shape, caused by the $(1,5)$ mode. Results from a simulation with a sinusoidal spanwise blowing and suction has been included in the figure as reference and this has a square-wave like phase curve, to compare with the curves including sharp peaks corresponding to the stepwise results.

Streak dependence

The differences in generation of the oblique waves and the growth of the *rms*-modes will obviously influence the growth of the streaks amplitude, which we define at each downstream position as $max_y(max_z(\bar{U}) - min_z(\bar{U}))$. As we consider the meanflow, the modes in frequency-wavenumber space that are associated with the streak amplitude will be $(0,\beta)$, β being any integer. In figure 18 (*a-d*) the downstream development of the streak amplitude and the three most important streak modes $(0,2)$, $(0,4)$ and $(0,6)$ are plotted for the five different generation methods. The $(0,2)$ mode is dominating but in the DAMP case the growth of the streak amplitude increases suddenly at $x = 440$ and this rise is caused by the growth of $(0,4)$ and $(0,6)$. The $(0,2)$ mode for this generation method does not grow after $x = 350$ and it is generated initially. The initial generation of $(0,2)$ is a clear difference from the other methods, but is in better agreement with the experiment, which also has a higher amplitude at the generation point apart from growing more rapidly downstream. Generation by stepwise blowing and suction generated the $(1,5)$ mode and the nonlinear interaction of $(1,5)$ and $(1,1)$ transfers energy to the $(0,6)$ mode, which is observed to have an amplitude from the generation point in figure 18 (*d*). This accounts for the difference in amplitude between the streak and the $(0,2)$ mode initially.

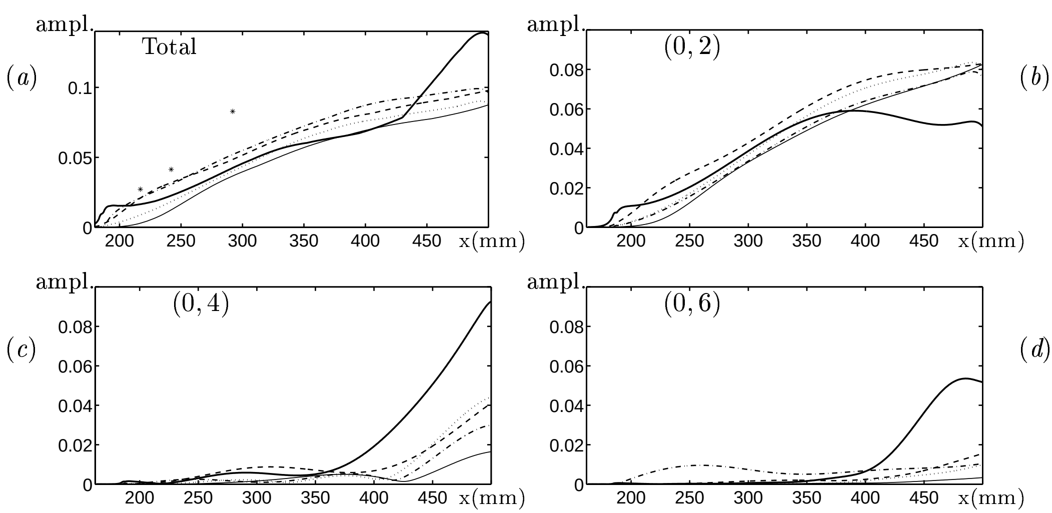

FIGURE 18. (*a*) Streak amplitude, (*b*) $(0,2)$ mode, (*c*) $(0,4)$ mode and (*d*) $(0,6)$ mode for different generation methods. FRIN, thin; BODY, dashed; BLOW, doted; STEP, dash doted; DAMP, thick; experiment, star.

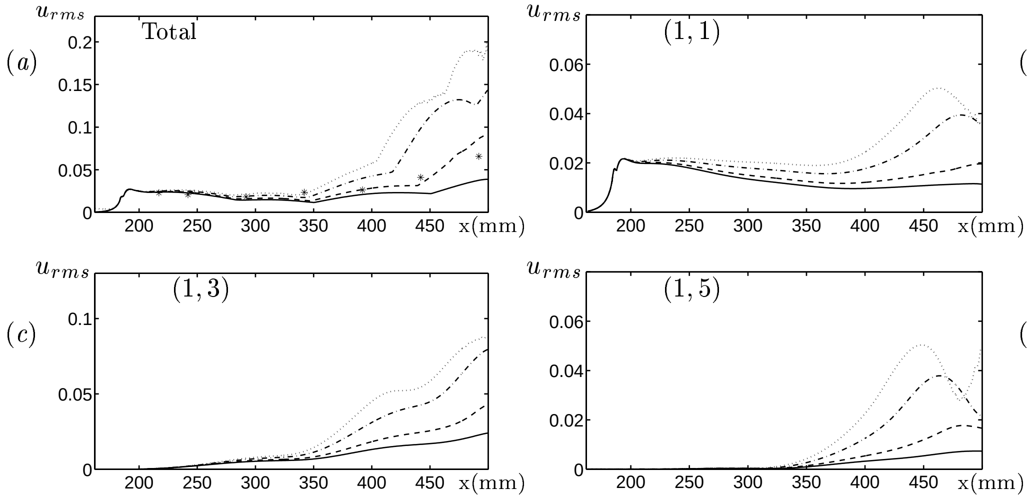

FIGURE 19. (*a*) u_{rms} (*b*) $(1,1)$ mode (*c*) $(1,3)$ mode for simulations with different pressure gradient and experiment. Zero pressure gradient, thick; increasing adverse pressure gradient from dash, dash-dotted to dotted; experiment, star.

3.2.2. *Effects of pressure gradient.* The investigation of disturbance generation did not explain the discrepancy in the streak growth observed in figure 18(*a*), something that could be caused by a slight mean pressure gradient in the experiment. We observed that the $(1,\pm1)$ modes decayed faster in the simulations than in the experiment (figure 14) and therefore chose a positive pressure gradient. That will decrease the damping of the oblique waves and thereby increase the forcing of the streaks. Three simulations with Falkner-Scan flow were performed, where the exponent m in equation 11 was set to -5.525×10^{-3}, -1.370×10^{-2} and -1.907×10^{-2}. The oblique waves were generated by blowing and suction with a sinusoidal spanwise distribution. Figure 19 (*a*) shows the the filtered u_{rms} as function of downstream position for the zero pressure gradient case and the experiment, together with the three cases with pressure gradient. An increased adverse pressure gradient indeed decreases the damping of the $(1,1)$ mode associated with the u_{rms} curve and increases the growth of the higher modes dominating after $x=350$ (figure 19 *b*-*c*). The increased growth of higher modes is caused both by the stronger forcing from the less damped oblique waves and the change of pressure gradient and this is also noted in figure 20 (*a*-*c*) displaying the streak amplitude and the associated modes. Although a faster downstream development is caused by a positive pressure gradient, the qualitative characteristics of the transition scenario is not altered by the pressure gradient. We note that the experimental data for u_{rms} up to $x=350$ agrees better with the simulation, having higher positive pressure gradient, and the corresponding curve of streak amplitude also gives the closest agreement, although it is still under predicted.

(*a*) (*b*)

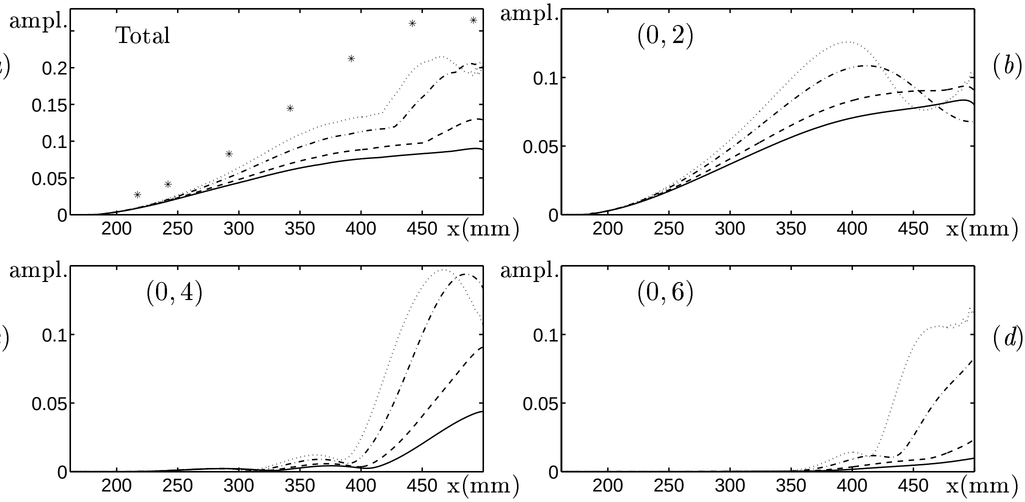

(*c*) (*d*)

FIGURE 20. (*a*) streak amplitude (*b*) (0, 2) mode (*c*) (0, 4) and (*d*) (0, 6) mode for simulations with different pressure gradient and experiment. Zero pressure gradient, thick; increasing adverse pressure gradient from dash, dash-dotted to dotted; experiment, star.

3.3. Detailed Modeling. The results on how the generation method and a pressure gradient influence the studied transition scenario, will in this section be used to model the experiment closely. Using blowing and suction is obvious since that was used in the experiment. The good agreement in the u_{rms} between the simulations and the experiment given by the STEP method was shown already in figure 17. Moreover, in figure 20 (*a*) one observes that the streak amplitude in the experiment starts at a higher level than the curves from the simulations. An increase in initial streak amplitude was observed when the DAMP method was used in figure 18 (*a,b*) and consequently a damping factor for suction of 0.7 was used for the results presented in this section. A pressure gradient was specified to get good agreement between experiment and simulation results for the growth of the $(1, \pm 1)$ modes the first 150 millimeters. Only a very small pressure gradient was observed in the experiment but other flow characteristics could explain the larger growth rates observed in the experiment. Klingmann *et al.* (1993) for example concluded in their investigation of the stability of Tollmien-Schlichting waves that an unsuitable leading edge often explained high growth rates observed in experiments.

Figure 21 displays the downstream variation of u_{rms} and the streak amplitude for both the experiment and a simulation using the above stated parameters. The agreement is excellent to $x = 320$ for u_{rms} and to $x = 340$ for the streak amplitude. Further downstream the pressure gradient cause earlier transition in the simulation. Therefore the later stages of the breakdown process occur at earlier streamwise positions than in the experiment. Thus a comparison of features from a particular stage in the transition process will have to occur at different streamwise positions in experiment and simulation. In figure 22 the

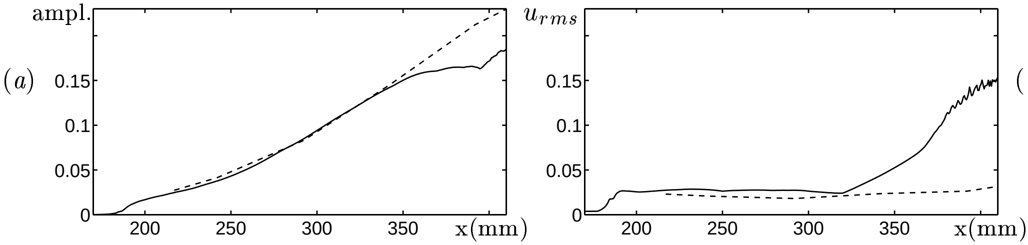

FIGURE 21. (a) streak amplitude (b) u_{rms} of experiment (dashed) and simulation (solid) with closely modeled generation mechanism and pressure gradient to match initial u_{rms} development.

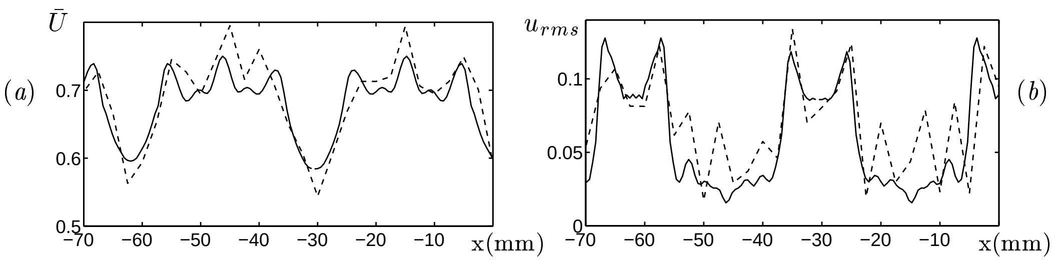

FIGURE 22. Spanwise variation of (a) $\bar{U}$ and (b) u_{rms} of experiment (dashed) and simulation (solid) with closely modeled generation mechanism and pressure gradient to match initial u_{rms} development. Because of the earlier transition in simulation, downstream positions were chosen to get equal maximum of u_{rms}. The downstream positions were $x = 391$ in the simulation and $x = 514$ in the experiment.

spanwise variation of u_{rms} and $\bar{U}$ are compared at downstream positions where the transition process has reached the same stage, i.e. where the maximum of u_{rms} are the same in both simulation and experiment. The mean and rms values at $x = 391$ in the simulation are compared with the corresponding values at $x = 514$ in the experiment. The agreement shown requires that amplitude and phase of all involved modes have the correct relations and is achieved thanks to the close modeling of the generation device for oblique waves. The difference in streak amplitude in figure 22(a) is smaller than that observed in figure 20(a). The reason for this is that the streak amplitude in the experiment decays after $x = 467$ (figure 10b).

3.4. Final Breakdown.

3.4.1. *The onset of high frequency fluctuations.* The last figures (figure 22 a,b) of the previous subsection shows that the peaks of u_{rms} appears where the spanwise gradient of $\bar{U}$ has its maximum. This is different from the early stages of oblique transition where u_{rms} is dominated by the oblique waves and therefore lies in the middle of the low speed streaks (cf. figure 7). The meandering streaks displayed in the flow visualization (figure 6) indicates that large u_{rms} values

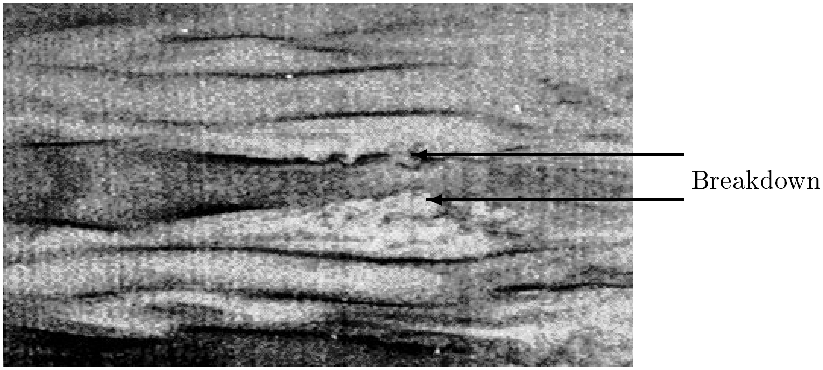

FIGURE 23. Late transition state from flow visualization of oblique transition. Observe that turbulent high frequency oscillations are first formed at the spanwise edge of the streaks.

are produced, as the boundary between high and low speed fluid oscillates in the spanwise direction. A close up of the streaks in the flow visualization also displays the first turbulent high frequency oscillations just where the color of the smoke pattern changes from black to white (figure 23).

The distribution of u_{rms} in a plane perpendicular to the flow is presented in color scale for both simulation and experiment in figures 24 (a,b). The experimental data are taken from $x = 566$ and the simulation results at $x = 410$, a difference that again is attributed to the earlier transition in the simulation. A

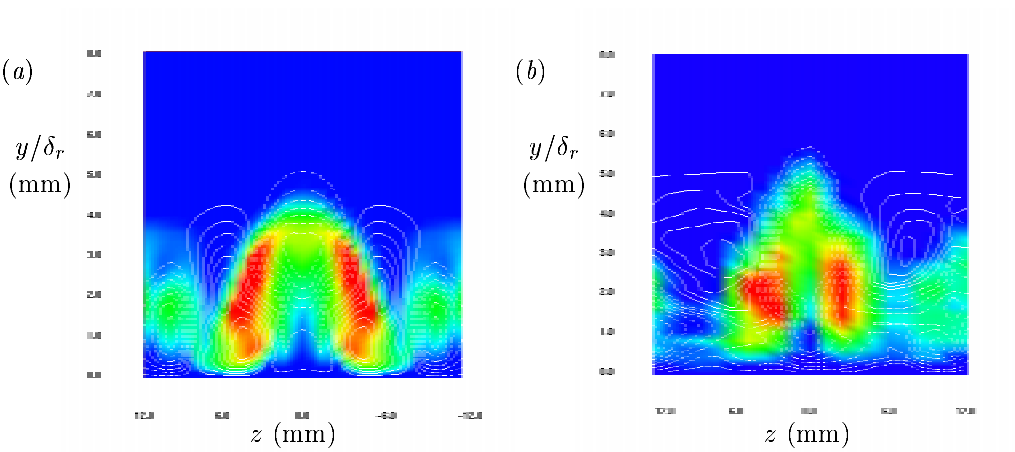

FIGURE 24. u_{rms} represented by colors in a scale from blue-minimum to red-maximum in a plane perpendicular to the flow. White contours represent $\bar{U} - mean_z(\bar{u})$ solid contours positive values and dashed contours negative values. Simulation data are from $x = 410$ and the experimental data from $x = 566$, as transition is earlier in the simulation.

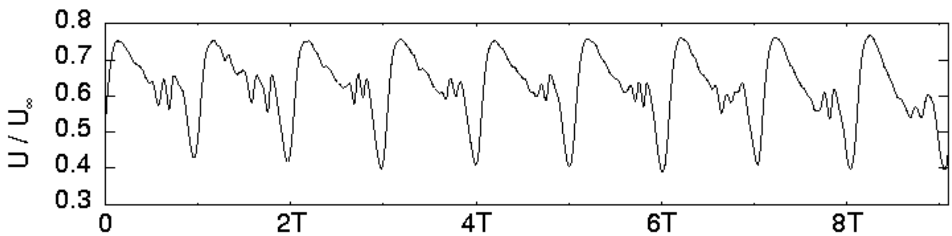

FIGURE 25. Timesignal at z= -2.5 mm, x_v=566 mm, y/δ_r= 1.55

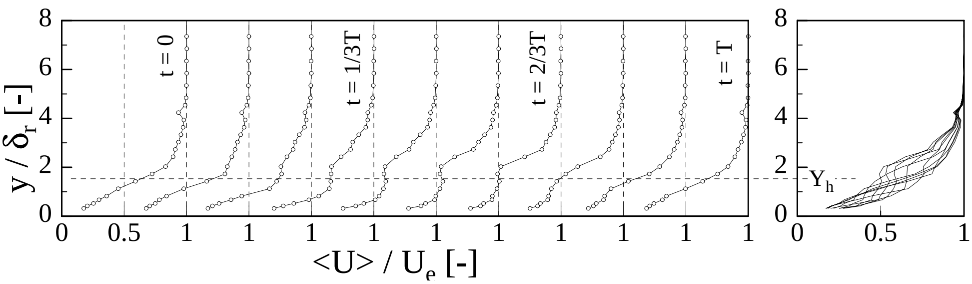

FIGURE 26. Instationary phase averaged mean velocity profiles, x_v=566 mm, z=-2.5.

characteristic symmetric structure with two legs, each containing a maxima of u_{rms}, joined at their upper half is identified in both figures. The figures also include contours of $\bar{U} - mean_z(\bar{U})$ and the shear is found to be high in regions where the maxima of u_{rms} are situated. It is important to note that it is not only the spanwise shear that is high, which was clear already in figure 22, but also the wall-normal shear. The wall-normal and spanwise positions, where the peaks of u_{rms} are found, are the same as those where the first appearance of high frequency oscillations were detected by a hotwire. A timetrace from the experiment at such a position is presented in figure 25, where each fundamental cycle contains high frequency oscillations. A spectral analysis reveals both high amplitude of several subharmonics and range of amplified frequencies at approximately 800 Hz. In the phase averaged streamwise velocity profiles collected at different phases during a fundamental time period in the experimental investigation (figure 26), we find inflectional profiles. The position of inflectional profiles coincide with the positions where we found the peaks of u_{rms} and the high frequency oscillations. The inflectional profiles were only present during a part of a time period, the same was true for the high frequency oscillations.

3.4.2. *Flow structures.* It is interesting to relate the statistical quantities and the instantaneous observations discussed above, to structures appearing in the flow during transition. In figure 27 positive and negative isosurfaces of instantaneous streamwise vorticity are displayed in yellow and green respectively. At

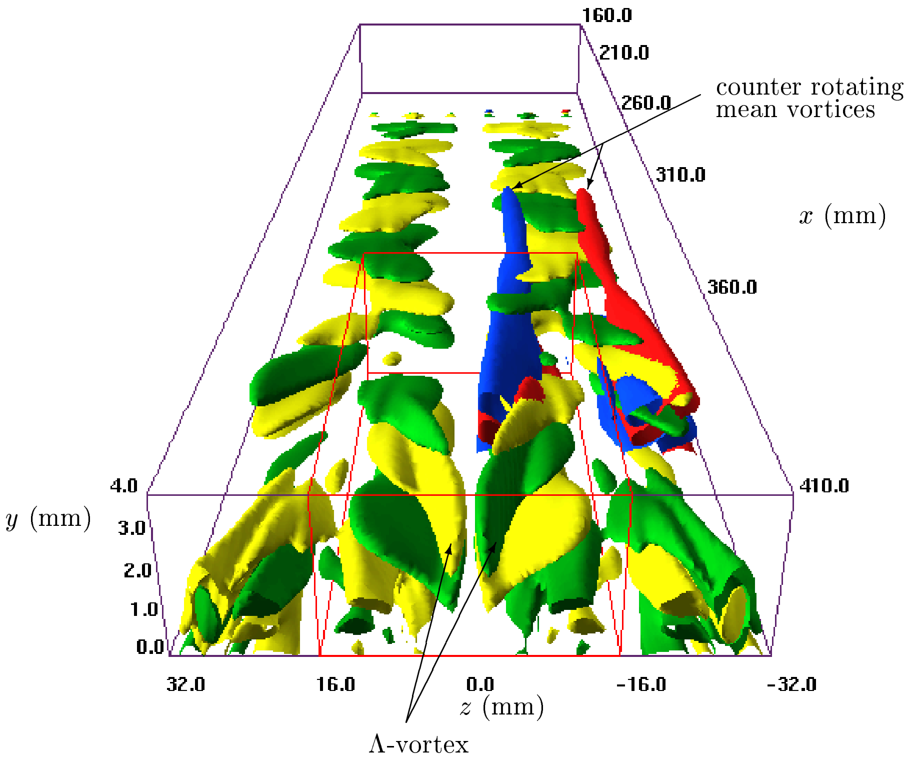

FIGURE 27. Isosurfaces of positive and negative instantaneous streamwise vorticity are colored yellow and green respectively. Note the formation of a Λ-vortex at the downstream part of the box. A pair of counter rotating vortices are displayed as red and blue surfaces representing positive and negative mean of streamwise vorticity, respectively.

$x = 200$ a spanwise row of small surfaces reveal where the wave generator is situated. The oblique waves are then seen as streamwise rows of alternating positive and negative vorticity. When the flow evolves downstream the patches of vorticity are gradually divided (x=360 mm). Groups of three surfaces overlapping each other, are separated alternately to the left and to the right. Two such groups, of three surfaces, from neighboring rows form new groups, in which we can identify the middle pair of surfaces as counter rotating vortices forming a Λ-shaped structure. The two pairs of surfaces above and below does not represent vortices

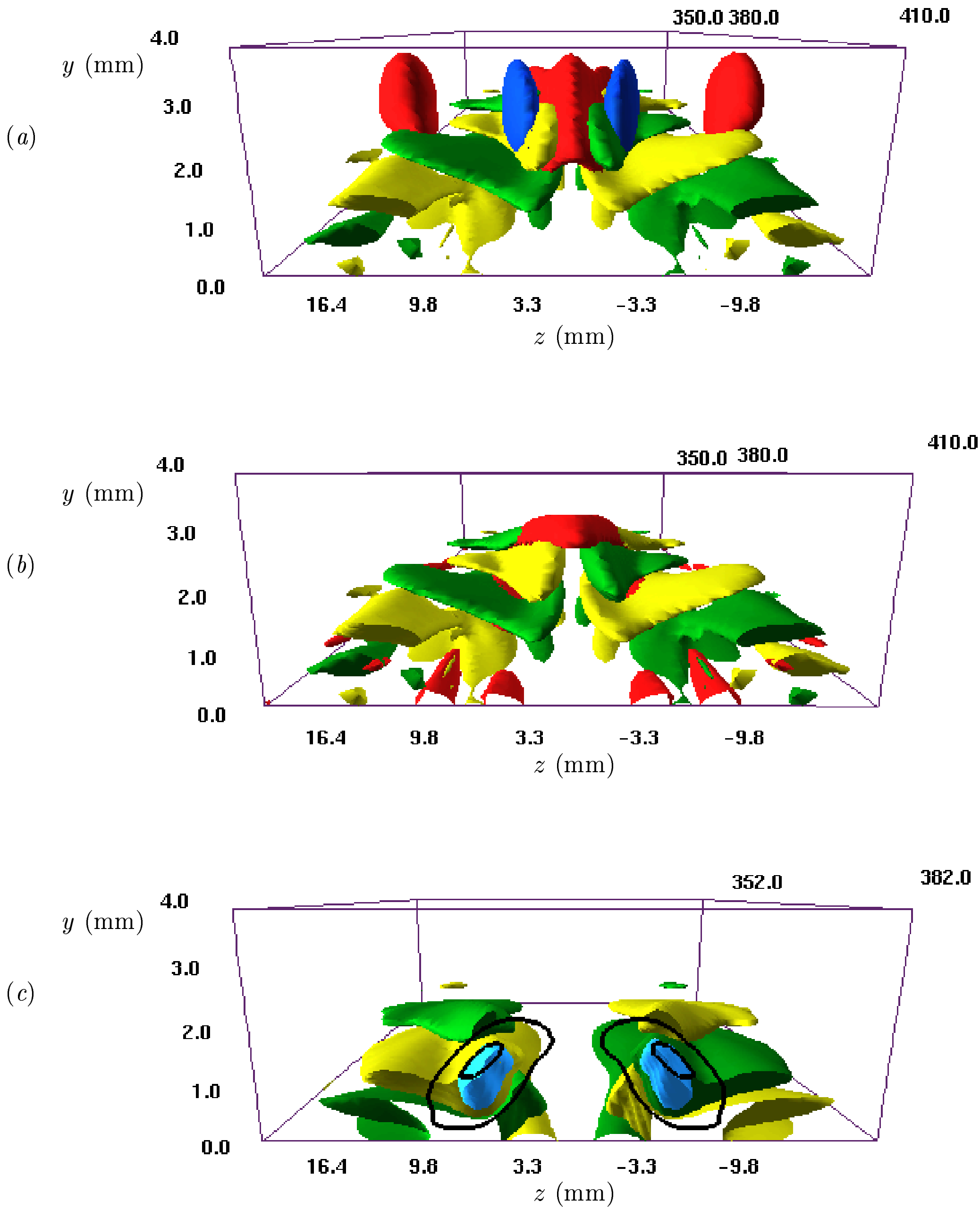

FIGURE 28. Isosurfaces of positive and negative instantaneous streamwise vorticity are colored yellow and green respectively. In (*a*) the red and blue surfaces represents constant positive and negative value of the wall-normal disturbance velocity respectively. In (*b*) and (*c*) The red and blue surfaces represent constant positive and negative values respectively of the wall-normal shear of the streamwise disturbance velocity, isolines are constant u_{rms}.

but regions of high wall-normal shear, $\partial w/\partial y$. Observe that there is no spanwise vortex connecting the legs of the Λ-vortex, which is natural since the legs has developed independently and thereafter been drawn towards each other. The red and blue surfaces in figure 27 represent positive and negative mean streamwise vorticity. It is that motion that creates the low and high speed streaks in the streamwise velocity and it is also responsible for the observed splitting of the instantaneous vorticity patches. In the first portion of the box the red and blue structures are mainly what we previously have called $(0, 2)$ mode and the yellow and green structures correspond to the $(1, \pm 1)$ mode. In the downstream region of the box the mean streamwise vorticity surfaces instead tend to be a trace of the instantaneous vorticity structures.

In figures 28 the structure inside the smaller red box in figure 27 are studied. The green and yellow surfaces are the same in the figures 27–28 and in figure 28 (*a*) the red and blue surfaces represents positive and negative wall-normal disturbance velocity respectively. With disturbance velocity we mean that the laminar velocity has been subtracted. The original checkboard pattern of positive and negative wall-normal velocity disturbances has here been deformed by the Λ-vortex. It has strengthened the upwash in the middle of the structure, which creates the strong shear-layer observed in figure 28 (*b*). In that figure the red surfaces represent the wall-normal shear of the streamwise disturbance velocity. One observes both a high shear-layer riding on top of the Λ-vortex and strong shear-layers underneath the Λ-vortex. The lower shear-layers start at the wall and follow the Λ-vortex upwards. They are caused by fluid with high streamwise velocity brought down by the negative wall-normal velocity (blue surfaces in figure 28 *a*). In figure 28 (*c*) the Λ-vortex has been cut and inside it, surfaces of minimal wall-normal shear of the streamwise velocity are displayed. That $\partial u/\partial y$ has a local minimum means that there is a inflectional velocity profile at that position. The isocurves at the face of the box in figure 28 (*c*) represents constant u_{rms} in that plane. The results are consistent with the experimental results showing the highest u_{rms} values in the region where we find the inflectional profiles.

4. Discussion

The structures that we have identified in the late state of oblique transition have many similarities with those previous investigators have found in K- and H-type transition. We find for example Λ-vortices with the strong shear-layers on top, streamwise vortices deforming the mean flow and inflectional profiles. Structures are easier to extract from numerical simulations and comparisons can be made with the spatial simulation of K-type transition by Rist & Fasel (1995) or the temporal simulations of both K- and H-type transition by Laurien & Kleiser (1989). Detailed flow structures of both K-type and H-type transition are also reported for channel flow by Krist & Zang (1986), Zang & Krist (1989) and others. Experimental investigators reporting details of the flow structures before breakdown are for example Williams, Fasel & Hama (1984) for K-type and Corke & Mangano (1989) for H-type transition.

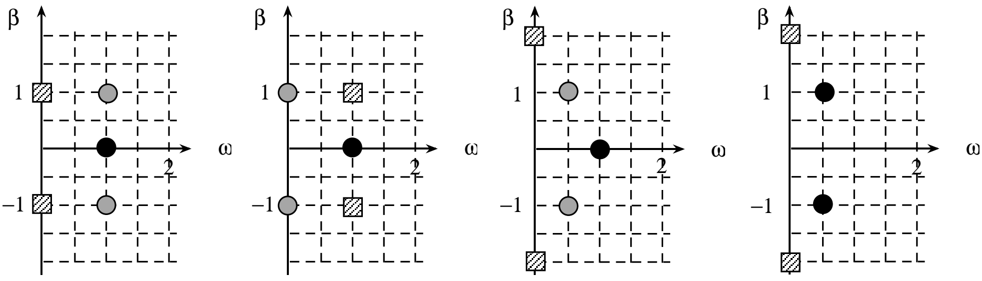

FIGURE 29. Graphs displaying the relation between the most important modes in (*a*,*b*) K-type, (*c*) H-type and (*d*) oblique transition. Modes marked with black dots are initiated with main amount of energy. Grey dots symbolize modes initiated with a small amount of energy and squares represent modes that are generated nonlinearly and are vital in the transition process or for what is observed at the late stages of transition.

There are differences between the three transition scenarios. The most important difference lies in the initial condition. Oblique transition does not need any two-dimensional TS-wave nor does such a mode grow during transition. The factor that causes the similarity between the different transition scenarios are the interaction of the oblique waves with counter rotating streamwise vortices.

The initial conditions of the important modes for the three transition scenarios are indicated in diagrams 29 (*a*-*d*). Black dots marks the modes where the largest initial energy is introduced in the flow. Grey dots mark modes that are initiated with a smaller amount of energy and finally squares represent vital modes that are generated nonlinearly from the initially exited modes. Figures 29 (*a*, *b*) represent the K-type scenarios with the main initial energy in the $(1,0)$ mode. In 29 (*a*) the oblique modes $(1,\pm1)$ are also initiated as it is done in many numerical simulations. The counter rotating vortices with associated streaks $(0,\pm1)$ that causes the spanwise modulation of the flow are in this case generated nonlinearly. In experiments it is usual to initiate the vortices/streaks and the TS-wave and let the oblique modes be generated nonlinearly, which is illustrated in figure 29 (*b*). The $(1,\pm1)$ modes in figures 29 (*a*, *b*) also generate the $(0,\pm2)$ modes, but with a small amplitude compared to the interaction of $(1,0)$, $(1,\pm1)$ and $(0,1)$. Even so the $(0,\pm2)$ modes can grow to a amplitude comparable to that of the $(0,\pm1)$, as it does at the late stages in the computations by Laurien & Kleiser (1989). The initial conditions for H-type transition are described in figure 29 (*c*), with the main initial energy still in the $(1,0)$ mode and with a small amount in the subharmonic $(1/2,\pm1)$ modes. The vortex-streak modes of importance now are $(0,\pm2)$, which are nonlinearly generated by the subharmonic modes. Finally oblique transition is described in figure 29 (*d*). The two-dimensional TS-mode $(1,0)$ is excluded and the initial energy is instead only introduced in the oblique waves $(1/2,\pm1)$. The vortex-streak modes $(0,\pm2)$ are generated nonlinearly exactly as in H-type transition, but the energy in the oblique waves are higher and consequently the forcing of the vortex-streak mode

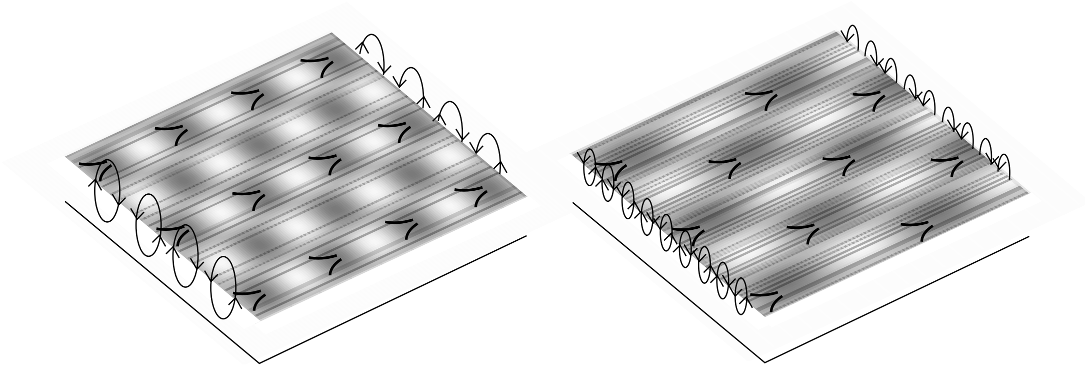

FIGURE 30. Relation between oblique waves, Λ-vortices and streamwise vortices for (*a*) K-type transition (*b*) H-type transition and oblique transition. The wall-normal velocity component of the oblique waves are represented by the grey scale pattern, where dark means positive and bright negative velocity. The arrows on the circles indicate the rotation direction of counter rotating streamwise vortices. Solid and dashed lines are contours of the wall-normal velocity associated with the vortices. Positions where Λ-vortices appear are marked by the black Λ symbols.

stronger. Therefore the streaks are captured in a flow visualization rather than the Λ-vortices as for H-type transition. The naming of modes is of course just a matter of normalization and in an attempt to simplify the comparison, oblique transition in this discussion involve modes $(0, \pm 2)$ and $(1/2, \pm 1)$, whereas we previously have called these modes $(0, \pm 2)$ and $(1, \pm 1)$.

With the sketches in figure 30 we illustrate the late stages of the three transition scenarios. The flow is from left to right and the gray shading represents the wall-normal velocity of oblique waves, dark for positive and bright for negative. The circles with arrows symbolize streamwise elongated counter rotating vortices, with the rotation direction indicated by the arrows. Contours of the wall-normal velocity associated with the vortices are also included in the figures. Solid contours indicate positive and dashed negative wall-normal velocity. The wall-normal motion will create streaks with low and high streamwise velocity, appearing where the solid and dashed contours are respectively. In 30 (*a*) the streamwise and spanwise scale of the oblique waves are the same and the spanwise wavelength of the vortex pattern is the same as that of the oblique waves. These conditions correspond to K-type transition also shown in figure 29 (*a, b*). Λ-vortices will appear at positions where the oblique waves produce a maximal wall-normal velocity *and* the the vortices produce positive wall-normal velocity. Aligned black lambdas mark where these conditions are met. The conditions shown in 30 correspond to oblique and H-type transition, with twice the streamwise scale of K-type transition and the spanwise wavelength of the vortices halved (cf. figure 29 *c, d*). The staggered Λ-vortices are marked using the same criteria as in figure 30 (*a*).

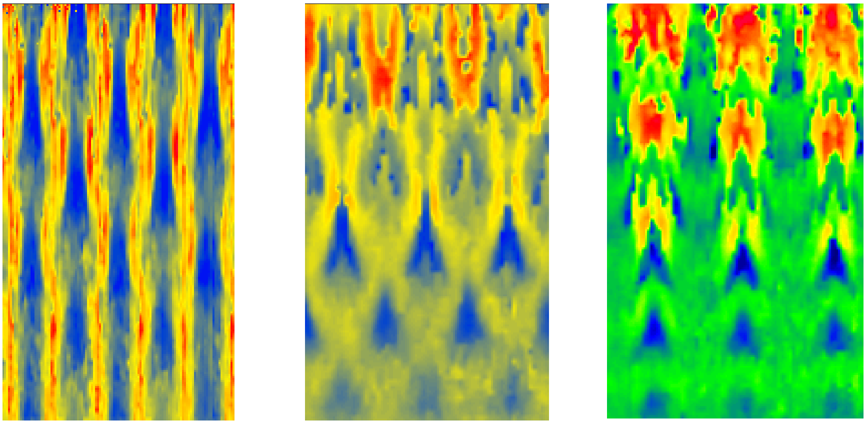

FIGURE 31. PIV pictures from three transition scenarios, from left to right: oblique transition, H-type transition and K-type transition. The flow direction is from the bottom to top of the figures. Both Λ-shapes and streaks can be observed in all three scenarios.

PIV measurements from the three transition scenarios are compared in figure 31. Both streaks and Λ-shapes can be observed in all three figures but the amplitude relation between them differ.

5. Conclusions

We have performed both physical experiments and numerical simulations of oblique transition, a transition scenario initiated by two oblique waves only. In this first experiment of oblique transition in an incompressible boundary layer, blowing and suction was used to generate the oblique waves. Hot-wire measurements as well as flow visualizations with a laser technique were used to analyze the physical flow. The experiment verified earlier computational and theoretical results. The oblique waves interacted nonlinearly and a spanwise variation of the meanflow was observed with alternating high and low streamwise velocity streaks. The streaks grew downstream in a manner consistent with the theories on non-modal growth. Efforts were made to closely model the experiment in the numerical code and five different methods for disturbance generation were compared. They all produced qualitatively similar transition scenarios but important differences were also found. The closest agreement with the disturbance generated by the experimental device was found when we used a blowing and suction technique, where the amplitude of the wall-normal velocity changed stepwise in the spanwise direction and the suction amplitude was 70% of the blowing amplitude. The effect of a positive pressure gradient was also investigated numerically and was found to move all stages of the transition scenario upstream. Imposing a positive pressure gradient in the simulation decreased the initial damping of oblique waves to better correspond to the experimental development. This resulted in a faster growth of the streak amplitude, which was also in agreement with the experiment, but the computed flow was in this case found to reach a turbulent stage upstream of the corresponding stage in the experiment. Mean streamwise vortices generated by the oblique waves and causing the growth of the streamwise streaks were found in an examination of the flow structures. This examination also identified high shearlayers riding on top of Λ-shaped vortex pairs at a late transition stage. Inflectional flow profiles were found in both experiments and simulations and their position coincided with the Λ-shaped vortex pairs. This was also the region where the peak of u_{rms} was found and high frequency oscillations in the experimental time traces. The identified structures were similar to those reported by both numerical and experimental investigators of K- and H-type transition. These similarities are explained by the common feature of all three transition scenarios, namely oblique waves and streamwise vortices.

The authors greatly acknowledge the contributions of all colleagues inspiring this work with discussions, especially Peter Schmid for calculating the maximum resonance for Blasuis boundary layers. We also wish to thank the technical staff at DLR for the assistance during the experiments. This work has been supported by TFR (Swedish Research Council for Engineering Sciences).

References

ANDERSSON, P., BERGGREN, M. & HENNINGSON, D. 1997. Optimal disturbances in boundary layers. In *Progress in Systems Control*. Birkhäuser.

BERLIN, S., LUNDBLADH, A. & HENNINGSON, D. S. 1994. Spatial simulations of oblique transition. *Phys. Fluids.* **6**, 1949–1951.

BERTOLOTTI, F. P., HERBERT, T. & SPALART, P. R. 1992. Linear and nonlinear stability of the Blasius boundary layer. *J. Fluid Mech.* **242**, 441–474.

BUTLER, K. M. & FARRELL, B. F. 1992. Three-dimensional optimal perturbations in viscous shear flow. *Phys. Fluids A.* **4**, 1637–1650.

CHANG, C.-L. & MALIK, M. R. 1992. Oblique-mode breakdown and secondary instability in a supersonic boundary layers using nonlinear pse. In *Instability, Transition and Turbulence* (HUSSAINI, M. Y., KUMAR, A. & STREETT, C. L., editors), pp. 231–241. Springer-Verlag.

CHANG, C.-L. & MALIK, M. R. 1994. Oblique-mode breakdown and secondary instability in supersonic boundary layers. *J. Fluid Mech.* **273**, 323–360.

CORKE, T. C. & MANGANO, R. A. 1989. Resonant growth of three-dimensional modes in transitional Blasius boundary layers. *J. Fluid Mech.* **209**, 93 – 150.

ELLINGSEN, T. & PALM, E. 1975. Stability of linear flow. *Phys. Fluids.* **18**, 487–488.

ELOFSSON, P. A. & ALFREDSSON, P. H. 1995. Experiments on nonlinear interaction between oblique Tollmien-Schlichting waves. In *Laminar-Turbulent Transition*, pp. 465–472.

ELOFSSON, P. A. & ALFREDSSON, P. H. 1997. An experimental investigation of oblique transition in a Blasius boundary layer. In *EUROMECH Colloquium 359*.

ELOFSSON, P. A. & LUNDBLADH, A. 1994. Ribbon induced oblique transition in plane poiseulle flow. In *Bypass transition - proceedings from a mini-workshop* (HENNINGSON, D. S., editor), pp. 29–41. TRITA-MEK Technical Report 1994:14, Royal Institute of Technology, Stockholm, Sweden.

FASEL, H. & KONZELMANN, U. 1990. Non-parallel stability of a flat-plate boundary layer using the complete navier-stokes equations. *J. Fluid Mech.* **221**, 311–347.

FASEL, H. & THUMM, A. 1991. Direct numerical simulation of three-dimensional breakdown in supersonic boundary layer transition. *Bull. Am. Phys. Soc.* **36**, 2701.

FASEL, H., THUMM, A. & BESTEK, H. 1993. Direct numerical simulation of transition in supersonic boundary layers: Oblique breakdown. In *Transitional and turbulent compressible flows* (KRAL, L. & ZANG, T., editors), pp. 77–92.

GUSTAVSSON, L. H. 1991. Energy growth of three-dimensional disturbances in plane Poiseuille flow. *J. Fluid Mech.* **224**, 241–260.

Hanifi, A., Schmid, P. J. & Henningson, D. S. 1996. Transient growth in compressible boundary layer flow. *Phys. Fluids.* **8**, 51–65.

Henningson, D. S. 1996. Comment on "Transition in shear flows. Nonlinear normality versus non-normal linearity" [phys. fluids 7 3060 (1995)]. *Phys. Fluids.* **8**, 2257–2258.

Herbert, T. 1983. Secondary instability of plane channel flow to subharmonic three-dimensional disturbances. *Phys. Fluids.* **26**, 871–874.

Herbert, T. 1983. Subharmonic three-dimensional disturbances in unstable shear flows.

Herbert, T. 1988. Secondary instability of boundary layers. *Ann. Rev. Fluid Mech.* **20**, 487–526.

Joseph, D. D. 1976. *Stability of Fluid Motions I.* Springer.

Joslin, R. D., Streett, C. L. & Chang, C. L. 1992. Oblique wave breakdown in an incompressible boundary layer computed by spatial dns and pse theory. In *Instability, Transition and Turbulence* (Hussaini, M. Y., Kumar, A. & Streett, C. L., editors), pp. 304–310. Springer-Verlag.

Joslin, R. D., Streett, C. L. & Chang, C. L. 1993. Spatial direct numerical simulations of boundary-layer transition mechanisms: Validation of PSE theory. *Theoret. Comput. Fluid Dyn.* **4**, 271–288.

Kachanov, Y. S. 1994. Physical mechanisms of laminar-boundary-layer transition. *Ann. Rev. Fluid Mech.* **26**, 411–482.

Kachanov, Y. S., Kozlov, V. & Levchenko, V. Y. 1977. Nonlinear development of a wave in a boundary layer. *Izv. Akad. Nauk SSSR, Mekh. Zhidk. Gaza.* **3**, 49–53. (in Russian).

Kelvin, L. 1887. Stability of fluid motion - rectilinear motion of a viscous fluid between two parallel planes. *Philosophical Magazine.* **24**, 188–196.

Kendall, J. M., 1985. Experimental study of disturbances produced in a pre-transitional laminar boundary layer by weak freestream turbulence. AIAA Paper 85-1695.

Kim, J., Moin, P. & Moser, R. 1987. Turbulence statistics in fully developed channel flow. *J. Fluid Mech.* **177**, 133–166.

Klebanoff, P. S. 1971. Effect of freestream turbulence on the laminar boundary layer. *Bull. Am. Phys. Soc.* **10**, 1323.

Klebanoff, P. S., Tidstrom, K. D. & Sargent, L. M. 1962. The three-dimensional nature of boundary layer instability. *J. Fluid Mech.* **12**, 1–34.

Kleiser, L. & Zang, T. A. 1991. Numerical simulation of transition in wall-bounded shear flows. *Ann. Rev. Fluid Mech.* **23**, 495–537.

Klingmann, B. G. B., Boiko, A., Westin, K., Kozlov, V. & Alfredsson, P. 1993. Experiments on the stability of Tollmien-Schlichting waves. *Eur. J. Mech., B/Fluids.* **12**, 493–514.

Krist, S. E. & Zang, T. A., 1986. Numerical simulation of boundary layers: Part 1. Weak formulation and numerical method. NASA TM 88222.

Landahl, M. T. 1975. Wave breakdown and turbulence. *SIAM J. Appl. Math.* **28**, 735–756.

Laurien, E. & Kleiser, L. 1989. Numerical simulation of boundary-layer transition and transition control. *J. Fluid Mech.* **199**, 403–440.

Lu, Q. & Henningson, D. S. 1990. Subcritical transition in plane Poiseuille flow. *Bull. Am. Phys. Soc.* **35**, 2288.

Luchini, P. 1996. Reynolds number independent instability of the Blasius boundary layer over a flat surface. *J. Fluid Mech.* **327**, 101–115.

Luchini, P. 1997. Reynolds number independent instability of the Blasius boundary layer over a flat surface. part 2: optimal pertubations. Submitted to jfm.

Lundbladh, A., Henningson, D. S. & Johansson, A. V., 1992. An efficient spectral integration method for the solution of the Navier-Stokes equations. FFA-TN 1992-28, Aeronautical Research Institute of Sweden, Bromma.

Lundbladh, A., Schmid, P. J., Berlin, S. & Henningson, D. S., 1994. Simulation of bypass transition in spatially evolving flows. Proceedings of the AGARD Symposium on Application of Direct and Large Eddy Simulation to Transition and Turbulence, AGARD-CP-551.

Malik, M. R., Zang, T. A. & Hussaini, M. Y. 1985. A spectral collocation method for the Navier-Stokes equations. *J. Comp. Phys.* **61**, 64–88.

Morkovin, M. V. 1969. The many faces of transition. In *Viscous Drag Reduction* (Wells, C. S., editor). Plenum Press.

Orr, W. M. F. 1907. The stability or instability of the steady motions of a perfect liquid and of a viscous liquid. Part I: A perfect liquid. Part II: A viscous liquid. *Proc. R. Irish Acad. A.* **27**, 9–138.

Reddy, S. C. & Henningson, D. S. 1993. Energy growth in viscous channel flows. *J. Fluid Mech.* **252**, 209–238.

Reddy, S. C., Schmid, P. J., Bagget, J. S. & Henningson, D. S., 1997. On stability of streamwise streaks and transition thresholds in plane channel flow. submitted to jfm.

Rist, U. & Fasel, H. 1995. Direct numerical simulation of controlled transition in a flat-plate boundary layer. *J. Fluid Mech.* **298**, 211–248.

Rotta, J. C. 1971. Fortran 4-rechenprogramm für grenzschichten bei kompressiblen ebenen und achsensymmetrische strömungen. Technical Report DFVLR-FB 71-51, Institute for Theoretical Fluid Mechanics, Göttingen.

Sandham, N. D., Adams, N. A. & Kleiser, L., 1994. Direct simulation of breakdown to turbulence following oblique instability waves in a supersonic boundary layer. First ERCOFTAC workshop on direct and large eddy simulation, Guildford, England, March 28-30.

Schmid, P. J. & Henningson, D. S. 1992. Channel flow transition induced by a pair of oblique waves. In *Instability, Transition and Turbulence* (Hussaini, M. Y., Kumar, A. & Streett, C. L., editors), pp. 356–366. Springer-Verlag.

Schmid, P. J., Reddy, S. C. & Henningson, D. S. 1996. Transition thresholds in boundary layer and channel flow. In *Advances in Turbulence VI* (Gavrilakis, S., Machiels, L. & Monkewitz, P. A., editors), pp. 381–384. Kluwer Academic Publishers.

Trefethen, L. N. 1997. Psuedospectra of linear operators. *SIAM Review.* **39**, 383–406.

Trefethen, L. N., Trefethen, A. E., Reddy, S. C. & Driscoll, T. A. 1993. Hydrodynamic stability without eigenvalues. *Science.* **261**, 578–584.

Wiegel, M. 1997. *Experimentelle Untersuchung von kontrolliert angeregten dreidimensionalen Wellen in einer Blasius-Grenzschicht.*, volume 312 of *VDI Fortschritt-Bericht Reihe 7.* VDI-Verlag, Düsseldorf (Germany). Dissertation zum Dr.-Ing. an der TH Hannover, Dezember 1996.

Williams, D. R., Fasel, H. & Hama, F. R. 1984. Experimental determination of the three-dimensional vorticity field in the boundary-layer transition process. *J. Fluid Mech.* **149**, 179–203.

Zang, T. A. & Krist, S. E. 1989. Numerical experiments on stability and transition in plane channel flow. *Theoret. Comput. Fluid Dyn.* **1**, 41–64.

Paper 4

P4

A NEW NONLINEAR MECHANISM FOR RECEPTIVITY OF FREE-STREAM DISTURBANCES

S. Berlin
Dept. of Mech., KTH, S-10044 Stockholm, Sweden

D. S. Henningson
FFA, Box 11021, S-16111 Bromma, Sweden

Abstract. Numerical experiments on the interaction of simple vortical free-stream disturbances with a laminar boundary layer are presented. Both spatial and temporal direct numerical simulations (DNS) have been performed for three types of free-stream disturbances. A linear and a new nonlinear receptivity mechanism were identified. The nonlinear mechanism was found to force streaks inside the boundary layer similar to those found in experiments on free-stream turbulence and it performed equally well for disturbances elongated in the streamwise direction as for and oblique free-stream disturbances. The boundary layer response caused by the nonlinear mechanism was, depending on the initial disturbance energy, comparable to that of the linear mechanism, which was only efficient for free-stream streamwise vortices. The receptivity to two-dimensional disturbances was very low for both mechanisms. A parameter study revealed that the wall normal velocity component of the free-stream disturbances is more important for the investigated receptivity mechanisms than the streamwise component. The new boundary layer receptivity mechanism, in which three-dimensional disturbances in the free-stream continuously force streaks inside the boundary layer, may explain discrepancies between experimental results and previously suggested theories for the origin of streaks in boundary layers subjected to free-stream turbulence.

1. Introduction

1.1. Transition scenarios.

1.1.1. *TS-wave breakdown.* The main research efforts on boundary layer transition has traditionally concerned how a disturbance present in the boundary layer may grow or cause transition to turbulence. The Orr-Sommerfeld and Squire equations has been derived and analyzed and the first solutions for two-dimensional eigenfunctions were obtained by Tollmien 1929 and Schlichting 1933. After these Tollmien-Schlichting waves or TS-waves had been observed in experiments, research focused on how they and their subsequent secondary instabilities cause transition. Reviews on this subject can be found by for example Herbert 1988, Kachanov 1994 and Kleiser & Zang 1991. Terms like “TS-wave” or “TS-frequency” are however often used for disturbances that may be neither two-dimensional nor have a TS-like wall normal distribution. It is not clear that such disturbances cause transition by the same mechanism as the original TS-waves. That transition may be caused by other mechanisms is evident and Morkovin 1969 called these mechanisms, that at the time were unknown, bypass-transition.

1.1.2. *Non-modal breakdown.* Reexamination of the Orr-Sommerfeld and Squire equations (Gustavsson 1991, Butler & Farell 1992, Reddy & Henningson 1993 and Trefethen *et al.* 1993) has led to the finding that the eigenfunctions are non-orthogonal, which means that disturbances other than exponentially unstable eigenfunctions can grow in the boundary layer. The physical mechanism behind this linear mechanism is streamwise vortices that interact with the boundary layer shear and create streaks in the streamwise velocity component (lift-up). Reddy *et al.* 1997 has shown that the modification of the mean flow by the streaks may cause secondary instabilities in a similar manner to those caused by TS-waves.

Another transition scenario that is also based on these non-modal mechanisms, in combination with nonlinear mechanisms, is oblique transition. It is initiated by two oblique waves at equal and opposite angles and does not need a TS-wave to cause transition nor does it necessarily generate a TS-wave during the transition process. It was first investigated numerically by Schmid & Henningson 1992 in plane Poiseuille flow and can be exited even at subcritical Reynolds numbers. It has since been investigated also in laminar boundary layers both experimentally and numerically (Berlin, Lundbladh & Henningson 1994, Wiegel 1997, Elofsson 1997 and Berlin, Wiegel & Henningson 1998) and an important ingredient is found to be the growth of streamwise streaks.

1.2. Receptivity mechanisms.

1.2.1. *TS-wave receptivity.* To understand and predict transition, knowledge about the manner in which disturbances can enter or interact with the boundary layer is necessary. Receptivity researchers has therefore investigated how TS-waves can be generated in the boundary layer by outer disturbances. The disturbances are often characterized as either acoustic or vortical disturbances convected by the free-stream. Both types of disturbances has been thoroughly investigated by asymptotic methods and a summary of the results can be found in the reviews by Goldstein & Hultgren 1989 and Kerschen 1990. They find that to overcome the difference in length scale between acoustic disturbances and unstable TS-waves, local length scales of the order of TS-waves are needed. Receptivity for acoustic disturbances can therefore be found in the leading edge region, by rapid geometry changes or local roughness. Kerschen 1985 finds the receptivity for convected gusts (vortical disturbances), interacting with short scale mean flow gradients created by for example a local surface hump or in the vicinity of the leading edge, to be comparable to that of acoustic disturbances. The experimental findings on TS-wave receptivity has been reviewed by Nishioka & Morkovin 1986 and generally agree with the theoretical investigations. The effect of free-stream sound has also been investigated numerically by Lin, Reed & Saric 1992. They found receptivity at the nose of their elliptical leading edge and that a sharper leading edge gave less receptivity. The sudden pressure gradients appearing at the junction of their leading edge and the flat plate was found to be an important receptivity source. Buter & Reed 1994 investigated the effect of vortical disturbances at the leading edge numerically and found the same sources of receptivity as Lin, Reed & Saric 1992.

1.2.2. *Experiments with free-stream turbulence.* Experiments of boundary layers subjected to free-stream turbulence are characterized by disturbances very different from TS-waves, namely streamwise elongated streaks. These were first observed as low-frequency oscillations in hot-wire signals caused by slow spanwise oscillations of the streaks. They are commonly referred to as Klebanoff-modes after Klebanoff's 1971 mainly unpublished experimental findings (Kendall 1985). After comparing data from several experiments Westin 1994 *et al.* drew the conclusion that there is no general correlation between the level of free-stream turbulence, the fluctuation level in the boundary layer and the transitional Reynolds number. They compared results for the streamwise velocity component, which is what is normally reported from the experimental investigations. Yang & Voke's 1993 numerical experiment however, indicated that the wall normal velocity component of the free-stream turbulence is more important for the response in the boundary layer. Kendall 1990 states that in experiments with week free-stream turbulence, the streak response scaled linearly with the turbulence level in the streamwise velocity component and that Klebanoff found the spanwise scale of the streaks to correlate with the free-stream turbulence scales. Westin 1994 *et al.* found that the transition point moved substantially when the stagnation point on their leading edge was altered. If that was due to changes of the streak growth or caused by increased receptivity to other disturbances was not reported.

1.2.3. *Theory and computations of free-stream turbulence.* Choudhari 1996 used asymptotic methods to study the receptivity of oblique disturbances and found the receptivity by the leading edge and local humps to increase with increased obliqueness of the vortical disturbances. He also noted that the wall normal distribution of the response to the oblique disturbances was similar to the Klebanoff mode. Bertolotti 1997 assumes free-stream modes, periodic in all directions, of which he calculates the boundary layer receptivity in a "linear region" excluding the the leading edge. He finds receptivity to modes with zero streamwise wavenumber. These modes are used as forcing in PSE calculations of the downstream disturbance development and the results agree fairly well with experimental results. Bertolotti 1997 finds it most likely that the growth of streaks is related to non-modal growth.

Traditionally the non-modal theory has been developed from a temporal point of view but Luchini 1996 studied the same type of growth in space, which is more appropriate for a spatially developing boundary layer. He finds a "Reynolds number independent instability" causing the growth of streamwise streaks. It is vortical disturbances at the leading edge that create disturbance growth in the streamwise velocity component. Andersson, Berggren & Henningson 1998 and Luchini 1997 used an optimization technique to determine what disturbance present at the leading edge will give the largest disturbance in the boundary layer. They also found streamwise vortices causing growth of streaks. Note that the disturbances present at the leading edge were outside the boundary layer and the calculated response inside the boundary layer, i.e. a receptivity process. The results of the calculations on spatially growing streaks well predict a number of the features seen in experiments. There are, however, some discrepancies concerning the growth rate and the slightly increasing spanwise scale of the streaks as they develop downstream.

The importance of TS-waves for transition caused by free-stream turbulence, is not clear. Generally fluctuations with a frequency close to the most unstable TS-waves are found at the boundary layer edge and have a mode shape different from the unstable eigenmode. At high turbulence levels TS-waves are difficult to identify and do not cause transition 1992. For low free-stream turbulence levels Kendall 1990 can identify wave packets traveling with the same phase speed as TS-waves with amplitudes scaling nonlinearly with the turbulence level. Boiko *et al.* 1994 introduced additional TS-waves in an experiment with a boundary layer subjected to free-stream turbulence and found their amplification rate to be smaller than in the undisturbed boundary layer. Bertolotti 1997 concludes that a mechanism for TS-wave generation by free-stream turbulence is still unknown.

In our numerical experiments, we exclude the leading edge and study how simple vortical free-stream disturbances interact with a laminar boundary layer. The goal is to investigate if there is a mechanism for receptivity that does not include the leading edge. Such a mechanism would continuously force disturbances in the boundary layer and could provide an explanation to the present discrepancies between calculations and experiments on free-stream turbulence. One simple free-stream disturbance type that will get much attention consists of two oblique free-stream waves. Oblique waves inside the boundary layer has, as previously stated, been found to generate streaks in the boundary layer and it is therefore interesting to observe if they can do the same when present in the free-stream. We first present (§2) the two numerical formulations used in the investigation and the parameters defining the shape of the introduced free-stream disturbances. In §3 results from spatial simulations is presented and in §4 we start with a comparison between these results and the results of temporal calculations. We continue by identifying both a nonlinear and linear mechanism that cause growth of streamwise streaks in the boundary layer. Finally a study of how the receptivity depends on the characteristics of our free-stream disturbances is presented. We also relate our numerical results to the optimal disturbances calculated by linear theory.

2. Numerical method

The simulation code (see Lundbladh, Henningson & Johansson 1992 and Lundbladh *et al.* 1994) used for the present computations uses spectral methods to solve the three-dimensional, time dependent, incompressible Navier-Stokes equations. The algorithm is similar to that of Kim, Moin & Moser 1987, i.e. Fourier representation in the streamwise and spanwise directions and Chebyshev polynomials in the wall-normal direction and pseudo-spectral treatment of the nonlinear terms. The time advancement used was a four-step low storage third-order Runge-Kutta method for the nonlinear terms and a second-order Crank-Nicholson method for the linear terms. Aliasing errors from the evaluation of the nonlinear terms were removed by the $\frac{3}{2}$-rule when the horizontal

FFTs were calculated. In order to set the free-stream boundary condition closer to the wall, a generalization of the boundary condition used by Malik, Zang & Hussaini 1985 was implemented. It is an asymptotic condition applied in Fourier space with different coefficients for each wavenumber that exactly represents a potential flow solution decaying away from the wall. This method, that does not include the leading edge, has been implemented in a spatial and a temporal formulation.

2.1. Temporal method. The basis of the temporal simulation technique is the thought of a localized disturbance or wave traveling downstream, surrounded by a boundary layer of constant thickness which grows slowly in time. The extent of the computational domain is small as only one wave length of the largest disturbance is included in the streamwise and spanwise directions. Moreover, the approximation that the boundary layer thickness is constant at each instant of time is made, which enables us to use periodic boundary conditions in the wall parallel directions. This approximation necessitates a correction to the equations. Let us define the streamwise, wall normal and spanwise directions as x, y and z respectively with velocity disturbance components u, v and w that are all made dimensionless with the displacement thickness δ_0^* at $t = 0$ and the free-stream velocity U_∞. With velocity disturbance we mean that the base flow (Blasius) has been subtracted from the total flow. We follow the ideas of Spalart & Yang 1987 and introduce a reference point $x_r = x_0 + ct$ where c is a reference speed. We now assume that the undisturbed boundary layer in the vicinity of the disturbance has the velocity distribution $U(y,t) = U(x_r, y)$, $V(y,t) = 0$ (no x dependence). Whereas the full Blasius velocity $U(x,y)$ (with the corresponding V given by continuity) is a good approximate solution to the Navier-Stokes equations, that is not true for $\{U(y,t), V(y,t)\}$. Thus to ensure the correct development of the boundary layer profile over extended periods of time a (weak) forcing is added to the streamwise momentum equation,

$$
\begin{aligned}
F_x &= \frac{\partial U(y,t)}{\partial t} - \frac{1}{R}\frac{\partial^2 U(y,t)}{\partial y^2} \\
&= c\frac{\partial U(x,y)}{\partial x} - \frac{1}{R}\frac{\partial^2 U(x,y)}{\partial y^2} \qquad (1)
\end{aligned}
$$

where the right hand side should be evaluated at the reference coordinate x_r. The reference speed c should be chosen as the propagation speed of the studied disturbance for best agreement with a spatially developing flow, a difficulty if disturbances present in the computational domain travel at very different speeds.

The disturbance that we intend to study is added as an initial condition to the flow field from which we start the simulation. We want to control its size and wall normal position and it should fulfill continuity. The velocity components of the chosen disturbance are,

$$u = -A\alpha \sin(\alpha x)\cos(\beta z) f'(y)/k^2 \tag{2}$$
$$v = A\cos(\alpha x)\cos(\beta z) f(y) \tag{3}$$
$$w = -A\beta \cos(\alpha x)\sin(\beta z) f'(y)/k^2, \tag{4}$$

where α and β are the streamwise and spanwise wavenumbers and

$$k^2 = \alpha^2 + \beta^2 \tag{5}$$
$$f(y) = S\left(\frac{y-l}{\lambda}\right) - S\left(\frac{y-(l+2\lambda)}{\lambda} + 1\right). \tag{6}$$

$S(x)$ is a smooth step function rising from zero for negative x to one for $x \geq 1$. We have used the following form for S, which has the advantage of having continuous derivatives of all orders,

$$S(x) = \begin{cases} 0 & x \leq 0 \\ 1/[1+\exp(\frac{1}{x-1}+\frac{1}{x})] & 0 < x < 1 \\ 1 & x \geq 1 \end{cases}$$

Selecting $\alpha \neq 0$ and $\beta \neq 0$, two oblique waves with equal and opposite angels will be initiated, and $\beta = 0$ or $\alpha = 0$ gives a two-dimensional wave or streamwise vortices, respectively. The parameters l and λ gives the wall normal distance to the lowest point with non-zero amplitude and the disturbance half width, respectively. $f(y)$ is illustrated with $l = 5$ and $\lambda = 2$ in figure 1.

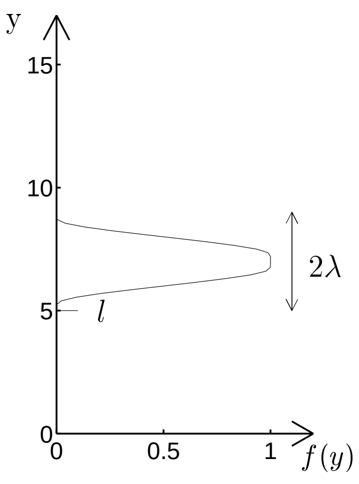

FIGURE 1. Illustration of wall normal amplitude function $f(y)$ for the parameters $l = 5$ and $\lambda = 2$

All temporal simulations has been performed for an initial Reynolds number $R = \nu\delta_0^*/U_\infty = 400$ and $16 \times 97 \times 16$ spectral modes has been used in the x, y

and z directions, respectively, which was sufficient as the disturbance amplitudes were low. The box hight was 15 initial displacement thicknesses (δ_0^*), except for a few cases when the disturbances were moved very far into the free-stream and the hight was increased to 20 displacement thicknesses. The streamwise and spanwise box sizes were adjusted to fit one fundamental wavelength in each simulation.

2.2. Spatial method. In an experimental investigation disturbances develop downstream in a slowly thickening boundary layer and the best numerical model of this is a spatial formulation. At each time instant the simulation then contains the complete flow field of the streamwise region of interest and the boundary layer growth is modeled correctly. To combine this requirement with periodic boundary condition in the streamwise direction a "fringe region", similar to that described by Bertolotti, Herbert & Spalart 1992 has been implemented. In this region, at the downstream end of the computational box, the function $\lambda(x)$ in equation (7) is smoothly raised from zero and the flow is forced to a desired solution $\mathbf{v}$ in the following manner,

$$\frac{\partial \mathbf{u}}{\partial t} = NS(\mathbf{u}) + \lambda(x)(\mathbf{v} - \mathbf{u}) + \mathbf{g} \tag{7}$$

$$\nabla \cdot \mathbf{u} = 0 \tag{8}$$

where $\mathbf{u}$ is the solution vector and $NS(\mathbf{u})$ the right hand side of the (unforced) momentum equations. Both $\mathbf{g}$, which is a disturbance forcing, and $\mathbf{v}$ may depend on the three spatial coordinates and time. $\mathbf{v}$ is smoothly changed from the laminar boundary layer profile at the beginning of the fringe region to the prescribed inflow velocity vector, which in our case is a Blasius boundary layer flow. This method damps disturbances flowing out of the physical region and smoothly transforms the flow to the desired inflow state, with a minimal upstream influence.

In the spatial formulation we continuously generate disturbances in the upstream region of the computational domain. This is done by applying a body force in the flow. The force distribution of the initiated disturbance was taken from equations (2)-(4), but u, v and w was exchanged for the force g_x, g_y and g_z of equation (7). In addition the streamwise wavenumber α in equations (2)-(5) was exchanged for a frequency ω and the S-function was used to confine the forcing also in the streamwise direction. It was limited to the region $10 < x < 26$.

The Reynolds number at the inflow of the spatial simulations was also $R = 400$ and in the larger simulation presented first, the box had the non-dimensional size $600 \times 20 \times 17.95$ in the streamwise, wall normal and spanwise directions, respectively. That was well resolved with $300 \times 97 \times 32$ spectral modes. For the scaling and parameter studies a smaller box was used with dimensions $300 \times 15 \times 32.79$ and with resolution $128 \times 97 \times 16$, which also was well resolved.

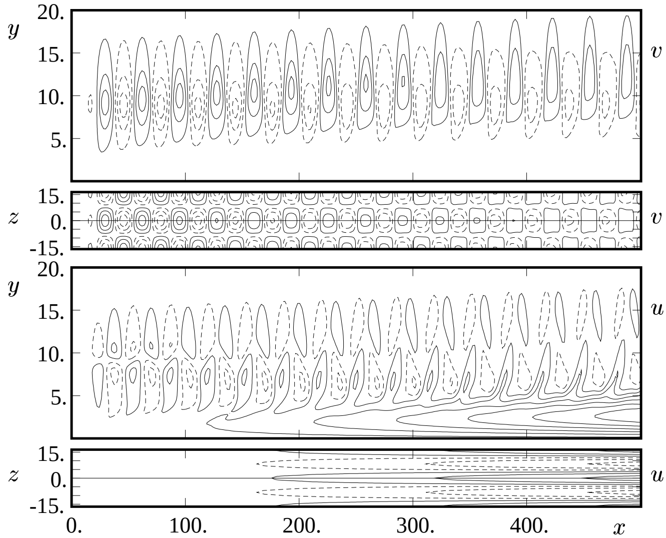

FIGURE 2. Contours of velocity from spatial simulation with oblique waves in the free-stream. Top: v at $z = 0$, spacing 0.005, Second: v at $y = 9$, spacing 0.005, Third: u at $z = 0$, spacing 0.0075, Bottom: u at $y = 2$, spacing 0.025.

3. Spatial results

The presentation of results is divided into two sections according to the numerical method used to produce the results. In this section we present the spatial simulations that model the real physics closer. The purpose is to show that the qualitative features of the new mechanism are the same as those identified by the temporal formulation (section 4), used in the subsequent parameter studies.

3.1. Generation of streamwise streaks. In a first spatial simulation, two oblique waves were forced with $\omega = 0.1916$, $\beta = 0.1916$, $l = 7$ and $\lambda = 2$. The downstream development is shown in figure 2. The two top figures contains contours of the wall normal disturbance velocity v in planes perpendicular and parallel to the wall. With disturbance velocity we mean that a Blasius flow has been subtracted from the complete velocity field. The second frame from the top contains a wall parallel plane selected at $y = 9.0$. It shows the typical chequered disturbance pattern produced by two oblique waves and that the wave amplitude decreases downstream. The downstream decay is also seen in the perpendicular symmetry plane $z = 0$, from which it is clear that the main part of the oblique disturbances remain in the free-stream. Contours of the streamwise disturbance velocity u is displayed in the two bottom frames of figure 2. The perpendicular plane is $z = 0$ and we can again see the downstream decay in the free-stream, but also disturbance growth inside the boundary layer. A wall parallel plane inside the boundary layer at $y = 2$ reveals growing streamwise streaks with half

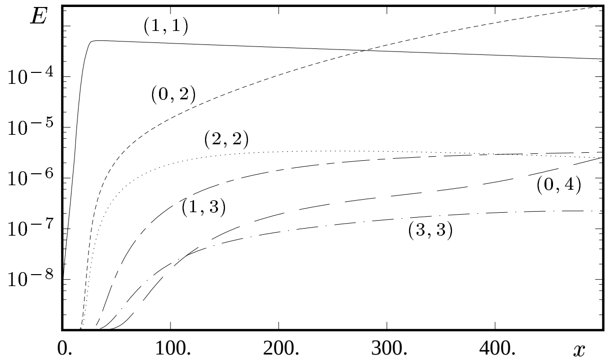

FIGURE 3. Downstream development of the energy in selected Fourier modes. The $(1, 1)$ is forced in the free-stream between $x = 10$ and $x = 26$, it then decays downstream. Strong growth is observed in the vortex/streak mode $(0, 2)$ after the initial quadratic generation that also generates $(2, 2)$.

the spanwise wavelength of the initially generated oblique waves. These streaks are forced through a nonlinear mechanism and their growth is due to linear non-modal mechanisms. In order to show this we will Fourier transform the velocity field in time and in the spanwise direction.

3.2. Results in Fourier space. In Fourier space we normalize the frequency and spanwise wavenumber of the disturbances with the fundamental frequency and spanwise wavenumber of the generated oblique waves ($\omega_0 = 0.1916$, $\beta_0 = 0.1916$). The oblique waves are then denoted as the $(1, \pm 1)$ modes and the streamwise streaks becomes the $(0, 2)$ mode, as their frequency is zero and spanwise wavenumber twice that of the oblique waves. The nonlinear interactions will spread energy in Fourier space. With the present generation of symmetric $(1, \pm 1)$ modes however, only modes for which the sum of the normalized frequency and wavenumber add to an even number can be exited. The symmetry will be preserved by the Navier-Stokes equations and consequently all modes (ω, β) will equal the corresponding $(\omega, -\beta)$ modes, and we will therefore only show the modes with positive β. Figure 3 shows the slow downstream decay of the energy in the Fourier mode $(1, 1)$ representing a forced oblique wave. It also shows the nonlinear excitation of some of the modes involved. The growth of the $(0, 2)$ mode is significant and we also observe a beginning growth of the $(0, 4)$ mode. The main energy in these modes reside in the boundary layer. The main energy of the other modes remain in the free-stream. This is demonstrated for the $(1, 1)$ and $(0, 2)$ modes in figure 4, showing contours of the energy distribution in a vertical plane for the two modes.

To investigate the relation between the body force and the response in the dominant modes, we performed four simulation with varying energy input by the body force. In figure 5 the energy in the $(1, 1)$ and $(0, 2)$ modes from these simulations are plotted using two different scalings. In the top figure, each curve

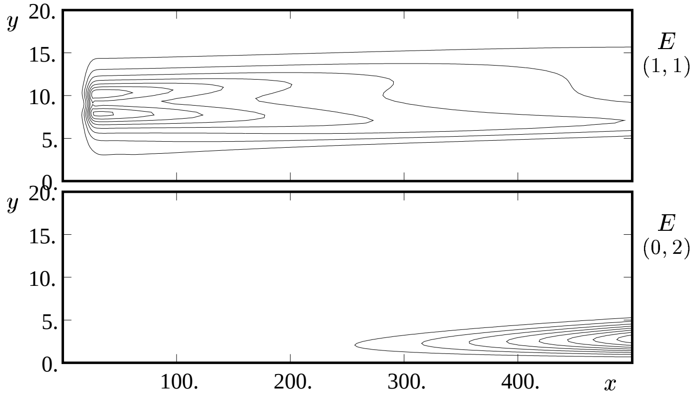

FIGURE 4. Total energy distribution in the wall normal direction (y) as function of x in the $(1, 1)$ mode (top) and $(0, 2)$ mode (bottom). The energy in the oblique wave stays in the free-stream whereas the streak grows inside the boundary layer.

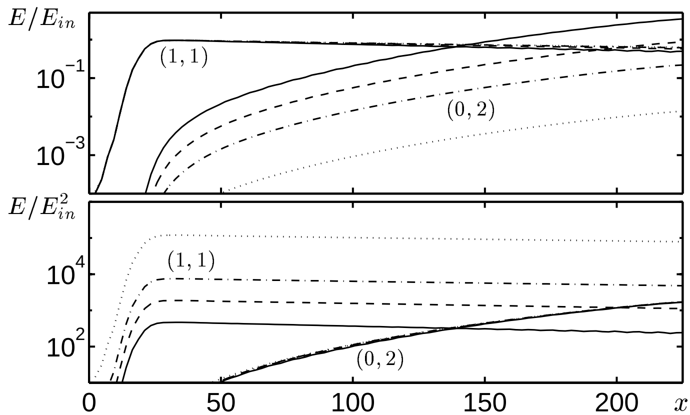

FIGURE 5. Downstream development of the energy in the $(1, 1)$ and $(0, 2)$ mode from four simulations with different initial energy input, E_{in}. The results from each simulation are scaled with E_{in} of that particular simulation (top) and with E_{in}^2 (bottom). The collapse of the $(1, 1)$ modes (top) and the $(0, 2)$ (bottom) demonstrates the linear and quadratic scaling, respectively.

has been scaled with the energy input of the oblique waves for that simulation and in the bottom figure by the same quantity squared. The $(1, 1)$ curves collapse in the top figure, confirming the linear dependence on the excitation of body force. In the bottom figure the $(0, 2)$ curves collapse, demonstrating that the streaks depend quadratically on the forcing and has been generated nonlinearly.

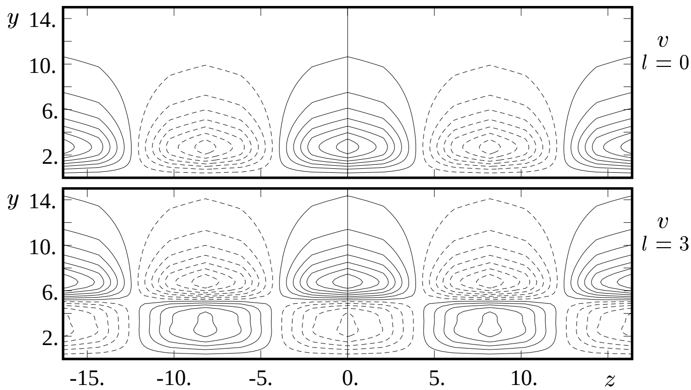

FIGURE 6. Contours of the time averaged wall normal disturbance velocity of the streamwise vortices in the $(0, 2)$ mode. When the initial disturbance $(1, 1)$ was forced in the boundary layer one layer of $(0, 2)$ vortices were generated (top). When the forcing was moved to the free-stream ($l = 3$) two layers of vortices were generated (bottom).

3.3. Two nonlinear modes. The nonlinear generation of streamwise vortices inside the boundary layer by oblique waves is active regardless of the distance from the wall to the point were the oblique waves are generated. Naturally it is most efficient when the oblique waves are forced close to the wall ($l = 0$). As the forcing of the oblique waves is moved away from the wall a maxima in the boundary layer response can be found for a specific wall normal distance of the forcing. We will discuss this further in §4.3 together with the temporal parameter study. We restrict the presentation of the spatial results to show that the nonlinear mechanism can excite two different vortex modes, depending on the wall normal distance of the initial disturbance. In figure 6 contours of the time averaged normal velocity disturbance $\bar{v}$ for these different modes are plotted in a plane perpendicular to the flow. The top figure displays the mode exited when the forcing is applied close to the wall. This disturbance mode consist of streamwise elongated counter rotating vortices. The bottom figure displays the situation when the forcing is applied at an optimal free-stream location, which for the current parameter combination is $l = 3$. This disturbance consist of two layers of counter rotating vortices on top of each other. We observe that the maximum of the lower disturbance layer is positioned at the same wall normal distance as the maximum of the disturbances in the top figure. The mode with two layers of counter rotating vortices remains when the forcing is moved further away from the wall. At intermediate forcing positions these two modes are counter acting each other and the boundary layer response to the oblique waves is decreased. Note that the outer vortices are well outside the boundary layer, and would be hidden in free-stream turbulence.

4. Temporal Results

4.1. Comparison with spatial results.

4.1.1. *General consideration.* Direct comparison of temporal and spatial results is difficult for several reasons. In the temporal formulation the velocity field itself is specified as an initial condition, an approach that could have been used also in the spatial case but the disturbance would then be convected out of the considered domain. We instead chose to continuously force the disturbance in the upstream part of the computational domain. As the same algebraic expression is used to specify both the force distribution in the spatial formulation and the amplitude of the initial condition we cannot expect to obtain identical velocity disturbances. A further complication is that in the spatial case we generate a frequency and the streamwise wavelength is then given by the phase speed of the disturbance, which differs depending on the wall normal position of forcing. In the temporal formulation we specify the streamwise wavenumber itself. However, the temporal formulation has been widely used and it also models the basic physical mechanism of interest here, which we intend to show in this subsection. For this we have used the same parameter settings as in the spatial simulations with $\beta_0 = 0.1916$, $\lambda = 2$ and $\omega_0 = 0.1916$ exchanged for $\alpha_0 = 0.1916$, implying a phase speed of 1 as in the free-stream.

4.1.2. *Scaling and nonlinear modes.* We will start by demonstrating the linear and quadratic scaling of the $(1, \pm 1)$ and $(0, 2)$ modes respectively. Observe that we now are discussing streamwise wavenumbers instead of frequency and $(1, -1)$ means that $\alpha = 1 \cdot \alpha_0$ and $\beta = -1 \cdot \beta_0$. Figure 7 shows the energy in the $(1, 1)$ and $(0, 2)$ modes from four simulations where the initial energy had four different values. The same two scalings as in figure 5 was used for the two frames. In the top frame, each curve has been scaled with the energy input of a oblique wave for that simulation and in the bottom figure by the same squared. Again the linear scaling of the oblique waves $(1, 1)$ and the quadratic generation of the streaks $(0, 2)$ is evident. The $(1, 1)$ and $(0, 2)$ curves collapse in the top and bottom frame respectively. The logarithmic scale on the vertical axis has been chosen to match that of figure 5, but the horizontal scale is now time instead of downstream distance. The low cost of temporal simulations let us follow the disturbance development much longer and we observe the decay of the streaks after $t = 1400$. The spatial simulation only covered a time corresponding to $t = 225$ for a disturbance traveling with the free-stream.

Recall that two different nonlinearly excited vortex modes were observed in the spatial simulations, depending on the wall normal distance of the disturbance. These two modes were also identified using the temporal formulation and they are displayed in figure 8 for the same parameter settings that was used for the spatial case. In that case we presented a time average of the v component collected during one fundamental period. This was to extract the streak mode that have zero frequency. For the temporal case we have selected the zero streamwise wavenumber part of the v component to present a corresponding quantity. The temporal and spatial modes are very close considering the differences in disturbance generation and calculation method.

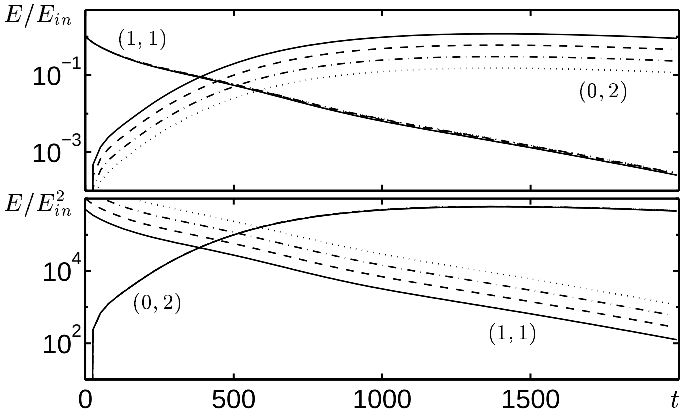

FIGURE 7. Time development of the energy in the $(1,1)$ and $(0,2)$ mode from four simulations with different initial energy input, E_{in}. The results from each simulation are scaled with E_{in} of that particular simulation (top) and with E_{in}^2 (bottom). The collapse of the $(1,1)$ modes (top) and the $(0,2)$ (bottom) demonstrates the linear and quadratic scaling respectively.

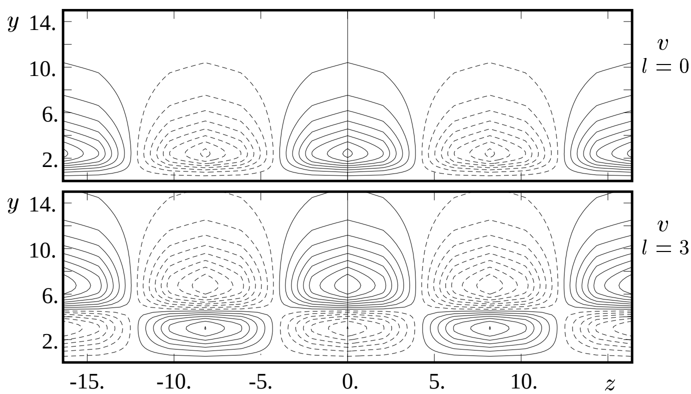

FIGURE 8. Contours of the v component of the streamwise vortices in the $(0,2)$ mode. When the initial disturbance $(1,1)$ was forced in the boundary layer one layer of $(0,2)$ vortices were generated (top). When the forcing was moved to the free-stream ($l=3$) two layers of vortices were generated (bottom).

4.1.3. *Effects of boundary layer growth.* In the presentation of the numerical method we mentioned that it is possible to specify a temporal growth of the boundary layer thickness by the reference speed c. Correct reference speed for disturbances convected by the free-stream is obviously $c = 1$. For disturbances in the boundary layer an other value may be better suited. The phase speed of zero frequency disturbances nonlinearly forced form the free-stream is difficult to determine. Figure 9 present results from two simulations where $c = 1$ and $c = 0$ was used to produce the results plotted with solid and dashed lines, respectively.

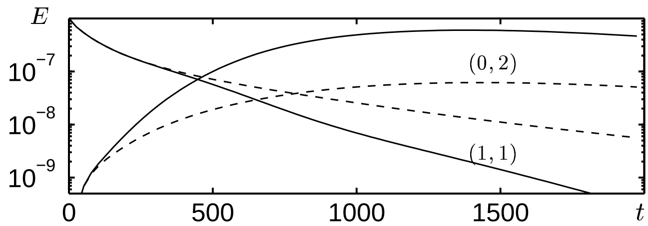

FIGURE 9. Time development of the $(1, 1)$ and $(0, 2)$ mode for two simulations with $c = 1$ (solid) and $c = 0$ (dashed).

The initial disturbance was generated in the free-stream with $\lambda = 5$ and the other parameters were the same as previously used in this subsection. The decay of the oblique waves is found to be faster in the growing boundary layer, whereas the response in the streaks are larger. We will use the convection speed for free-stream disturbances in this paper if nothing else is stated. Many of the results have actually been calculated for both $c = 1$ and $c = 0$ and we have found the parameter dependence to be qualitatively similar. The streaks usually has a lower amplitude and their maximum occurs slightly later for the boundary layer with constant thickness.

4.2. Receptivity mechanisms. The oblique waves in the free-stream generate growing streamwise streaks in the boundary layer by a nonlinear process in both the spatial and the temporal numerical simulations. We will now study this receptivity mechanism closer and also compare it with two slightly different disturbance types. The first is two-dimensional waves and the second streamwise vortices, both initiated in the free-stream. The parameter settings for the three disturbance types were $l = 5$ and $\lambda = 2$, with streamwise wavenumber $\alpha = 0.1916$ for both oblique and two dimensional waves and spanwise wavenumber $\beta = 0.35$ for oblique waves and streamwise vortices. The study of the streamwise vortices will also lead to a discussion of a linear receptivity mechanism.

4.2.1. *Nonlinear receptivity mechanism.* Better understanding of how the nonlinear mechanism act can be gained by studying the energy in the velocity components as a function of both time and the wall normal coordinate. We will here only consider three types of primary modes $(1, 1)$, $(1, 0)$ and $(0, 1)$ and the main modes they force nonlinearly $(0, 2)$ and $(2, 0)$. We have also separated the parts in each mode that have a linear, quadratic and cubic dependence on the energy in the initial disturbance. The linear and cubic terms will only contribute to the primary modes $(1, 1)$, $(1, 0)$ and $(0, 1)$. The main nonlinearly generated modes $(0, 2)$ and $(2, 0)$ will only contain quadratic terms, since the fourth order terms that they also could contain are negligible at the low amplitudes we have used. To do the separation we first calculate the development of the same disturbance initiated with several different initial amplitudes A_i, $(i = 1, \ldots, n)$. We then assume that the results can be expanded,

$$R_i = c_1 A_i + c_2 A_i^2 + c_3 A_i^3 + \cdots + c_k A_i^k + \cdots . \tag{9}$$

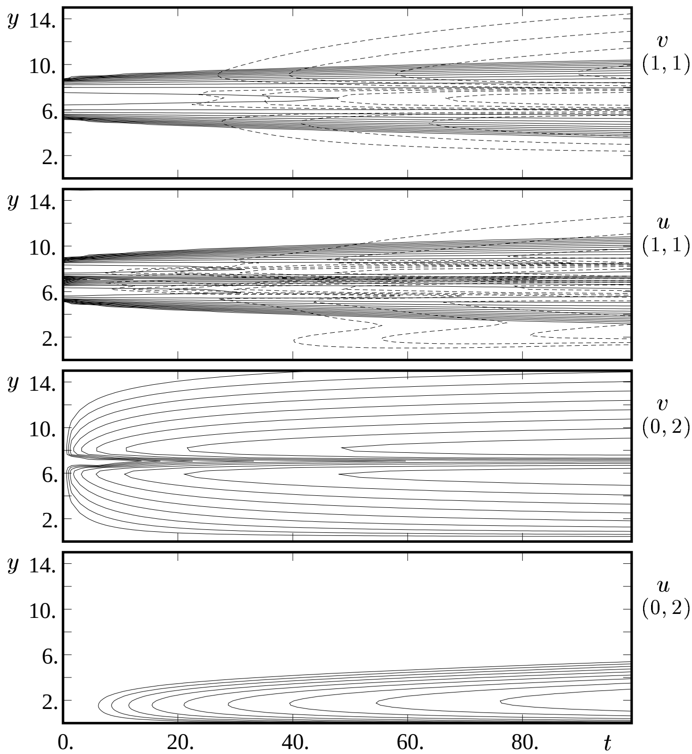

FIGURE 10. Logarithmic contours of energy starting at $1 \cdot 10^{-12}$, where two contours represent an increase with a factor of 10. Top: v in the $(1,1)$ mode. Solid represents the linear part and dashed the cubicly generated part, Second: u in the $(1,1)$ mode. Solid represents the linear part and dashed the cubicly generated part, Third: v in the quadratically generated $(0,2)$ mode, Bottom: u in the quadratically generated $(0,2)$ mode. Note how the $(0,2)$ mode is nonlinearly generated in the hole domain and itself generates growing streaks.

With n different amplitudes A_i we get a system of equations that we can solve for the coefficients c_i, $(i = 1, \dots, n)$ of the form

$$c_i = \gamma_1^i R_1 + \gamma_2^i R_2 + \gamma_3^i R_3 + \cdots + \gamma_n^i R_n, \tag{10}$$

where the γ's are functions of A_i, $(i = 1, \dots, n)$. Note that the result signified by R_i may be a single velocity component a single mode or a complete velocity field. The first and the second frame from the top in figure 10 shows the energy in v and u respectively for an oblique wave, both the linear part (solid contours) and the cubic part (dashed contours). The linear part of the oblique waves, both u and v, diffuses slowly and decays rapidly with time. The cubicly generated part is seen to be more spread out vertically. The most interesting quadratically generated mode is $(0,2)$, and in the second frame from the bottom we display its v component, which is rapidly generated by the non-linearities in a large wall normal domain. It is not damped and only slightly affected by the boundary layer and the wall. The v component is associated with streamwise vortices that

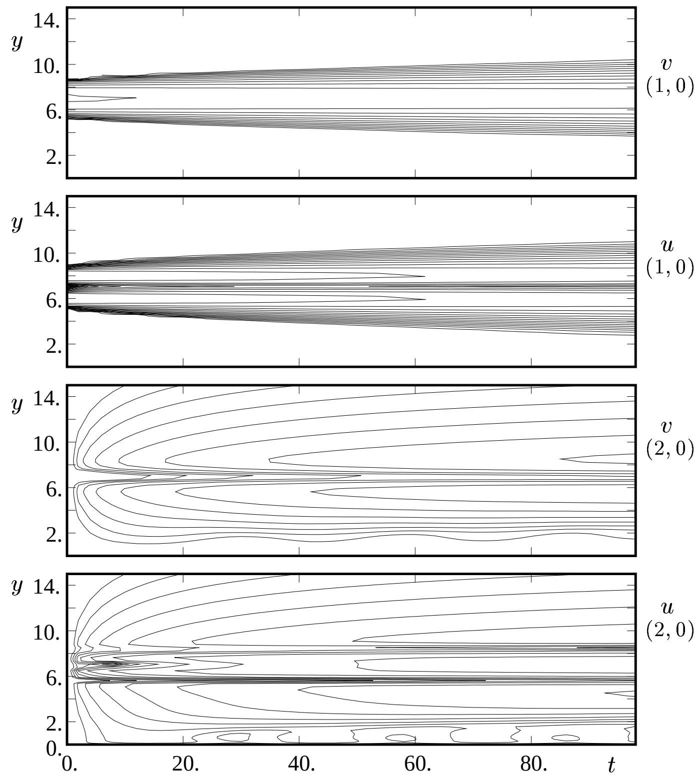

FIGURE 11. Logarithmic contours of energy starting at $1 \cdot 10^{-12}$, where two contours represent an increase with a factor of 10. Top: v in the $(1,0)$ mode. Second: u in the $(1,0)$ mode. Third: v in the quadratically generated $(2,0)$ mode, Bottom: u in the quadratically generated $(2,0)$ mode. Note that the nonlinearly generated $(2,0)$ mode is damped in the boundary layer.

immediately interact with the shear in the boundary layer to form streaks. This is observed as growing energy in the u component inside the boundary layer in the bottom frame.

In figure 11 the spanwise wavenumber of the initial disturbance was set to zero and we are studying a two-dimensional wave. Since it is the $(1,0)$ mode which has been initiated, the nonlinearities cannot generate a streamwise vortex mode, but only a two-dimensional $(2,0)$ mode. Both the v and u components of the linear $(1,0)$ mode displayed in the two top frames diffuses slowly as they decay. The cubicly generated $(1,0)$ is confined to the same wall normal region as the linear part and is therefore not displayed. The energy in both components of the quadratic $(2,0)$ mode is distributed over a larger wall normal domain, which is shown in the two bottom frames. The two-dimensional $(2,0)$ mode, however, is damped by the wall and the boundary layer. Growth is not observed in the boundary layer and the main energy of both velocity components reside in the free-stream.

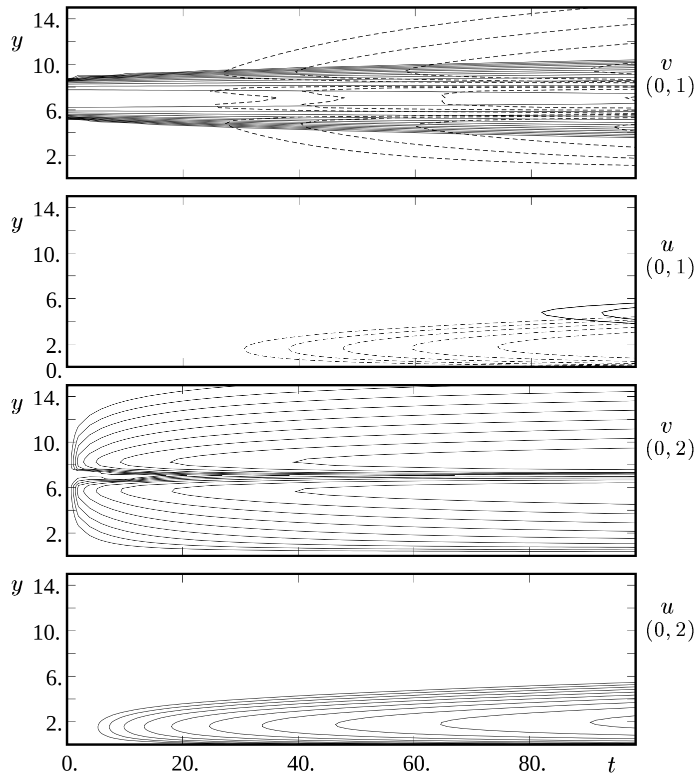

FIGURE 12. Logarithmic contours of energy starting at $1 \cdot 10^{-12}$, where two contours represent an increase with a factor of 10. Top: v in the $(0,1)$ mode. Solid represents the linear part and dashed the cubicly generated part, Second: u in the $(0,1)$ mode. Solid represents the linear part and dashed the cubicly generated part, Third: v in the quadratically generated $(0,2)$ mode, Bottom: u in the quadratically generated $(0,2)$ mode. Note how the $(0,2)$ mode is nonlinearly generated in the hole domain and generates growing streaks. The cubic $(0,1)$ also generates streaks in the same way.

If the streamwise wavenumber is set to zero the initiated disturbance consists of streamwise vortices, the $(0,1)$ mode. We then have three possible mechanisms for interaction of streamwise vortices with the boundary layer shear. The initiated $(0,1)$ vortices may diffuse into the boundary layer, the non-linearity will quadratically generate $(0,2)$ mode vortices, and we may have a cubic generation of $(0,1)$ vortices. In figure 12 the development of the three possibilities are followed during the first 100 time units. The v component of the $(0,1)$ mode is displayed in the top figure. The linear part decays and diffuses in the same way as we noted for the other two disturbance types, whereas the cubic generation has spread energy over a larger wall normal region. The interaction of these two parts of $(0,1)$ with the boundary layer shear results in growing streaks, which are observed in the second frame displaying the u component of $(0,1)$. Energy of cubicly dependent streaks are growing in the boundary layer, but the diffusion of the linear v component has just reached the boundary layer edge and only a small linear u disturbance appears in the upper shear region. The two bottom frames shows the quadraticly generated $(0, 2)$ mode. It is generated over the hole wall normal domain as for the oblique free-stream disturbances and the v component is again essentially unaffected by the boundary layer. Strong streak growth is observed in the streamwise velocity disturbance in the bottom frame.

4.2.2. *Long term comparison and linear mechanism.* The three disturbance types chosen and their initial interaction with the boundary layer were studied in the last subsection and we will now compare their continued development. Figure 13 shows the energy as function of time in the initially generated modes and the corresponding dominant quadratic modes (curves with additional markers). The oblique waves (solid) and the initiated two-dimensional wave (dash-dotted) both decay at comparable rate. However, their nonlinearly generated modes develops very differently. The two-dimensional $(2, 0)$ wave (dash-dotted with additional markers) grows for a short time due to the non-linear generation, but then decays like the linear $(1, 1)$ and $(1, 0)$ modes. The vortex/streak $(0, 2)$ mode (solid with markers), nonlinearly generated by the oblique waves, grows substantially until its maximum is reached shortly before $t = 1000$. The disturbance development caused by the initial generation of the vortex/streak mode $(0, 1)$ (dashed) shows a significant difference from the other initiated modes after $t = 200$. At that time the initially generated vortices has diffused deep enough into the boundary layer to cause streak growth together with the cubic $(0, 1)$ part. The $(0, 2)$ mode, non-linearly generated by the initiated $(0, 1)$, also grows and is up to $t = 450$ slightly larger than the $(0, 1)$ mode for this initial energy, which corresponds to a v_{rms} of about 1%.

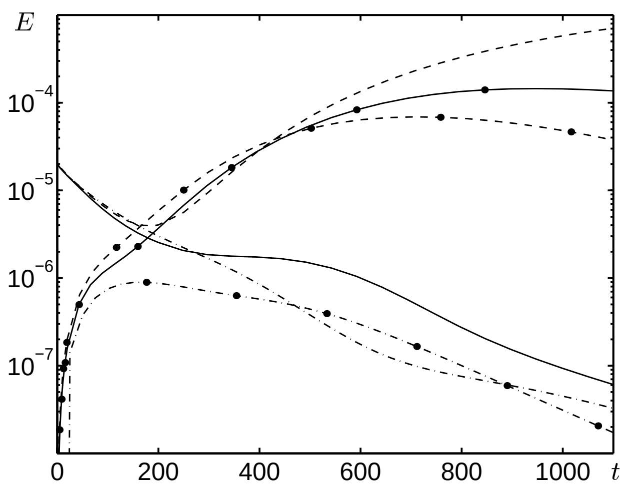

FIGURE 13. Long behavior of the energy for three disturbance types, initiated with the same energy in the free-stream. Solid: oblique waves, dashed: streamwise vortices, dash-dotted: two-dimensional wave. Curves representing non-linearly generated modes are marked with dots.

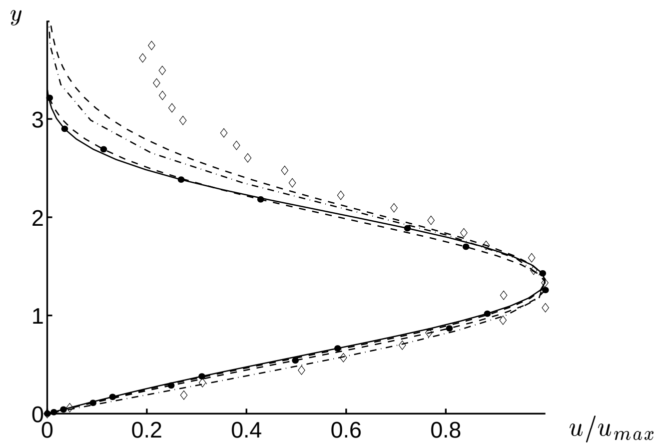

FIGURE 14. Wall normal mode shape in the u-component of growing streaks. Solid with marker: $(0,2)$ mode generated by oblique free-stream waves; dashed: $(0,1)$ initiated in the free-stream; dashed with marker: $(0,2)$ mode generated by streamwise vortices in the free-stream; dash-dotted: results by Anderson, Berggren & Henningson 1998 and diamonds: u_{rms} distribution from experiment by Westin *et al.* 1994 $R = 890$. Note that the Reynolds number based on the displacement thickness at the instant $(t = 600)$ is $R = 930$.

The wall normal mode shape in the u component of the three growing modes previously discussed are plotted figure 14. The shape of what is commonly referred to as a Klebanoff mode is found for all three cases, with the linear mode reaching slightly further into the free-stream. The original Klebanoff mode is the wall normal variation of u_{rms} in experiments with free-stream turbulence and we have included experimental data from Westin *et al.* 1994 in the figure. The fluctuations found in the experiment is caused by the random oscillations of the dominant streaks and the agreement in mode shape between the streak modes and u_{rms} is therefore natural. A consequence of the free-stream turbulence in the experiments are that u_{rms} does not go to zero in the free-stream and whether the experimental mode is associated with the linear or the nonlinear mode shape or both can not be determined.

The linear mechanism is caused by the diffusion of a free-stream vortex into the boundary layer and has been studied by Anderson, Berggren & Henningson 1998 and Luchini 1996, 1997, who assumed the presence a of vortex at the leading edge. Bertolotti 1997 used a different method to calculate the initial vortices but also studied the linear mechanism of streak growth. All these investigators found the Klebanoff mode shape and we have included the results of Anderson, Berggren & Henningson 1998 in figure 14 (dash-dotted curve). The close agreement in wall normal mode shape between experiments and the different theoretical investigations is remarkable considering that methods and initial conditions vary significantly. We mentioned in the introduction that also Choudhari 1996 found a mode shape similar to the Klebanoff mode in his asymptotic investigation of receptivity to vortical free-stream disturbances. Luchini 1997 argued that the reason for this agreement is that the Klebanoff mode shape, or what he also calls a Stewartson 1957 mode of the Libby and Fox 1964 sequence, "is a strong attractor to drive near to itself the velocity profile under most initial conditions".

4.3. Parameter study. In this subsection we will present further results on how the growth of the quadratically generated streaks depend on the initial disturbance characteristics. First the influence of changes in wavenumber is presented and then how the wall normal shape and position effects the growth. To avoid transition, low energy is used in the initial disturbances and the energy in the streak mode will then decay after reaching a maximum at some time T. T will be one of the parameters used to quantify the boundary layer response. The other is the energy reached at T, normalized with the initial disturbance energy squared. This normalization creates a measure independent of the initial energy (cf. figures 5, 7).

4.3.1. *Dependence on wavenumber.* In the study of the wavenumber dependence of the growth we have initiated the disturbances in the free-stream with $l = 5$ and $\lambda = 2$. The top frame in figure 15 displays the growth as function of the streamwise wavenumber (α) for constant $\beta = 0.35$. The largest growth is found for waves with close to zero α and the response then decreases as the wave angle to the mean flow direction increases. The time of maximum is almost independent of the streamwise wavenumber, which is shown in the bottom frame.

In figure 16 the spanwise wavenumber is varied along the horizontal axis and two sets of curves are displayed. The solid curves displays the energy response and the peak time for simulations with $\alpha = 0.1916$ and the dashed ones are results for $\alpha = 0$. In both cases a preferred spanwise wavelength is found, with the optimum for $\alpha = 0$ being lower. The variations in the displayed β range are

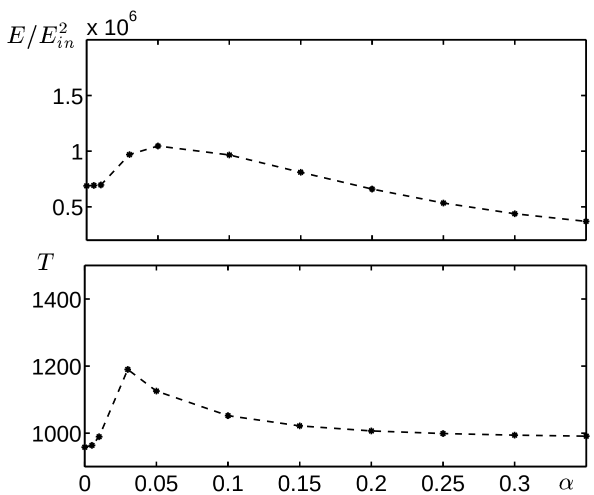

FIGURE 15. Streak response and time of maximum response T as function of streamwise wavenumber, with $\beta = 0.25$.

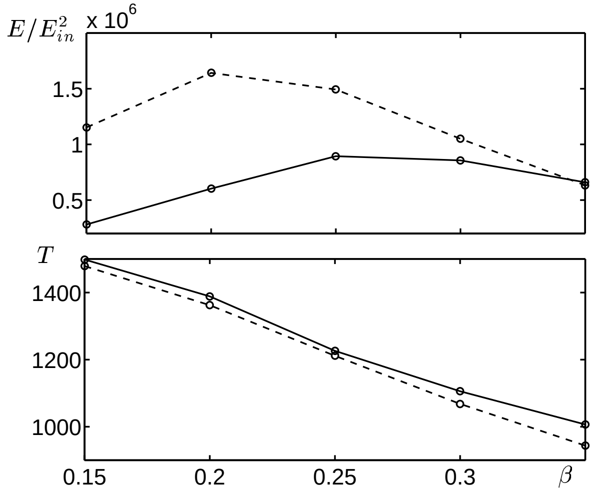

FIGURE 16. Streak response and time of maximum response T as function of spanwise wavenumber. Solid curves represent $\alpha = 0.1916$ and dashed $\alpha = 0$.

however rather small. When the spanwise wavenumber is increased the maximum response is reached earlier.

4.3.2. *Dependence on wall normal position.* The dependence on the disturbance distribution in the wall normal direction is more complicated than the dependence on the wavenumber. We start by discussing changes in the wall normal position, while keeping $\lambda = 2$. The spanwise wavenumber is kept at $\beta = 0.35$ and we again present results for two streamwise wavenumbers $\alpha = 0.1916$ (solid) and $\alpha = 0$ (dashed). The wall normal distance of the lowest disturbance part l is now varied from 0 to 7 in integer steps. Figure 17 displays both the magnitude of the maximum response and the time when it occurs. For $l \geq 3$ the response decreases and T increases as the disturbance is moved away from the wall, for both values of α. The behavior $l < 3$ is more complicated since there is a change in the non-linearly generated vortex pattern. Recall that when the initial disturbance was in the free-stream we found that two layers of vortices were generated whereas only one layer was found when the initial disturbance was close to the wall. The two-layer mode has its maximum earlier than the one-layer mode and the sudden decrease in T for larger values of l, indicates that the two-layer modes dominates. Note that oblique waves give much larger response than streamwise vortices when the disturbance is initiated in the boundary layer, something that has been noted earlier by Schmid, Reddy & Henningson 1996.

4.3.3. *Importance of wall normal velocity.* To investigate the relative importance of the wall normal velocity and the wall normal disturbance size we keep the integrated energy of the disturbance and its lower point ($l = 5$) constant and vary λ. $\alpha = 0.1916$ and $\beta = 0.35$ are also kept constant. An increase of λ means that the wall normal disturbance scale is increased and that disturbance energy is moved further away from the boundary layer. Moreover, as a consequence

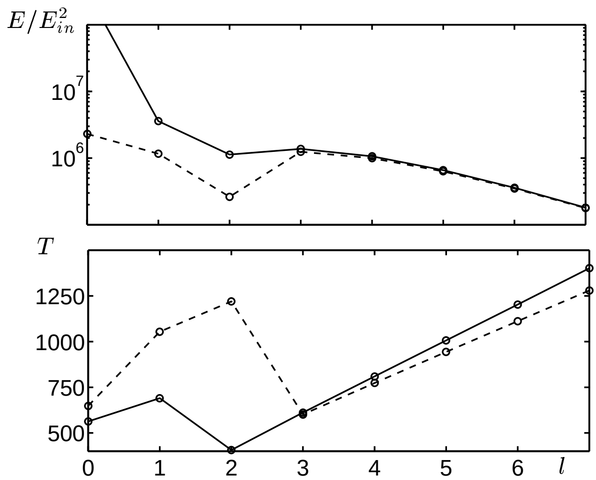

FIGURE 17. Streak growth (top) and time of maximum growth T (bottom) as function of lowest wall normal disturbance initiation point l. $\beta = 0.35$, $\alpha = 0.1916$ (solid) and $\alpha = 0$ (dashed).

of the chosen disturbance shape, increasing wall normal size means increased v fluctuations and decreased u and w fluctuations, which has large influence on the boundary layer response.

The initial energy in the oblique waves is 1e-6 and in the top frame of figure 18 the part of that associated with the v component is plotted versus time. The solid curve represents the smallest wall normal size with $\lambda = 1$. λ then increases in unit steps up the graphs to the final thick line with $\lambda = 5$. The change of disturbance proportion and redistribution of energy into the v-component also reduced the damping of the total energy. The energy response in the u component of the $(0, 2)$ mode are plotted in the middle frame for the five cases. The maximum in the response is later for a large wall normal disturbance and the largest response is found for $\lambda = 4$. The amount of nonlinearly generated v velocity associated with the streamwise vortices are shown in the lowest frame. It is the interaction of this component and the boundary layer shear that generates the large u disturbance displayed in the middle frame. The correlation between the v/vortex component and the u/streak component is obvious. This demonstrates the large importance of the wall normal velocity component in spite that its energy is several orders of magnitude than that in u .

4.4. Optimal perturbations.

4.4.1. *Linear growth.* In theoretical work on non-modal and transient growth the focus is often set on perturbations causing the largest possible energy growth. In this section we compare the growth of the disturbances we are using with those optimal perturbations. Butler & Farrell 1992 found the optimal boundary layer perturbation to have spanwise wavenumber $\beta = 0.65$ and streamwise wavenumber $\alpha = 0$. The amplitude of the initial disturbance was found to have a

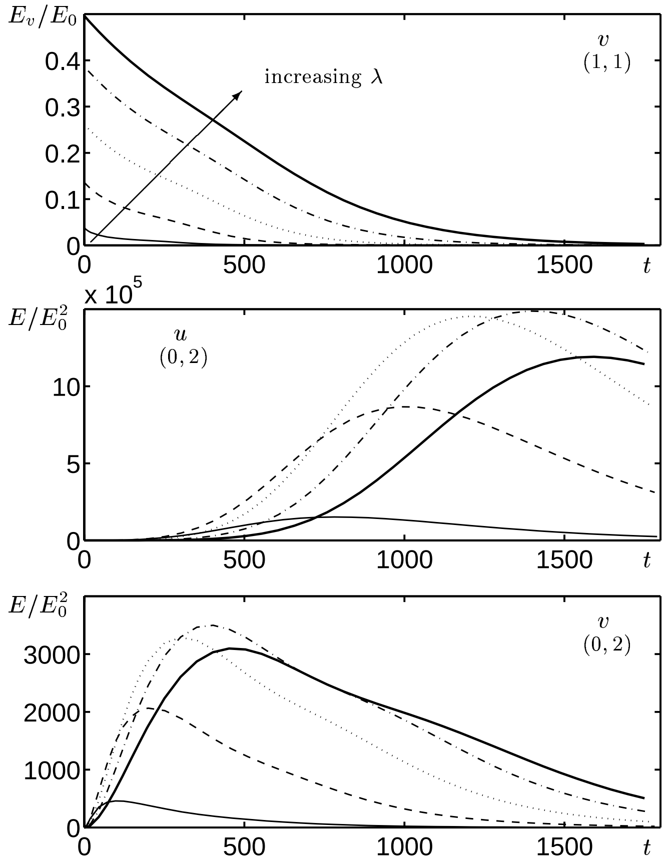

FIGURE 18. Results from simulations with λ varying between 1 (thin) and 5 (thick) and $l = 5$ constant. Top: energy in initiated v component, middle: energy in u of quadraticly generated $(0, 2)$ mode, bottom: energy in v of quadraticly generated $(0, 2)$ mode. Note the different normalization of the linear and the nonlinear modes.

maximum at approximately $y = 2$ and the disturbance reached to approximately $y = 5$. For Reynolds number 400, that we have used for our simulations, the optimal would at $t = 310$ be amplified 240 times. The theory is linear and with the assumption that the boundary layer is parallel. The simulations were hence performed with a constant boundary layer thickness and the comparisons are made with the initiated $(0, 1)$ mode. Using $l = 0$ and $\lambda = 2.5$ we found an initial disturbance close to the one which gave the theoretical maximum, and by setting the initial energy to 1×10^{-9} we removed the nonlinear effects. With $\alpha = 0$ we found $\beta = 0.66$ to give a maximal amplification of 179 times at $t = 344$. Variations of the spanwise wavenumber in the range $0.60 < \beta < 0.70$ did not lower the amplification below 176 times but making the wall normal shape slightly asymmetric increased the amplification to 201 times. These values are fairly close to the optimal ones presented by Butler & Farrell 1992.

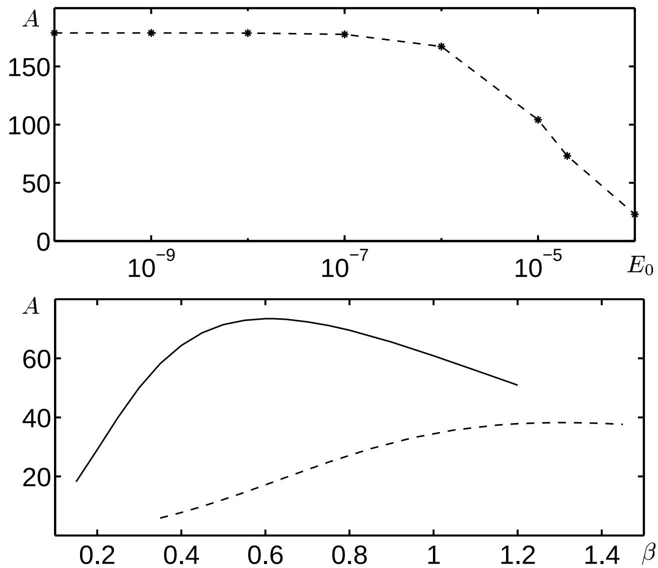

FIGURE 19. Top: amplification A as function of initial amplitude. Bottom: amplification as function of β for two different λ. Vortices are initiated in the boundary layer with $l = 0$ and $\lambda = 2.5$ (solid) or $\lambda = 1.0$ (dashed).

4.4.2. *Nonlinear effects.* Nonlinear interactions drain energy from the initiated $(0, 1)$ mode. To investigate how that effected our optimal perturbation we kept the disturbance shape ($l = 0$ and $\lambda = 2.5$) and used $\beta = 0.65$ and varied the initial amplitude. The amplification decreases as nonlinear effects becomes stronger, which is shown in the top frame of figure 19. The maximum is reached earlier when the nonlinear energy exchange increases and the growth of the nonlinearly generated $(0, 2)$ is obviously increased several orders of magnitude. We also checked if the nonlinear interactions affected the optimal β and for that we picked the initial amplitude 2×10^{-5}. In the bottom frame of figure 19 the maximum amplification A of the initiated $(0, 1)$ mode is plotted versus β for two sets of simulations. The solid line corresponds to simulations where the wall normal disturbance shape was the same as we used in the linear investigation, with $\lambda = 2.5$ and $l = 0$. The maximal amplification was reduced to be 73 times by the nonlinear effects and that maximum was reached already at $t = 243$ for spanwise wavenumber $\beta = 0.61$. A smaller wall normal disturbance size with $\lambda = 1$, is represented by the dashed lines and gave also a smaller spanwise scale. The optimal β was then found to be 1.30 and was amplified 38 times at $t = 88$. As both amplification curves are very flat around the peak, one can not expect amplification differences to be very selective for spanwise wavenumbers.

The relation between the wall normal and spanwise size of the initiated vortex is important and the amplification is more selective to the wall normal size than to changes of β. We therefore investigated the optimal wall normal size for some spanwise wavenumbers. The optimal λ was found to vary around 2.5. For small β it increased to 3.0 and for large it decreased to 2 such that the spanwise and wall normal scales of the initial vortices were kept approximately equal. Note that the wall normal scale of the vortex is larger than the boundary layer thickness. When λ is 2.5 the center of the vortices are at $y = 2.5$ and that is were the v component has its wall normal maximum. This is position is close to the boundary layer edge, δ_{99} being 2.8. We also found that the maximum disturbance amplitude was reached earlier when β was increased, which is what the theoretical findings predict.

Still initiating the $(0,1)$ mode inside the boundary layer, we investigated what parameter combination gave the largest response in the nonlinearly generated $(0,2)$ mode. The same wall normal scale, $\lambda = 2.5$, as when we optimized for growth of $(0,1)$ was again found to give the largest response. The spanwise wavenumber of the initial vortices giving the largest response in $(0,2)$ was $\beta = 0.30$, which gives a spanwise wavenumber of $\beta = 0.60$ in the $(0,2)$ mode. That is again close to optimal found when we optimized for growth in $(0,1)$.

5. Conclusions and Discussion

Our numerical experiments on how simple wave-like disturbances effect a laminar boundary layer has identified two mechanisms. A new nonlinear mechanism and a linear mechanism that is related to the investigations by Luchini 1997, Bertolotti 1997 and Andersson, Berggren & Henningson 1998. Both mechanisms result in growing streamwise streaks and they are therefore most relevant to experiments with free-stream turbulence, where streaks are the dominant flow characteristics. The nonlinear mechanism however, is also able to create oblique and two-dimensional disturbances at low level in the boundary layer (figures 10, 11), which in some cases might be a relevant source of background noise in the transition process.

Previous investigators have considered the receptivity of streamwise vortices present in the free-stream turbulence. The most important feature of the new nonlinear mechanism is that it can cause streak growth from oblique disturbances in the free-stream. We have also shown that for moderate disturbance levels (figure 13) the growth caused by the nonlinear mechanism is comparable to that caused by the linear mechanism. At low disturbance levels the linear mechanism may dominate, with the nonlinear mechanism setting in at higher disturbance levels. Experiments do not give the answer to that at present. Kendall 1990 found the streak amplitude to depend linearly on the free-stream turbulence level, which was very low in his experiments. Westin *et al.* 1994, as previously stated, could not find a correlation between turbulence level, streak amplitude and transitional Reynolds number in the experiments reported in literature.

Normally experimental investigators only report the turbulence level in the streamwise velocity component. We have shown the great importance of the wall normal velocity component, which also found by Yang & Voke 1993. To find correlations or good transition prediction models the wall normal turbulence level should be observed instead. The fact that calculations based on initial conditions without streamwise velocity perturbations give good results, is an other indication of that.

Bertolotti's 1997 theory predicts a most amplified spanwise wavelength and he uses experimental results by Klebanoff (reported by Herbert and Lin) and Westin *et al.* 1994 to suggest that there is a selectivity for that wavelength in the experiments. In his comparison with the results of Westin *et al.* 1994, Bertolotti 1997 unfortunately has missed the fact that Westin *et al.* 1994 bases their Reynolds number on the displacement thickness. A correct scaling of the data obtained by Westin *et al.* 1994, however, shows that the spanwise scale of their streaks are very different to results reported by Klebanoff and Bertolotti's 1997 most amplified spanwise wavelength. Andersson, Berggren & Henningson 1998 speculates in a universality of their optimization results, which implies also a universality of spanwise scales. Our investigation indicates that the selectivity for spanwise wavenumber is small and the wavelength found in an experiments would depend on the free-stream scales, which was Klebanoff 1990 found.

The growth rates in the calculations by Andersson, Berggren & Henningson 1998 and Bertolotti 1997 decreases after some downstream position in a manner that does not agree with experiments. The simple vortical free-stream disturbances in this investigation shows that free-stream turbulence have the possibility to continuously force streaks in the boundary layer, even downstream of the leading edge. This additional forcing may be what is missing in the other calculations to prevent the decreased streak growth.

The spanwise spacing of the streaks are increasing downstream in the experimental investigations. The optimization procedure by Andersson, Berggren & Henningson 1998 offers the explanation the the optimal spanwise wavelength changes downstream. Their optimization results predicts the best agreement with the experiment by Westin *et al.* 1994 and a downstream growth of the spanwise scale proportional to $\sqrt{x}$, which is significantly faster than what is found in the experiment. A continuous forcing from the free-stream could also result in downstream changing scales as the optimal streak changes with boundary layer thickness.

To give us the final answer, these speculations need to be investigated by large spatial computation with more realistic free-stream disturbances, more experiments and improved theoretical models for calculations.

Acknowledgment

We thank Dr. J. Westin and Mr. P. Andersson for making their data available and Mr. P Anderson for interesting discussions. This work has been supported by TFR (Swedish Research Council for Engineering Sciences).

References

Andersson, P., Berggren, M. & Henningson, D. 1998. Optimal disturbances and bypass transition in boundary layers. *Phys. Fluids.* . (Submitted).

Berlin, S., Lundbladh, A. & Henningson, D. S. 1994. Spatial simulations of oblique transition. *Phys. Fluids.* **6**, 1949–1951.

Berlin, S., Wiegel, M. & Henningson, D. S. 1998. Numerical and experimental investigation of oblique boundary layer transition. Submitted to jfm.

Bertolotti, F. P. 1997. Response of the blasius boundary layer to free-stream vorticity. *Phys. Fluids.* **9** (8), 2286–2299.

BERTOLOTTI, F. P., HERBERT, T. & SPALART, P. R. 1992. Linear and nonlinear stability of the Blasius boundary layer. *J. Fluid Mech.* **242**, 441–474.

BLAIR, M. F. 1992. Boundary-layer transition in accelerating flows with intense freestream turbulence: Part 1 disturbances upstream of transition onset. *Journal of Fluid Engineering.* **114**, 313–321.

BOIKO, A. V., WESTIN, K. J. A., KLINGMANN, B. G. B., KOZLOV, V. V. & ALFREDSSON, P. H. 1994. Experiments in a boundary layer subject to free-stream turbulence. Part II: The role of TS-waves in the transition process. *J. Fluid Mech.* **281**, 219–245.

BUTER, T. A. & REED, H. L. 1994. Boundary layer receptivity to free-stream vorticity. *Phys. Fluids.* **6**, 3368–3379.

BUTLER, K. M. & FARRELL, B. F. 1992. Three-dimensional optimal perturbations in viscous shear flow. *Phys. Fluids A.* **4**, 1637–1650.

CHOUNDHARI, M., 1996. Boundary-layer receptivity to three-dimensional unsteady vortical disturbances in free stream. AIAA Paper 96-0181.

ELOFSSON, P. A. & ALFREDSSON, P. H. 1997. An experimental investigation of oblique transition in a Blasius boundary layer. In *EUROMECH Colloquium 359.*

GOLDSTEIN, M. E. & HULTGREN, L. S. 1989. Boundary-layer receptivity to long-wave free-stream disturbances. *Ann. Rev. Fluid Mech.* **21**, 137–166.

GUSTAVSSON, L. H. 1991. Energy growth of three-dimensional disturbances in plane Poiseuille flow. *J. Fluid Mech.* **224**, 241–260.

HERBERT, T. 1988. Secondary instability of boundary layers. *Ann. Rev. Fluid Mech.* **20**, 487–526.

KACHANOV, Y. S. 1994. Physical mechanisms of laminar-boundary-layer transition. *Ann. Rev. Fluid Mech.* **26**, 411–482.

KENDALL, J. M., 1985. Experimental study of disturbances produced in a pre-transitional laminar boundary layer by weak freestream turbulence. AIAA Paper 85-1695.

KENDALL, J. M., 1990. Boundary layer receptivity to freestream turbulence. AIAA Paper 90-1504.

KERSCHEN, E. J., 1985. Experimental study of disturbances produced in a pre-transitional laminar boundary layer by weak freestream turbulence. AIAA Paper 85-1695.

KERSCHEN, E. J. 1990. Boundary layer receptivity theory. *Appl Mech Rev.* **43** (5, Part 2), S152–157.

KIM, J., MOIN, P. & MOSER, R. 1987. Turbulence statistics in fully developed channel flow. *J. Fluid Mech.* **177**, 133–166.

KLEBANOFF, P. S. 1971. Effect of freestream turbulence on the laminar boundary layer. *Bull. Am. Phys. Soc.* **10**, 1323.

KLEISER, L. & ZANG, T. A. 1991. Numerical simulation of transition in wall-bounded shear flows. *Ann. Rev. Fluid Mech.* **23**, 495–537.

LIBBY, P. A. & FOX, H. 1964. Some perturbation solutions in laminar boundary-layer theory. *J. Fluid Mech.* **17**, 433–449.

LIN, N., REED, H. L. & SARIC, W. S. 1992. Effect of leading-edge geometry on boundary-layer receptivity to freestream sound. In *Instability, Transition and Turbulence* (HUSSAINI, M. Y., KUMAR, A. & STREETT, C. L., editors), pp. 356–366. Springer-Verlag.

LUCHINI, P. 1996. Reynolds number independent instability of the Blasius boundary layer over a flat surface. *J. Fluid Mech.* **327**, 101–115.

LUCHINI, P. 1997. Reynolds number independent instability of the Blasius boundary layer over a flat surface. part 2: optimal pertubations. Submitted to jfm.

LUNDBLADH, A., HENNINGSON, D. S. & JOHANSSON, A. V., 1992. An efficient spectral integration method for the solution of the Navier-Stokes equations. FFA-TN 1992-28, Aeronautical Research Institute of Sweden, Bromma.

LUNDBLADH, A., SCHMID, P. J., BERLIN, S. & HENNINGSON, D. S., 1994. Simulation of bypass transition in spatially evolving flows. Proceedings of the AGARD Symposium on Application of Direct and Large Eddy Simulation to Transition and Turbulence, AGARD-CP-551.

MALIK, M. R., ZANG, T. A. & HUSSAINI, M. Y. 1985. A spectral collocation method for the Navier-Stokes equations. *J. Comp. Phys.* **61**, 64–88.

Morkovin, M. V. 1969. The many faces of transition. In *Viscous Drag Reduction* (Wells, C. S., editor). Plenum Press.

Nishioka, M. & V., M. M. 1986. Boundary-layer receptivity to unsteady pressure gradients: experiment and overview. *J. Fluid Mech.* **171**, 219–261.

Reddy, S. C. & Henningson, D. S. 1993. Energy growth in viscous channel flows. *J. Fluid Mech.* **252**, 209–238.

Reddy, S. C., Schmid, P. J., Bagget, J. S. & Henningson, D. S., 1997. On stability of streamwise streaks and transition thresholds in plane channel flow. submitted to jfm.

Schlichting, H., 1933. Zur Entstehung der Turbulenz bei der Plattenströmung. Nachr. Ges. Wiss. Göttingen, 181–208.

Schmid, P. J. & Henningson, D. S. 1992. A new mechanism for rapid transition involving a pair of oblique waves. *Phys. Fluids A.* **4**, 1986–1989.

Schmid, P. J., Reddy, S. C. & Henningson, D. S. 1996. Transition thresholds in boundary layer and channel flow. In *Advances in Turbulence VI* (Gavrilakis, S., Machiels, L. & Monkewitz, P. A., editors), pp. 381–384. Kluwer Academic Publishers.

Spalart, P. R. & Yang, K. 1987. Numerical study of ribbon induced transition in blasius flow. *J. Fluid Mech.* **178**, 345–365.

Stewartson, K. 1957. On asymptotic expansion in the theory of boundary layer. *J. Math. Phys.* **36**, 137.

Tollmien, W., 1929. Über die Entstehung der Turbulenz. Nachr. Ges. Wiss. Göttingen, 21–44. (English translation NACA TM 609, 1931).

Trefethen, L. N., Trefethen, A. E., Reddy, S. C. & Driscoll, T. A. 1993. Hydrodynamic stability without eigenvalues. *Science.* **261**, 578–584.

Westin, K. J. A., Boiko, A. V., Klingmann, B. G. B., Kozlov, V. V. & Alfredsson, P. H. 1994. Experiments in a boundary layer subject to free-stream turbulence. Part I: Boundary layer structure and receptivity. *J. Fluid Mech.* **281**, 193–218.

Wiegel, M. 1997. *Experimentelle Untersuchung von kontrolliert angeregten dreidimensionalen Wellen in einer Blasius-Grenzschicht.*, volume 312 of *VDI Fortschritt-Bericht Reihe 7*. VDI-Verlag, Düsseldorf (Germany). Dissertation zum Dr.-Ing. an der TH Hannover, Dezember 1996.

Yang, Z. Y. & Voke, P. R. 1993. Large-eddy simulation of transition under turbulence. Technical Report ME-FD/93.12, University of Surrey, Dept. Mech. Eng.

Paper 5

P5

CONTROL OF OBLIQUE TRANSITION BY FLOW OSCILLATIONS

S. Berlin
Dept. of Mech., KTH, S-100 44 Stockholm, Sweden

J. Kim
MAE Dept., UCLA, CA 90095-1597 Los Angeles, USA

D. S. Henningson
FFA, Box 11021, S-16111 Bromma, Sweden

Abstract. Transition delay caused by spanwise flow oscillations of a Blasius boundary layer is studied. The oscillations is driven either by a moving wall or a body force that is exponentially decaying away from the wall. The latter can be realized by a Lorenz force that can be generated from an array of magnets and electrodes on a wall. The control strategies are found to delay oblique transition and prevent transition caused by a random disturbance. The the flow caused by the body force reached further out from the wall compared to that set up by the moving wall, which made it more efficient for transition delay.

1. Introduction

Delaying laminar-to-turbulent transition has many obvious advantages and the simplest method is perhaps to shape the surface on which the boundary layer develop such that a suitable pressure distribution is obtained. Other approaches aiming for a more stable mean flow profile include application of heating/cooling, suction and magneto-hydrodynamic (MHD) forces and has been reviewed by Gad-el-Hak (1989). The later control tools has also been used for active wave cancellation. The purpose has then been to cancel growing Tollmien-Schlichting (TS) waves or waves associated with the secondary instability caused by TS-waves, see for example Thomas (1983), Kleiser & Laurien (1985), and Danabasoglu, Biringen & Streett (1991). The bypass transition scenarios in the present study are, however, characterized by streamwise streaks and vortices rather than two-dimensional waves.

Recent studies (Choi, Moin & Kim 1993) have shown that near-wall streamwise vortices are responsible for high skin-friction drag in turbulent boundary layers and successful control strategies are found to reduce their strength. Even if those vortices are found closer to the wall and of smaller wall normal scale than those observed in transition, it is well worth investigating if the same type of control used for drag reduction can be applied on transition caused by streamwise vortices.

Akhavan, Jung & Mangiavacchi (1993) showed that a spanwise oscillatory motion of a wall or an oscillatory spanwise crossflow reduced turbulence and skin-friction. The oscillating spanwise flow was in that case driven by a pressure gradient, while our idea have been to instead use a body force. In their experiment Nosenchuck & Brown (1993) achieved viscous drag reduction by letting a wall normal directed Lorenz force interact with the turbulent structures. Gailitis & Lielausis (**?**) considered spanwise periodically distributed magnetic fields and electric currents generated from the boundary layer wall and showed that it gave a streamwise force exponentially decaying in the wall normal direction (Tsinober 1989). Their aim was to stabilize boundary layer profiles in sea water or use the force for propulsion. Kim *et al.* (1995, 1996) considered the same device as Gailitis & Lielausis turned 90 degrees and an oscillating electric current to produced an oscillating spanwise force. They reported that the oscillating Lorenz force prevented the interaction of streamwise vortices with the wall and that skin friction was reduced in turbulent channel flow. Berlin *et al.* (1996) used the same approach to delay boundary layer transition.

In the present investigation we have studied the possibility of transition delay by spanwise flow oscillations generated by either a body force exponentially decaying in the wall normal direction or a moving wall. After the presentation of the numerical method §2 we briefly describe the two transition scenarios considered §3 and the flow generated by the control devices §4 before the results are presented in §5.

2. Numerical method

The simulation code (Lundbladh, Schmid, Berlin & Henningson 1994) used for the present computations uses spectral methods to solve the three-dimensional, time dependent, incompressible Navier-Stokes equations. The algorithm uses Fourier representation in the streamwise and spanwise directions and Chebyshev polynomials in the wall-normal direction and pseudo-spectral treatment of the nonlinear terms. The time advancement used was a four-step low storage third-order Runge-Kutta method for the nonlinear terms and a second-order Crank-Nicholson method for the linear terms. Aliasing errors from the evaluation of the nonlinear terms were removed by the $\frac{3}{2}$-rule when the horizontal FFTs were calculated. In order to set the free-stream boundary condition closer to the wall, a generalization of the boundary condition used by Malik, Zang & Hussaini (1985) was implemented. It is an asymptotic condition applied in Fourier space with different coefficients for each wavenumber that exactly represents a potential flow solution decaying away from the wall. A temporal approximation has been used for all the presented simulation results.

The basis of the temporal simulation technique is the thought of a localized disturbance or wave traveling downstream, surrounded by a boundary layer of constant thickness which grows slowly in time. The extent of the computational domain is small as only one wave length of the largest disturbance is included in the streamwise and spanwise directions. Moreover, the approximation that the boundary layer thickness is constant at each instant of time is made, which enables us to use periodic boundary conditions in the wall parallel directions. The parallel approximation requires that a (weak) forcing is added to the streamwise momentum equation in order to ensure the correct development of the boundary layer profile over extended periods of time. The boundary layer thickness has in this investigation been set to grow with the same rate as an observer following the outer flow would experience. Compared to a simulation with constant boundary layer thickness transition occurs faster with the current setting. The basic physical mechanisms we have studied are, however, the same regardless of pace of boundary layer growth.

The simulations presented below were started at Reynolds number $R = 664$, where $R = U_\infty \delta_0^*/\nu$, ν the kinematic viscosity, U_∞ the free stream velocity and δ_0^* the displacement thickness at time $t = 0$. The two later quantities has been used to non-dimensionalize all variables. The computational box had the dimensions $52.84 \times 15 \times 75.93$ in the streamwise x, wall normal y and spanwise z directions, respectively and the resolution was at least $32 \times 97 \times 32$ spectral modes. Some simulations with up to $96 \times 145 \times 216$ modes were performed and the transition point was then delayed approximately 50 time units but that was consistent for all cases both with and without control. The relation between the transition times for different control parameters that we present is therefore not effected by the resolution issue. To give exact numbers that can be compared with experimental results, spatial simulations must be performed that correctly accounts for the boundary layer growth.

3. Controlled transition scenarios

3.1. Oblique transition. Two transition scenarios has been studied. The focus has been on oblique transition, which is a bypass transition scenario initiated by two oblique waves with opposite wave angle. It has been studied in boundary layer flow both numerically and experimentally (Berlin, Lundbladh & Henningson 1994, Wiegel 1997, Elofsson & Alfredsson 1997 and Berlin, Wiegel & Henningson 1998) and found to be a powerful mechanism that is active also at subcritical Reynolds numbers. The nonlinear interaction of the oblique waves generates counter rotating streamwise vortices that are causing growth of streamwise velocity streaks in the boundary layer. The growth mechanism is explained by the theories on non-modal growth (Gustavsson 1991, Butler & Farell 1992, Reddy & Henningson 1993 and Trefethen *et al.* 1993) and is physically due to what has been called the lift-up effect. The counter rotating vortices interacts with the wall normal shear in the boundary layer and lifts up low velocity fluid elements from the wall towards the free-stream and vice versa.

The streamwise and spanwise wavenumbers of the oblique waves were in the current investigation chosen to $\alpha_0 = 0.1189$ and $\beta_0 = 8.274 \cdot 10^{-2}$, respectively. These parameters are similar to those used in the investigation of Berlin, Wiegel & Henningson (1998), as is the Reynolds number. That investigation was spatial and a complete agreement can therefore not be expected.

The streamwise velocity in a wall parallel plane inside the boundary layer at four time instances during the transition process are displayed in figure 1. The flow is from left to right and red represents low speed increasing over yellow and green to high speed blue. The top left figure shows the pattern of the initial oblique waves. At $t = 300$ meandering streaks has been formed and they grow to become more irregular at $t = 500$. The flow is fully turbulent at $t = 800$ and

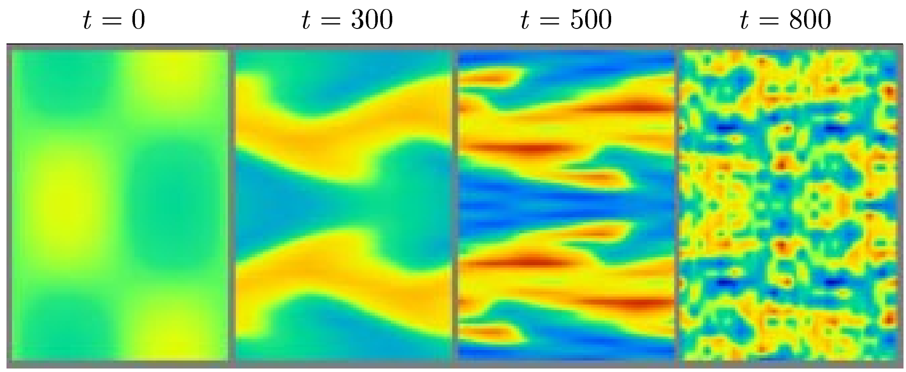

FIGURE 1. Streamwise velocity in wall parallel planes at $y = 1.2$ during oblique transition. Flow is from left to right and the velocity increases from red to blue over yellow and green.

at that stage not fully resolved but our interest is in the onset of transition and not in the turbulent flow.

We transform the velocity field to Fourier space and use the notation (α, β), where α and β are the streamwise and spanwise wavenumber respectively, each normalized with the corresponding wavenumber of the oblique waves. Thus the oblique waves are represented by $(1, 1)$ and $(1, -1)$ and the streaks by $(0, 2)$. As the flow is symmetric and (α, β) equal to $(\alpha, -\beta)$, we only display modes with positive β in figure 2. At $t = 0$ only the $(1, 1)$ mode is non-zero and it only increases slightly as t increases. The nonlinearly generated vortex/streak mode $(0, 2)$ is seen to grow rapidly and along with it the $(1, 3)$ mode. After $t = 400$ other modes are also growing and at the turbulent final stage the energy in all modes are of the same order.

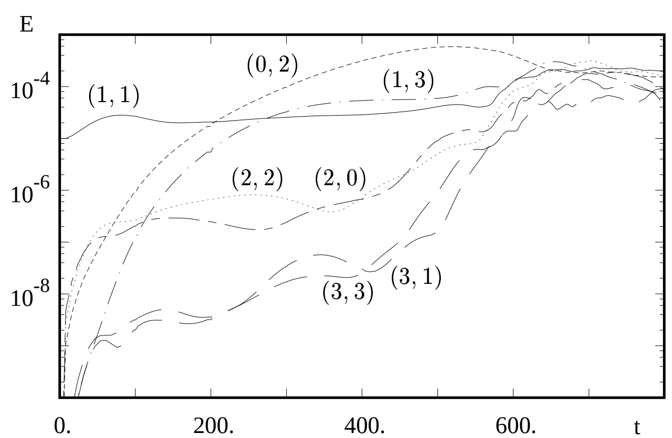

FIGURE 2. Time evolution of the energy in the most energetic Fourier modes during oblique transition.

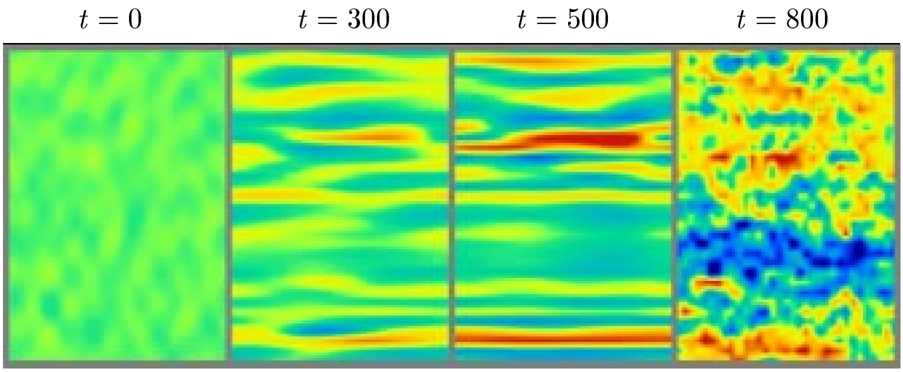

FIGURE 3. Streamwise velocity in wall parallel planes at $y = 1.2$ during transition initiated by random disturbances. flow is from left to right and velocity increases from red to blue over yellow and green.

3.2. Transition caused by random disturbances. For comparison we have also studied a transition scenario were the initial disturbance energy was randomly distributed in the 8, 16 and 13 lowest spectral modes in the x, y and z directions, respectively. The total disturbance energy was twice that used in the initiated oblique waves in order to get approximately the same transition time.

The streamwise velocity inside the boundary layer are displayed in figure 3 at the same time and wall normal position as for the oblique waves. The random distribution at $t = 0$ is displayed in the left square. The pattern observed at $t = 300$ is again streaky and the strength has also increases at $t = 500$ as for oblique transition. The streakyness may indicate the the same basic mechanism is causing transition as in the oblique case. At $t = 800$ the flow is turbulent but a streamwise elongated characteristic is still present. That is explained by the observation that the $(0, 1)$ streak mode contains more energy than the other

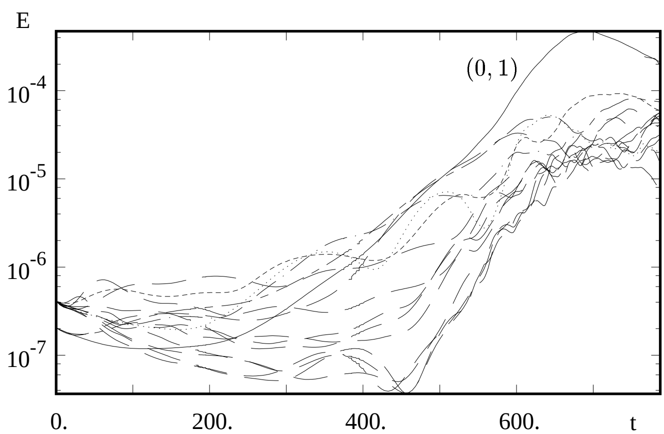

FIGURE 4. Time evolution of the energy in some Fourier modes during transition initiated by random disturbances. Solid represents the $(0, 1)$ mode.

modes at large times in figure 4. Apart from that we note that it is after $t = 400$ that all modes grow and that the energy curves level off at a lower level in this case than it did after oblique transition.

4. Control strategy

The two applied control strategies caused spanwise oscillation of the flow in the boundary layer. In the first we applied a spanwise oscillating body force of the form

$$F_z = f_0 e^{-y/c} \cos(\omega t), \tag{1}$$

where f_0 is an amplitude, ω the oscillation frequency and c a parameter controlling the wall normal decay. We will use the triplet (f_0, c, ω) to refer to these force parameters. The force itself is not significant for the control but rather the spanwise flow that it causes. If the wall normal velocity component of the mean flow is neglected, which it is in the temporal approximation, the flow caused by the force has the form

$$w(y, c, \omega) = A\sqrt{e^{-2\gamma y} + e^{-2y/c} - 2\cos(\gamma y) e^{-(\gamma + 1/c)y}} \tag{2}$$

where

$$A = \sqrt{\frac{(f_0 R)^2 c^4}{1 + (\omega R)^2 c^4}}, \quad \gamma = \sqrt{\frac{\omega R}{2}} \tag{3}$$

The expressions (3) reveals that a change of the oscillation frequency will also affect both amplitude and wall normal distribution of the spanwise flow. That is also true for changes of the decay parameter c. It is therefore not possible to solely change either frequency or wall normal distribution of the spanwise flow. By adjusting all parameters it is, however, possible to come fairly close to such changes and we will present the actual spanwise flow profiles used below. An example of force and flow profile is found in the left plot of figure 5.

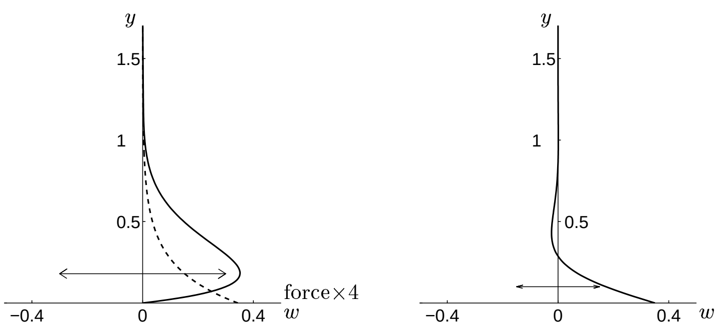

FIGURE 5. Left: spanwise oscillating flow profile (solid) caused by the spanwise oscillating body force (dashed). Right: spanwise oscillating flow profile caused by a spanwise oscillating wall.

The right plot contains the flow profile set up by an spanwise oscillating wall, which was the second type of control applied in the present investigation. The expression for w is then

$$w = Ce^{-\gamma y}\cos(\gamma y), \tag{4}$$

where γ is given above and C is the amplitude.

5. Results

5.1. Control of oblique transition.

5.1.1. *Control by body force.* The transition delay achieved by our control strategies depend on a number of parameters and we will first present the results associated with the body force applied to oblique transition. Selecting $\omega = 0.09$ and $c = 0.22$ we found that an increased spanwise flow amplitude generally led to further transition delay. However, an optimum was found after which increased flow amplitude actually reduced the transition delay. This is illustrated in the left frame of figure 6, where the friction coefficient is plotted as function of time for four controlled flows. The latest transition is found for the second highest spanwise flow amplitude corresponding to the dashed curve. The spanwise flow profiles for the three cases are plotted in the right frame. In the plot of friction coefficient we have also included a thicker curve corresponding to the case without control.

The effect of changes in the spanwise oscillating flow profile is shown in figure 7. The two middle flow profiles performs best. The transition delay is less if the spanwise flow is concentrated close to the wall or if a large wall normal proportion of the boundary layer is oscillating. The purpose of the control is to break the flow structures causing transition, and one may interpret these results in the following manner. If the whole structure is moved (the highest flow profile) or if the relevant structures are not affected (the lowest profile), they will not

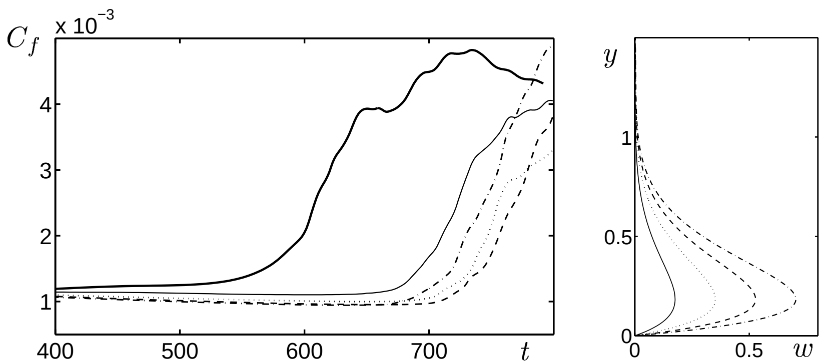

FIGURE 6. Left: coefficient of friction Right: oscillating spanwise flow profiles, for $f_0 = 0.043$ (solid), $f_0 = 0.086$ (doted), $f_0 = 0.129$ (dashed), $f_0 = 0.172$ (dash-doted), $c = 0.22$ and $\omega = 0.09$. The thick curve in the left figure represents the uncontrolled case.

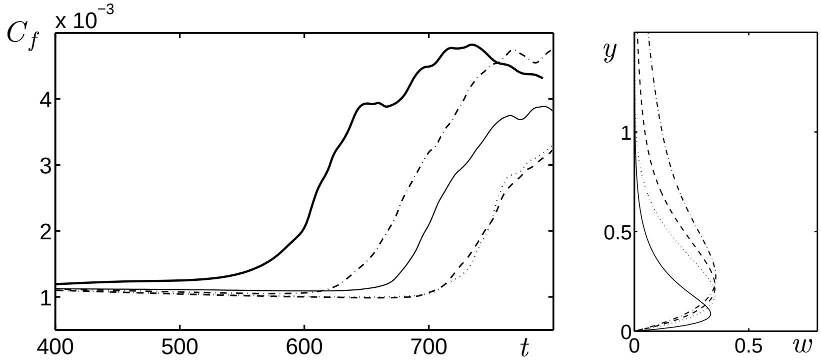

FIGURE 7. Left: coefficient of friction Right: oscillating spanwise flow profiles, for force parameters $(0.43, 0.05, 0.09)$ (solid), $(0.086, 0.22, 0.09)$ (doted), $(0.060, 0.38, 0.09)$ (dashed) and $(0.046, 0.7, 0.09)$ (dash-doted). The thick curve in the left figure represents the uncontrolled case.

be broken by the spanwise flow oscillations and therefor the resulting transition delay will be less.

When the dependence of the transition time on the forcing frequency was investigated, all the control parameters has to be adjusted in order to keep the flow profile as constant as possible. The frequency was varied from 0.039 to 0.4 and the flow profiles used all fell within the region enclosed by the three profiles displayed in the left frame of figure 8. The dash-dotted curve corresponds to the highest frequency and it was not possible to avoid the movement of the profile peak towards the wall for the high frequencies without extending the profile further in the wall normal direction, which reduced the achieved transition delay considerably, as noted in figure 7. The transition time dependence on forcing frequency is displayed in the middle frame of figure 8, where the transition time is

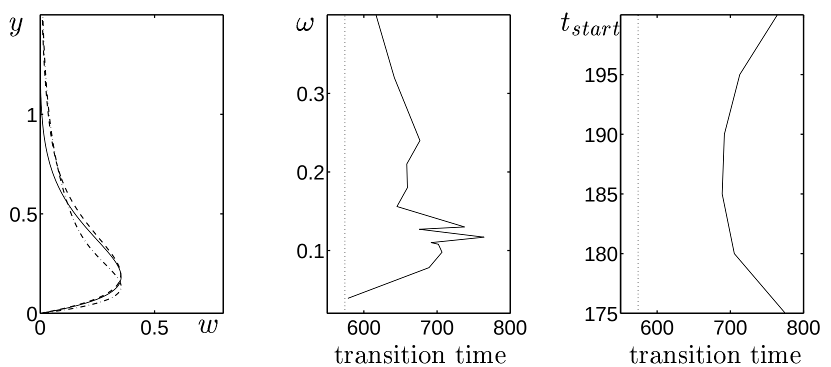

FIGURE 8. Left: Flow profiles used for frequencies: 0.0782 (solid), 0.13 (dash), 0.156 (dash-dot) and 0.40 (dot). Middle: frequency dependence of transition time. Right: Transition time dependence on start time of forcing.

defined as the instant when the friction coefficient exceeds 1.7 times the laminar value. The vertical dotted line marks the transition time for the no-control case and for low frequency forcing the transition time curve is almost on that line. The transition delay decreases for frequencies higher than 0.24.

The odd behavior in the frequency range $0.1 < \omega < 0.2$ is caused by differences in the flow resulting from the turn on of the forcing. The right frame displays the transition time for different start time of the forcing for $\omega = 0.117$. Start time 175 and 200 gave the same transition delay whereas a start time in between gave earlier transition. The forcing amplitude was smoothly ramped up to its final value during the first 30 time units and the phase of the forcing was the same in all cases, which means that the forcing at $t = 230$ was identical for all cases. The periodicity found in the curve corresponds to half the time period of the forcing which is much shorter than the period of the oblique waves. This implies that the setup of the initial spanwise flow is of great importance for the transition delay in the frequency range $0.1 < \omega < 0.2$. This behavior was not observed for higher frequencies. Disregarding this periodic behavior, transition was not delayed further by initiating the control earlier than $t = 200$ but later initiation gave less transition delay. Note that control during a specific time period in the temporal approximation corresponds to forcing over a limited downstream extent in an experiment.

5.1.2. *Control by wall oscillations.* The transition delay of oblique transition observed when the boundary layer wall was oscillated in the spanwise direction, was less than that achieved with the body force. This could be expected considering that the transition delay was reduced when the spanwise flow caused by the body force was concentrated close to wall. The flow caused by the oscillating wall is obviously closer to the wall. The flow also becomes more concentrated to the wall region for higher oscillation frequencies, which we in figure 9 find to give less transition delay. In the investigation of how the transition time depend on the frequency we used a maximum wall speed of 0.35. The transition delay was for $\omega = 0.09$ found to increases with wall speed up to 0.6 and thereafter is

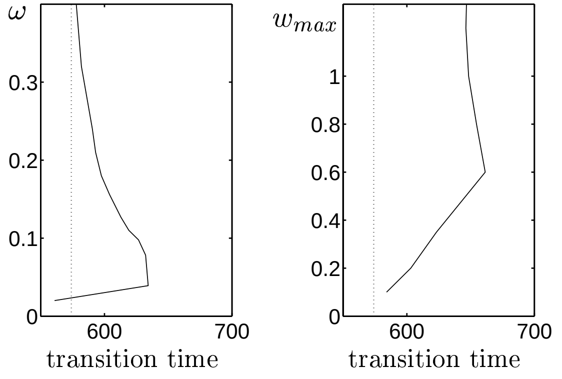

FIGURE 9. Transition time dependence on the frequency of the spanwise oscillating wall (left) and the maximum wall speed (right).

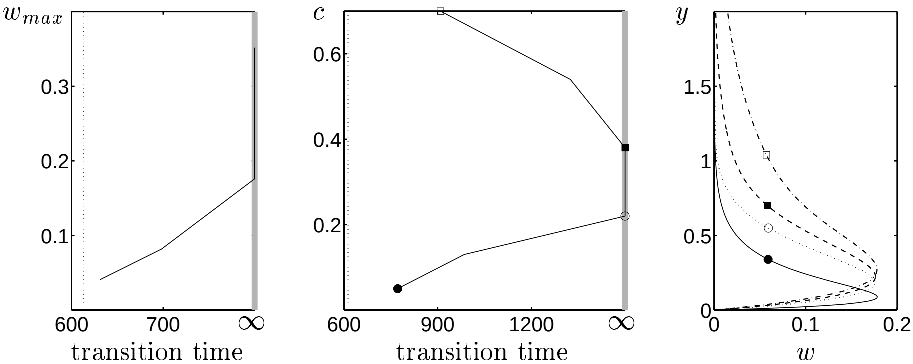

FIGURE 10. Left: transition time dependence on maximum spanwise flow for $\omega = 0.09$ and $c = 0.22$. Middle: transition time dependence on the wall normal distribution of the spanwise flow. Right: spanwise flow. The markers in the two rightmost figures connect the transition times with the corresponding spanwise flow.

slowly decreases, a behavior similar to that found for the spanwise flow caused by the body force.

5.2. Control of transition caused by random disturbances.

5.2.1. *Control by body force.* The transition scenario initiated by the random disturbances was easier controlled than oblique transition and both our strategies could actually prevent transition. For a body force with $\omega = 0.09$ and $c = 0.22$ a forcing amplitude of 0.043 was found sufficient to prevent transition. It corresponds to a maximum spanwise flow amplitude of 0.18 and is only one third of what gave optimal performance on the oblique waves. The transition time for different amplitudes are displayed in figure 10, where a curve reaching the right edge of the figure represents complete prevention of transition. The same spanwise flow amplitude was used for the study of how the wall normal flow distribution influence transition which is presented in the two rightmost frames of figure 10. The markers in the middle frame connect transition times and c-values with the flow profiles in the right frame. The same flow distributions that gave the longest transition delay of oblique transition was found to prevent transition caused by the random disturbance. Referring to the left frame it is possible to conclude that an increased forcing amplitude would prevent transition for a wider range of flow distributions.

The frequency range of the forcing which in figure 11 is found to prevent transition is slightly lower than that giving the longest transition delay of oblique transition, but they do overlap. The flow distributions used were the same as for oblique transition, displayed in figure 8. Variation of the transition time due to the precise turn on time of forcing was also noted for this transition scenario but the variation was not as regular as for oblique transition (cf. figure 8).

5.2.2. *Control by wall oscillations.* Oscillating the boundary layer wall was found to delay transition less than the oscillating spanwise force in a similar

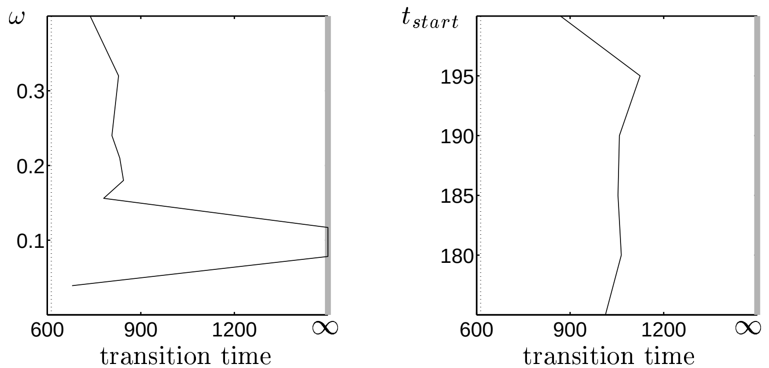

FIGURE 11. Left: transition time dependence on forcing frequency. Right: variation of transition delay due to changes of start instant.

manner as for transition caused by the oblique waves. However, as random disturbance transition was easier to control, it could be prevented by the oscillating wall if the wall speed was high enough. In figure 12 this is achieved for maximum wall speed 1.0, which is above the optimal wall speed of 0.6 found for oblique transition. The longest transition delay was found for ω just above 0.1 (middle frame), which is within the optimal frequency range observed for the body force. For oblique transition the optimal range of the wall oscillations was shifted towards lower frequencies, were the results were still rather poor. The large influence of the control turn on process that we found for the body force cases was large in this case and the transition time dependence on start instant is displayed in the left frames of figure 12. The jump in transition time is now found at a different time than it was for the body force, indicating that this effect is related to the control flow rather than to a suddenly appearing flow structure.

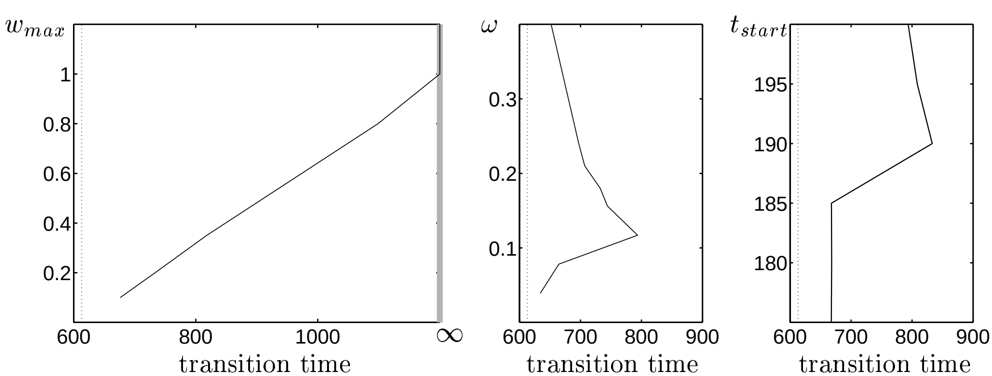

FIGURE 12. Transition time dependence on: maximum spanwise speed of the wall oscillating with $\omega = 0.09$ (left), oscillation frequency with $w_{max} = 0.35$ (middle) and oscillation start time (right), with $w_{max} = 0.35$ and $\omega = 0.117$.

6. Discussion and summary

We have shown that spanwise oscillations of a boundary layer flow may delay or even prevent transition caused by oblique waves or a random disturbance. Oblique transition was for the studied cases more difficult to delay, possibly because it contains larger more coherent structures that were less effected by the applied control. The oscillating flow caused by a body force exponentially decaying from the wall could delay transition further than a flow caused by a oscillating wall. The reason for this was that the oscillating flow caused by the body force reached further away from the wall where, essential structures could be affected. The optimal oscillation frequency observed was in the range $0.1 < \omega < 0.2$ for all the studied cases, with the exception that the oscillating wall gave comparable transition delay for lower frequencies when applied to oblique transition. That delay was however small. It is worth pointing out that results not presented here show that the body force was also more dangerous in the sense that unsuitably set control parameters could cause earlier transition.

The physical mechanisms causing the transition delay are uncertain. Large efforts were made to identify structures, wave, flow or vorticity components that correlated with transition time and the applied control, but no general pattern was found. Typically we find several cases were the transition delay correlate well with the reduction of the streak amplitude in oblique transition but also a few cases were transition is delayed and the streak amplitude enhanced. The same was true for other relations and our conclusion is that several components of the complicated nonlinear transition stage influence the transition time. Transition delay can be achieved by reducing one or two of them even if an other becomes stronger. An approach similar to that of Zang & Hussaini (1985) may be beneficial in rating the importance of different components. They artificially suppressed different wave components in calculations of transition caused by secondary instability of TS-waves.

In order to obtain results that could be compared to an experimental situation, spatial simulations are required and this study may be valuable for the initial parameter choices and interpretations of such calculations that are considerably more expensive. Moreover, spatial calculations will provide necessary information for the estimate of the efficiency of the suggested control.

We are grateful to Mr. Jaisig Choi for fruitful discussions and his interest in our study. This work has been supported by TFR (Swedish Research Council for Engineering Sciences).

References

Akhavan, R., Jung, W. J. & Mangliavacchi, N. 1993. Turbulence control in wall-bounded flows by spanwise oscillations. *Applied Scientific Research.* **51**, 299–303.

Berlin, S., Choi, J., Kim, J. & Henningson, D. S. 1996. Control of boundary layer transition. *Bull. Am. Phys. Soc.* **41**, 1750.

Berlin, S., Lundbladh, A. & Henningson, D. S. 1994. Spatial simulations of oblique transition. *Phys. Fluids.* **6**, 1949–1951.

Berlin, S., Wiegel, M. & Henningson, D. S. 1998. Numerical and experimental investigation of oblique boundary layer transition. Submitted to jfm.

BUTLER, K. M. & FARRELL, B. F. 1992. Three-dimensional optimal perturbations in viscous shear flow. *Phys. Fluids A.* **4**, 1637–1650.

CHOI, H., MOIN, P. & KIM, J. 1993. Active turbulence control for drag reduction in wall-bounded flows. *J. Fluid Mech.* **262**, 75.

DANABASOGLU, G., BIRINGEN, S. & L., S. C. 1991. Spatial simulation of instability by periodic suction blowing. *Phys. Fluids A.* **3** (9), 2138–2147.

ELOFSSON, P. A. & ALFREDSSON, P. H. 1997. An experimental investigation of oblique transition in a Blasius boundary layer. In *EUROMECH Colloquium 359.*

GAD-EL HAK, M. 1989. Flow control. *Appl. Mech. Rev.* **42** (10), 261–293.

GUSTAVSSON, L. H. 1991. Energy growth of three-dimensional disturbances in plane Poiseuille flow. *J. Fluid Mech.* **224**, 241–260.

KIM, J., LEE, C., BERGER, T., LIM, J. & CHOI, H. 1995. Effects of electro-magnetic force on near-wall turbulence. *Bull. Am. Phys. Soc.* **40**, 1989.

KIM, J., LEE, C., BERGER, T., LIM, J. & CHOI, H. 1996. Turbulence control using electro-magnetic forces. *Bull. Am. Phys. Soc.* **41**, 1719.

KLEISER, L. & LAURIEN, E., 1985. Numerical investigation of interactive transition control. AIAA Paper 85-0566.

LUNDBLADH, A., SCHMID, P. J., BERLIN, S. & HENNINGSON, D. S., 1994. Simulation of bypass transition in spatially evolving flows. Proceedings of the AGARD Symposium on Application of Direct and Large Eddy Simulation to Transition and Turbulence, AGARD-CP-551.

MALIK, M. R., ZANG, T. A. & HUSSAINI, M. Y. 1985. A spectral collocation method for the Navier-Stokes equations. *J. Comp. Phys.* **61**, 64–88.

NOSENCHUCK, D. M. & BROWN, G. 1993. Discrete spatial control of wall shear stress in a turbulent boundary layer. In *Near-Wall Turbulent Flows*, pp. 689–698. Elsevier Science Publishers B.V.

REDDY, S. C. & HENNINGSON, D. S. 1993. Energy growth in viscous channel flows. *J. Fluid Mech.* **252**, 209–238.

THOMAS, A. S. 1983. The control of boundary-layer transition using a wave superposition principle. *J. Fluid Mech.* **137**, 233–250.

TREFETHEN, L. N., TREFETHEN, A. E., REDDY, S. C. & DRISCOLL, T. A. 1993. Hydrodynamic stability without eigenvalues. *Science.* **261**, 578–584.

TSINOBER, A. 1989. Mhd flow drag reduction. In *Viscous Drag Reduction in Boundary Layers*, volume 123, pp. 327–349. Progress in Astronautics and Aeronautics, American Institute of Aeronotical and Astronautics, Inc.

WIEGEL, M. 1997. *Experimentelle Untersuchung von kontrolliert angeregten dreidimensionalen Wellen in einer Blasius-Grenzschicht.*, volume 312 of *VDI Fortschritt-Bericht Reihe 7.* VDI-Verlag, Düsseldorf (Germany). Dissertation zum Dr.-Ing. an der TH Hannover, Dezember 1996.

ZANG, T. A. & HUSSAINI, M. Y., 1985. Numerical experiments on subcritical transition mechanism. AIAA Paper 85-0296.

Paper 6

P6

AN EFFICIENT SPECTRAL METHOD FOR SIMULATION OF INCOMPRESSIBLE FLOW OVER A FLAT PLATE

A. Lundbladh
VOLVO Aero Corporation, 461 81 Trollhättan, Sweden
S. Berlin
Dept. of Mech., KTH, S-10044 Stockholm, Sweden
D. S. Henningson
FFA, Box 11021, S-16111 Bromma, Sweden

Abstract. An efficient spectral integration technique for the solution of the Navier-Stokes equations for incompressible flow over a flat plate is described. The algorithm can either be used for temporal or spatial simulation. In the latter case, a fringe region technique is used to allow a streamwise inflow and outflow of the computational domain. At a constant distance from the flat plate an artificial boundary is introduced and a free-stream boundary condition applied. The horizontal directions are discretized using Fourier series and the normal direction using Chebyshev series. Time integration is performed using second order Adams-Bashforth or third order Runge-Kutta method for the advective and forcing terms and Crank-Nicholson for the viscous terms.

1. Introduction

This is the first part of a complete report on the boundary layer code `bla` (Lundbladh, Berlin, Skote, Hildings, Choi, Kim & Henningson 1998). The full report contains detailed descriptions of implementation issues and an evaluation of the fringe method, in addition to the generic numerical method described here.

Solution of the Navier-Stokes equations for the simulation of transition and turbulence requires high numerical accuracy for a large span of length scales. This has prompted a development of accurate spectral methods. Unfortunately even with these methods computations require an immense amount of computer time and memory. In the present report we use spectral integration methods to derive an accurate algorithm of the flat plate boundary flow geometry. The basic numerical method is similar to the Fourier-Chebyshev method used by Kim, Moin & Moser (1987).

The original algorithm (Lundbladh, Henningson & Johanson 1992) solved the incompressible flow equations in a channel flow geometry. To allow simulations of the flow over a flat plate a free-stream boundary condition is required, and for spatial simulations a fringe region technique similar to that of Bertolotti, Herbert & Spalart (1992) is described.

For further details about spectral discretizations and additional references see Canuto, Hussaini, Quarteroni & Zang (1988).

The original channel code and the implementation of the present numerical method has been used in a number of investigations.

In channel flow:

Henningson, Johansson & Lundbladh (1990), Lu & Henningson (1990), Lundbladh & Johansson (1991), Schmid & Henningson (1992), Lundbladh (1993), Henningson, Lundbladh & Johansson (1993), Lundbladh & Henningson (1993), Schmid & Henningson (1993), Elofsson & Lundbladh (1994), Kreiss, Lundbladh & Henningson (1994), Lundbladh, Henningson & Reddy (1994), Schmid, Lundbladh & Henningson (1994), Henningson (1995), Reddy, Schmid, Baggett & Henningson (1998).

In boundary layer flow:

Lundbladh, Johansson & Henningson (1992), Berlin, Lundbladh & Henningson (1994), Henningson & Lundbladh (1994), Lundbladh, Schmid, Berlin & Henningson (1994), Lundbladh & Henningson (1995), Högberg & Henningson (1998), Schmid, Reddy & Henningson (1996), Nordström, Nordin & Henningson (1997), Hildings (1997), Berlin & Henningson (1998), Berlin, Hanifi & Henningson (1998), Berlin, Wiegel & Henningson (1998), Berlin, Kim & Henningson (1998), Bech, Henningson & Henkes (1998).

2. The numerical method

2.1. Derivation of the velocity-vorticity formulation. The starting point is the non-dimensionalized incompressible Navier-Stokes equations in a rotating reference frame, here written in tensor notation,

$$\frac{\partial u_i}{\partial t} = -\frac{\partial p}{\partial x_i} + \epsilon_{ijk} u_j (\omega_k + 2\Omega_k) - \frac{\partial}{\partial x_i}(\frac{1}{2} u_j u_j) + \frac{1}{R}\nabla^2 u_i + F_i, \tag{1}$$

$$\frac{\partial u_i}{\partial x_i} = 0, \tag{2}$$

with boundary conditions at the flat plate and at the free-stream boundary, which are discussed in the next subsections.

The first equation represents conservation of momentum and the second equation incompressibility of the fluid. Here $(x_1, x_2, x_3) = (x, y, z)$ are the streamwise, normal and spanwise coordinates, $(u_1, u_2, u_3) = (u, v, w)$ are the respective velocities, $(\omega_1, \omega_2, \omega_3) = (\chi, \omega, \vartheta)$ are the corresponding vorticities, and p is the pressure. The streamwise and spanwise directions will alternatively be termed horizontal directions. Ω_k is the angular velocity of the coordinate frame around axis k. In practise the most often used case is rotation around the spanwise axis, thus let $\Omega = \Omega_3$ be the rotation number. F_i is a body force which is used for numerical purposes that will be further discussed below. It can also be used to introduce disturbances in the flow. The Reynolds number is defined as $R = U_\infty \delta^* / \nu$, where U_∞ is the undisturbed streamwise free-stream velocity at $x = 0$ and $t = 0$, δ^* is the displacement thickness of the undisturbed streamwise velocity at $x = 0$ and $t = 0$, and ν is the kinematic viscosity. The size of the solution domain in physical space is x_L, y_L and z_l in the streamwise, normal and spanwise directions, respectively.

A Poisson equation for the pressure can be obtained by taking the divergence of the momentum equation,

$$\nabla^2 p = \frac{\partial H_i}{\partial x_i} - \nabla^2(\frac{1}{2}u_j u_j) \tag{3}$$

where $H_i = \epsilon_{ijk} u_j(\omega_k + 2\Omega_k) + F_i$. Application of the Laplace operator to the momentum equation for the normal velocity yields an equation for that component through the use of Eqs. (3) and (2). One finds

$$\frac{\partial \nabla^2 v}{\partial t} = \left(\frac{\partial^2}{\partial x^2} + \frac{\partial^2}{\partial z^2}\right) H_2 - \frac{\partial}{\partial y}(\frac{H_1}{\partial x} + \frac{\partial H_3}{\partial z}) + \frac{1}{R}\nabla^4 v. \tag{4}$$

This equation can, for numerical purposes, be written as a system of two second order equations:

$$\begin{aligned} \frac{\partial \phi}{\partial t} &= h_v + \frac{1}{R}\nabla^2 \phi \\ \nabla^2 v &= \phi, \end{aligned} \tag{5}$$

where

$$h_v = \left(\frac{\partial^2}{\partial x^2} + \frac{\partial^2}{\partial z^2}\right) H_2 - \frac{\partial}{\partial y}\left(\frac{\partial H_1}{\partial x} + \frac{\partial H_3}{\partial z}\right). \tag{6}$$

An equation for the normal vorticity can be found by taking the curl of the momentum equation. The second component of that equation read

$$\frac{\partial \omega}{\partial t} = h_\omega + \frac{1}{R}\nabla^2 \omega, \tag{7}$$

where

$$h_\omega = \frac{\partial H_1}{\partial z} - \frac{\partial H_3}{\partial x}. \tag{8}$$

Note that the equations for ϕ, v and ω have similar form, and can thus be solved using the same numerical routine. Once the the normal velocity v and the normal vorticity ω have been calculated the other velocity components can be found form the incompressibility constraint and the definition of the normal vorticity.

2.2. Boundary condition. The boundary conditions in the horizontal directions are periodic but we need to specify boundary conditions at the plate and in the free-stream, to solve equations (5) and (7). The natural no-slip boundary conditions read

$$v(y=0) = 0, \; \frac{\partial v(y=0)}{\partial y} = 0, \; \omega(y=0) = 0. \tag{9}$$

For disturbance generation and control by blowing and suction through the plate an arbitrary time dependent velocity distribution

$$v(y=0) = v_{BS}(x,z,t) \tag{10}$$

can be used.

The flow is assumed to extend to an infinite distance perpendicularly to the flat plate. However, the discretization discussed below can only handle a finite domain. Therefore, the flow domain is truncated and an artificial boundary condition is applied in the free-stream.

The simplest possible is a Dirichlet condition i.e.,

$$u_i(y=y_L) = \mathcal{U}_i(y=y_L) \tag{11}$$

Where $\mathcal{U}_i(x,y,z,t)$ is a base flow that is normally chosen as a Falkner-Skan-Cook flow. An arbitrary pressure gradient, to for instance create a separation bubble, can be imposed by choosing $\mathcal{U}_i$ accordingly.

The desired flow solution generally contains a disturbance and that will be forced to zero by the Dirichlet condition. This introduces an error compared to the exact solution for which the boundary condition is applied at an infinite distance from the wall. The error may result in increased damping for disturbances in the boundary layer.

Some improvement can be achieved by using a Neumann condition,

$$\frac{\partial u_i}{\partial y}|_{y=y_L} = \frac{\partial \mathcal{U}_i}{\partial y}|_{y=y_L}. \tag{12}$$

This condition can be shown to be stable if there is outflow at the boundary or the inflow is weaker than $O(1/R)$. This restriction is fulfilled if the base flow is away from the wall and the boundary is placed on a sufficiently large distance from the wall, so that the disturbance velocity is small.

A generalization of the boundary condition used by Malik, Zang & Hussaini (1985) allows the boundary to be placed closer to the wall. It is an asymptotic condition that decreases the error further and it reads

$$\left[\frac{\partial \hat{u}_i}{\partial y} + |k|\hat{u}_i\right]_{y=y_L} = \left[\frac{\partial \hat{\mathcal{U}}_i}{\partial y} + |k|\hat{\mathcal{U}}_i\right]_{y=y_L} \tag{13}$$

where ˆ denotes the horizontal Fourier transform with respect to the horizontal coordinates, $k^2 = \alpha^2 + \beta^2$ and α and β are the horizontal wavenumbers (see equation 28). Thus this condition is most easily applied in Fourier space. The boundary condition exactly represents a potential flow solution decaying away from the wall. It is essentially equivalent to requiring that the vorticity is zero at the boundary. Thus it can be applied immediately outside the vortical part of the flow.

2.3. Forcing for temporal simulation. A localized disturbance or wave of relatively short wavelength which travels downstream in a slowly growing boundary layer is surrounded by a boundary layer of almost constant thickness which grows slowly in time. This forms the basis of the temporal simulation technique.

Following the ideas of Spalart & Yang (1987) we assume that the boundary layer streamwise velocity is $U(x,y)$ and introduce a reference point $x_r = x_0 + ct$ where c is a reference speed. We now assume that the undisturbed boundary layer in the vicinity of the disturbance has the velocity distribution $U(y,t) = U(x_r, y)$, $V(y,t) = 0$. Since the boundary layer is now parallel (as there is no dependence on x), it is possible to apply periodic boundary conditions in the horizontal directions. However, whereas $U(x,y)$ (with the corresponding V given by continuity) is a solution to Navier-Stokes or at least the boundary layer equations, this is not true for $\{U(y,t), V(y,t)\}$. Thus to ensure the correct development of the boundary layer profile over extended periods of time it is necessary to add a (weak) forcing to balance the streamwise momentum equation,

$$F_1 = \frac{\partial U(y,t)}{\partial t} - \frac{1}{R}\frac{\partial^2 U(y,t)}{\partial y^2} = c\frac{\partial U(x,y)}{\partial x} - \frac{1}{R}\frac{\partial^2 U(x,y)}{\partial y^2} \tag{14}$$

where the right hand side should be evaluated at the reference coordinate x_r. The reference speed should be chosen as the group speed of the wave or the propagation speed of the localized disturbance for best agreement with a spatially developing flow. To fully justify the periodic boundary conditions in the case of a wave train, the wave itself should be slowly developing.

2.4. Forcing for spatial simulation. The best numerical model of a physical boundary layer, which is usually developing in the downstream direction rather than in time, is a spatial formulation. To retain periodic boundary conditions, which is necessary for the Fourier discretization described below, a fringe region is added downstream of the physical domain, similar to that described by Bertolotti, Herbert & Spalart (1992). In the fringe region disturbances are damped and the flow returned to the desired inflow condition. This is accomplished by the addition of a volume force which only increases the execution time of the algorithm by a few percent.

The form of the forcing is :

$$F_i = \lambda(x)(\mathcal{U}_i - u_i) \tag{15}$$

where $\lambda(x)$ is a non-negative fringe function which is significantly non-zero only within the fringe region. $\mathcal{U}_i$ is the same flow field used for the boundary conditions, which also contains the desired flow solution in the fringe. The streamwise velocity component is calculated as,

$$\mathcal{U}_x(x,y) = U(x,y) + [U(x+x_L, y) - U(x,y)]\, S\left(\frac{x - x_{mix}}{\Delta_{mix}}\right), \tag{16}$$

where $U(x,y)$ is normally a solution to the boundary layer equations. Here x_{mix} and Δ_{mix} are chosen so that the prescribed flow, within the fringe region, smoothly changes from the outflow velocity of the physical domain to the desired inflow velocity. S is given below. The wall normal component $\mathcal{U}_y$ is then calculated from the equation of continuity, and the spanwise velocity $\mathcal{U}_z$ is set to zero for simulations where the mean flow is two dimensional. For three dimensional boundary layers $\mathcal{U}_z$ is computed from a boundary layer solution in fashion analogous to that for $\mathcal{U}_x$. This choice of $\mathcal{U}$ ensures that for the undisturbed laminar boundary layer the decrease in thickness is completely confined to the fringe region, thus minimizing the upstream influence. A forced disturbance to the laminar flow can be given as inflow condition if that disturbance is included in $\mathcal{U}_i$.

A convenient form of the fringe function λ is as follows

$$\lambda(x) = \lambda_{max}[S(\frac{x - x_{start}}{\Delta_{rise}}) - S(\frac{x - x_{end}}{\Delta_{fall}} + 1)]$$

Here λ_{max} is the maximum strength of the damping, x_{start} to x_{end} the spatial extent of the region where the damping function is nonzero and Δ_{rise} and Δ_{fall} the rise and fall distance of the damping function. $S(x)$ is a smooth step function rising from zero for negative x to one for $x \geq 1$. We have used the following form for S, which has the advantage of having continuous derivatives of all orders.

$$S(x) = \begin{cases} 0 & x \leq 0 \\ 1/[1 + \exp(\frac{1}{x-1} + \frac{1}{x})] & 0 < x < 1 \\ 1 & x \geq 1 \end{cases}$$

To achieve maximum damping both the total length of the fringe and λ_{max} has to be tuned. The actual shape of $\lambda(x)$ is less important for the damping but it should have its maximum closer to x_{end} than to x_{start}. The damping is also strongly effected by the resolution of the disturbance that should be damped. An investigation of how the fringe parameters effect the disturbance in the fringe can be found in Hildings (1997).

For maximum computational efficiency the simulated flow has to be considered when the fringe parameters are tuned. Assuming that the achieved damping is sufficient, a short fringe reduces the box length and therefor the required CPU time per iteration. However, if the flow gradients introduced in the fringe region are larger than those in the physical domain that may decrease the time step and consequently the necessary number of iterations. Note that the boundary layer growth causes outflow through the free-steam boundary. The streamwise periodicity requires that all that fluid enters in the fringe region.

Analysis of Navier-Stokes equations with a fringe forcing term yields that there is an additional part of the disturbance associated with the pressure whose decay is not dependent on λ. For a boundary layer, this solution decays appreciably over a downstream distance equal to the boundary layer thickness, and thus the fringe region must be some factor (say 10 to 30) times this thickness to get a large decay factor, see Nordström, Nordin & Henningson 1997.

2.5. Temporal discretization. The time advancement is carried out by one of four semi-implicit schemes. We illustrate them on the equation

	$a_n/\Delta t^n$	$b_n/\Delta t^n$	$c_n/\Delta t^n$
Euler	1	0	0
AB2	$1 + \Delta t^n/2\Delta t^{n-1}$	$-\Delta t^n/2\Delta t^{n-1}$	1/2
RK3	8/15	0	0
3-stage	5/12	-17/60	8/15
	3/4	-5/12	2/3
RK3	8/17	0	0
4-stage	17/60	-15/68	8/17
	5/12	-17/60	8/15
	3/4	-5/12	2/3

TABLE 1. Time-stepping coefficients.

$$\frac{\partial \psi}{\partial t} = G + L\psi, \tag{17}$$

which is on the same form as equation (5) and (7). ψ represents ϕ or ω, G contains the (nonlinear) advective, rotation and forcing terms and depends on all velocity and vorticity components, L is the (linear) diffusion operator. L is discretized implicitly using the second order accurate Crank-Nicholson (CN) scheme and G explicitly by either the second order Adams-Bashforth (AB2) or a low storage third order three or four stage Runge-Kutta (RK3) scheme. These time discretizations may be written in the following manner : (G and L are assumed to have no explicit dependence on time)

$$\psi^{n+1} = \psi^n + a_n G^n + b_n G^{n-1} + (a_n + b_n)\left(\frac{L\psi^{n+1} + L\psi^n}{2}\right), \tag{18}$$

where the constants a_n and b_n are chosen according to the explicit scheme used. Four possibilities are shown in the Table 1. The first is forward Euler which is used as a start up for the Adams-Bashforth scheme, the second is the AB2 scheme (allowing for variable time steps) and the third and fourth are the RK3 schemes. Note that the RK3 schemes have three or four stages which implies that a full physical time step is only achieved every three or four iterations. The time used for the intermediate stages are given by $t = t + c_n$, where c_n is given in table 1.

To obtain some insight into the properties of these they will be applied to the two dimensional linearized Burgers' equation with a system rotation. The eigenvalue analysis yields a necessary condition for stability which must be augmented by an experimental verification. Putting the equation into the form of Eq. (17) yields :

$$
\begin{aligned}
\psi &= \begin{bmatrix} u \\ w \end{bmatrix} \\
G &= \begin{bmatrix} u_0\partial/\partial x + w_0\partial/\partial z & 2\Omega \\ -2\Omega & u_0\partial/\partial x + w_0\partial/\partial z \end{bmatrix} \begin{bmatrix} u \\ w \end{bmatrix} \\
L &= \frac{1}{R}\begin{bmatrix} \partial^2/\partial x^2 + \partial^2/\partial z^2 & 0 \\ 0 & \partial^2/\partial x^2 + \partial^2/\partial z^2 \end{bmatrix}
\end{aligned} \tag{19}
$$

It can be seen as an approximation to Eq. (1). The dependence of ψ on both the streamwise and spanwise coordinate directions have been included in order to indicate how multiple dimensions enter into the stability considerations.

We will for simplicity use Fourier discretization in the spatial directions. The Chebyshev method acts locally as a transformed Fourier method and thus the stability properties derived here can be applied with the local space step. An exception to this occurs at the endpoints where the transformation is singular. It can be shown that the Chebyshev method is more stable there. A numerical study of a 1-dimensional advection equation using the Chebyshev discretization yields that the upper limit of its spectrum along the imaginary axis is about 16 times lower than the simple application of the results from the Fourier method. This allows a corresponding increase of the time-step when the stability is limited by the wall normal velocity at the free-stream boundary.

Fourier transforming in x and z yields:

$$
\hat{\psi}_t = \begin{bmatrix} i\alpha u_0 + i\beta w_0 & 2\Omega \\ -2\Omega & i\alpha u_0 + i\beta w_0 \end{bmatrix} \hat{\psi} - \frac{\alpha^2+\beta^2}{R}\hat{\psi}, \tag{20}
$$

where α and β are the wavenumbers in the x and z directions, respectively. This equation can be diagonalized to yield the equation,

$$
\hat{u}_t = i(\alpha u_0 + \beta w_0 \pm 2\Omega)\hat{u} + \frac{\alpha^2+\beta^2}{R}\hat{u} \tag{21}
$$

We assume that the absolute stability limit will first be reached for the largest wavenumbers of the discretization α_{max} and β_{max}, which corresponds to a wavelength of $2 \cdot \Delta x$ and Δz, respectively. Δx Δz are the discretization step lengths in physical space. The following parameters are useful for our analysis,

$$
\begin{aligned}
\mu &= \Delta t[2|\Omega_k| + (\alpha_{max}|u_0| + \beta_{max}|w_0|)] \\
&= \Delta t\left[2|\Omega_k| + \pi\left(\frac{|u_0|}{\Delta x} + \frac{|w_0|}{\Delta z}\right)\right],
\end{aligned} \tag{22}
$$

$$
\begin{aligned}
\lambda &= \frac{1}{R}\Delta t(\alpha_{max}^2 + \beta_{max}^2) \\
&= \frac{1}{R}\pi^2\Delta t\left(\frac{1}{\Delta x^2} + \frac{1}{\Delta z^2}\right).
\end{aligned} \tag{23}
$$

The parameter μ is usually called the spectral CFL number, in analogy with the stability theory for finite difference equations. Henceforth it will be termed

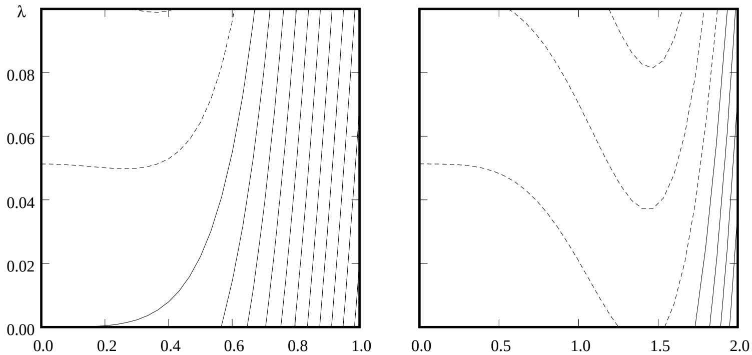

FIGURE 1. Contours of constant amplification factor for a) the AB2-CN method, and b) the RK3-CN method. Contour spacing is 0.05 with dashed lines indicating that the amplification factor is below unity.

simply the CFL number. Using the AB2-CN with a constant time-step we have the following time discretization for the model equation (21),

$$\hat{u}^{n+1} = \hat{u}^n + i\mu\left(\frac{3}{2}\hat{u}^n - \frac{1}{2}\hat{u}^{n-1}\right) - \frac{\lambda}{2}(\hat{u}^{n+1} + \hat{u}^n) \tag{24}$$

and using the RK3-CN time discretization we have the following three stages in each time step

$$\begin{aligned}
\hat{u}^{n+1} &= \hat{u}^n + i\mu a_1\hat{u}^n - \frac{\lambda}{2}a_1(\hat{u}^{n+1} + \hat{u}^n),\\
\hat{u}^{n+2} &= \hat{u}^{n+1} + i\mu(a_2\hat{u}^{n+1} + b_2\hat{u}^n) - \frac{\lambda}{2}(a_2 + b_2)(\hat{u}^{n+2} + \hat{u}^{n+1}),\\
\hat{u}^{n+3} &= \hat{u}^{n+2} + i\mu(a_3\hat{u}^{n+2} + b_3\hat{u}^{n+1}) - \frac{\lambda}{2}(a_3 + b_3)(\hat{u}^{n+3} + \hat{u}^{n+2}).
\end{aligned} \tag{25}$$

The absolute stability regions, i.e. the regions where all solutions to the above difference equations are bounded in the $\mu - \lambda$ plane, can now be found by calculating the roots of the associated characteristic polynomials. Contours of constant absolute values of the roots are given in figure 1. Figure 1a shows the curves for the AB2-CN method whereas figure 1b shows the curves for the RK3-CN method. Note that higher values of λ (lower Reynolds number) stabilizes the method, i.e. increases the CFL number (μ) that is allowed for an absolutely stable solution. In the limit of infinite Reynolds number the AB2-CN method is not absolutely stable for any CFL number, whereas the RK3-CN method approaches the limit $\sqrt{3}$, a result which also can be arrived at through the standard analysis of the RK3 scheme alone. The analysis for the four stage method is analogous and the stability limit is $\sqrt{8}$.

If the time advancement scheme (18) is applied to Eqs. (5) and (7) we find (for the moment disregarding the boundary conditions),

$$\begin{aligned}(1-\frac{a_n+b_n}{2R}\nabla^2)\phi^{n+1} &= (1+\frac{a_n+b_n}{2R}\nabla^2)\phi^n + a_n h_v^n + b_n h_v^{n-1} \\ \nabla^2 v^{n+1} &= \phi^{n+1}\end{aligned} \tag{26}$$

and

$$(1-\frac{a_n+b_n}{2R}\nabla^2)\omega^{n+1} = (1+\frac{a_n+b_n}{2R}\nabla^2)\omega^n + a_n h_\omega^n + b_n h_\omega^{n-1} \tag{27}$$

2.6. Horizontal discretization – Fourier expansions. The discretization in the horizontal directions uses a Fourier series expansions which assumes that the solution is periodic.

The streamwise and spanwise dependence of each variable can then be written

$$u(x,z) = \sum_{l=-(\frac{N_x}{2}-1)}^{\frac{N_x}{2}-1} \sum_{m=-(\frac{N_z}{2}-1)}^{\frac{N_z}{2}-1} \hat{u}(\alpha,\beta)\exp[i(\alpha_l x + \beta_m z)] \tag{28}$$

where $\alpha_l = 2\pi l/x_L$ and $\beta_m = 2\pi m/z_L$, and N_x and N_z are the number of Fourier modes included in the respective directions. Note that the indices on the discrete wavenumbers α and β are sometimes left out for notational convenience and that $k^2 = \alpha^2 + \beta^2$.

2.6.1. *Normal velocity and normal vorticity equations.* Expanding the dependent variables of Eq. (26) in Fourier series gives

$$\begin{aligned}\left(1-\frac{a_n+b_n}{2R}(D^2-k^2)\right)\hat{\phi}^{n+1} &= \left(1+\frac{a_n+b_n}{2R}(D^2-k^2)\right)\hat{\phi}^n + a_n\hat{h}_v^n + b_n\hat{h}_v^{n-1} \\ (D^2-k^2)\hat{v}^{n+1} &= \hat{\phi}^{n+1}\end{aligned} \tag{29}$$

where D signifies a derivative in the normal direction. Note that the above equations are two linear constant coefficient second order ordinary differential equations in y. A similar equation can also be derived from Eq. (27) . These three equations can be written as follows

$$(D^2-\lambda^2)\hat{\phi}^{n+1} = \hat{f}_v^n \tag{30}$$

$$(D^2-k^2)\hat{v}^{n+1} = \hat{\phi}^{n+1} \tag{31}$$

$$(D^2-\lambda^2)\hat{\omega}^{n+1} = \hat{f}_\omega^n \tag{32}$$

where

$$\lambda^2 = k^2 + 2R/(a_n+b_n) \tag{33}$$

$$\hat{f}_v^n = \hat{p}_v^n - \frac{2Ra_n}{a_n+b_n}\hat{h}_v^n \tag{34}$$

$$\hat{f}_\omega^n = \hat{p}_\omega^n - \frac{2Ra_n}{a_n+b_n}\hat{h}_\omega^n \tag{35}$$

and

$$
\begin{aligned}
\hat{p}_v^n &= -\left[D^2-\lambda^2+\frac{4R}{a_n+b_n}\right]\hat{\phi}^n-\frac{2Rb_n}{a_n+b_n}\hat{h}_v^{n-1} \\
&= -\hat{f}_v^{n-1}-\frac{4R}{a_n+b_n}\hat{\phi}^n-\frac{2Rb_n}{a_n+b_n}\hat{h}_v^{n-1}, \qquad (36)\\
\hat{p}_\omega^n &= -\left[D^2-\lambda^2+\frac{4R}{a_n+b_n}\right]\hat{\omega}^n-\frac{2Rb_n}{a_n+b_n}\hat{h}_\omega^{n-1} \\
&= -\hat{f}_\omega^{n-1}-\frac{4R}{a_n+b_n}\hat{\omega}^n-\frac{2Rb_n}{a_n+b_n}\hat{h}_\omega^{n-1}, \qquad (37)
\end{aligned}
$$

We will denote the quantities $\hat{p}_\omega^n$ and $\hat{p}_v^n$ the partial right hand sides of the equations.

2.6.2. *Horizontal velocities and wavenumber zero.* Having obtained $\hat{v}$ and $\hat{\omega}$ we can find $\hat{u}$ and $\hat{w}$ using Eq. (2) and the definition of the normal vorticity component, both transformed to Fourier space. We find

$$\hat{u} = \frac{i}{k^2}(\alpha D\hat{v}-\beta\hat{\omega}), \qquad (38)$$

$$\hat{w} = \frac{i}{k^2}(\alpha\hat{\omega}+\beta D\hat{v}). \qquad (39)$$

Similarly, we can find the streamwise and spanwise component of vorticity in terms of $\hat{\omega}$ and $\hat{\phi}$,

$$\hat{\chi} = \frac{i}{k^2}(\alpha D\hat{\omega}+\beta\hat{\phi}), \qquad (40)$$

$$\hat{\vartheta} = \frac{-i}{k^2}(\alpha\hat{\phi}+\beta D\hat{\omega}). \qquad (41)$$

These relations give the streamwise and spanwise components of velocity and vorticity for all wavenumber combinations, except when both α and β are equal to zero. In that case we have to use some other method to find $\hat{u}_0$, $\hat{w}_0$, $\hat{\chi}_0$ and $\hat{\vartheta}_0$ (the zero subscript indicates that $k=0$). The appropriate equations are found by taking the horizontal average of the first and the third component of Eq. (1). Due to the periodic BC all horizontal space derivatives cancel out, i.e.,

$$\frac{\partial u_0}{\partial t} = H_1+\frac{1}{R}\frac{\partial^2 u_0}{\partial y^2}, \qquad (42)$$

$$\frac{\partial w_0}{\partial t} = H_3+\frac{1}{R}\frac{\partial^2 w_0}{\partial y^2} \qquad (43)$$

After a time discretization we find,

$$(D^2-\lambda^2)\hat{u}_0^{n+1} = \hat{f}_{01}^n \qquad (44)$$

$$(D^2-\lambda^2)\hat{w}_0^{n+1} = \hat{f}_{03}^n \qquad (45)$$

where

$$\hat{f}^n_{0i} = \hat{p}^n_{0i} - \frac{2Ra_n}{a_n + b_n}\hat{H}^n_{0i}, \tag{46}$$

and

$$\begin{aligned} \hat{p}^n_{0i} &= -\left(D^2 - \lambda^2 + \frac{4R}{a_n + b_n}\right)\hat{u}^n_{0i} - \frac{2Rb_n}{a_n + b_n}\hat{H}^{n-1}_{0i}, \\ &= -\hat{f}^{n-1}_{0i}(\psi_0) - \frac{4R}{a_n + b_n}\hat{u}^n_{0i} - \frac{2Rb_n}{a_n + b_n}\hat{H}^{n-1}_{0i}. \end{aligned} \tag{47}$$

Here the 0 index in $\hat{H}_{0i}$ refers to the zero wavenumber in both horizontal directions. Note that the above system contains the same type of equations as the system (31), and can thus be solved using the same numerical algorithm. Once $\hat{u}_0$ and $\hat{w}_0$ are calculated, the streamwise and spanwise components of vorticity for $k = 0$ can be found as follows

$$\hat{\chi}_0 = D\hat{w}_0, \qquad \hat{\vartheta}_0 = -D\hat{u}_0. \tag{48}$$

2.6.3. *Solution procedure with boundary conditions.* A problem with the above equations is that the boundary conditions do not apply to the quantities for which we have differential equations. To remedy this, each of the equations can be solved for a particular solution with homogeneous boundary conditions. Then a number of homogeneous solutions with non-homogeneous boundary conditions are found for the same equations. Finally the boundary conditions are fulfilled by a suitable linear combination of particular and homogeneous solution. Explicitly we proceed as follows:

For all $k = \sqrt{\alpha^2 + \beta^2} \neq 0$ and each of the two symmetries (symmetric and antisymmetric with respect to reflections around $y = y_L/2$) we solve :

$$\begin{array}{llll}
(49) & (D^2 - \lambda^2)\hat{\phi}^{n+1}_p = \hat{f}^{n+1}_v & & \hat{\phi}^{n+1}_p(y_L) = 0 \\
(50) & (D^2 - k^2)\hat{v}^{n+1}_p = \hat{\phi}^{n+1}_p & & \hat{v}^{n+1}_p(y_L) = \begin{cases} \frac{v_{BS}}{2} & \textit{symetric} \\ \frac{-v_{BS}}{2} & \textit{antisymetric} \end{cases} \\
(51) & (D^2 - \lambda^2)\hat{\phi}^{n+1}_h = 0 & & \hat{\phi}^{n+1}_h(y_L) = 1 \\
(52) & (D^2 - k^2)\hat{v}^{n+1}_{ha} = \hat{\phi}^{n+1}_h & & \hat{v}^{n+1}_{ha}(y_L) = 0 \\
(53) & (D^2 - k^2)\hat{v}^{n+1}_{hb} = 0 & & \hat{v}^{n+1}_{hb}(y_L) = 1 \\
(54) & (D^2 - \lambda^2)\hat{\omega}^{n+1}_p = \hat{f}^{n+1}_\omega & & \hat{\omega}^{n+1}(y_L) = 0 \\
(55) & (D^2 - \lambda^2)\hat{\omega}^{n+1}_h = 0 & & \hat{\omega}^{n+1}(y_L) = 1
\end{array}$$

where the subscripts p, h, ha and hb indicate the particular and the homogeneous parts. v_{BS} is only nonzero for cases with blowing and suction through the plate. Note that only one boundary condition is needed for each second order equation since the assumption of symmetry (or antisymmetry) takes care of the other. $\hat{v}^{n+1}_p(y_L) = 0$ when the symmetric and antisymmetric solutions are added and all the other solutions are zero at $y = 0$. Equations (51) and

(55) have zero right hand sides and the same boundary conditions. The solution coefficients are therefore identical and so are their symmetric and antisymmetric coefficients. Thus, four calls of the the equation solver can be reduced to one.

To fulfill the the remaining boundary conditions we first construct $\hat{v}_{p1}$, $\hat{v}_{h1}$ and $\hat{v}_{h2}$,

$$\hat{v}_{p1}^{n+1} = \hat{v}_{p}^{n+1} + C_{p1}\hat{v}_{ha}^{n+1} \quad \hat{v}_{p1}^{n+1}(y_L) = 0 \quad \hat{v}_{p1}^{n+1}(0) = v_{BS}/2 \tag{56}$$

$$\hat{v}_{h1}^{n+1} = \hat{v}_{ha}^{n+1} / \frac{\partial \hat{v}_{ha}}{\partial y}(y = y_L) \quad \hat{v}_{h1}^{n+1}(y_L) = 0 \quad \hat{v}_{h1}^{n+1}(0) = 0 \tag{57}$$

$$\hat{v}_{h2}^{n+1} = \hat{v}_{hb}^{n+1} + C_{h2}\hat{v}_{ha}^{n+1} \quad \hat{v}_{h2}^{n+1}(y_L) = 1 \quad \hat{v}_{h2}^{n+1}(0) = 0 \tag{58}$$

where C_{p1} and C_{h2} are chosen to fulfill the boundary condition $\partial v/\partial y = 0$ at the lower wall for each of the two symmetries of $\hat{v}_{p1}$ and $\hat{v}_{h2}$. As the symmetric and antisymmetric parts of $\partial \hat{v}_{h1}/\partial y$ cancel at the lower wall their sum v_{h1} fulfills $\partial v_{h1}/\partial y = 0$.

Now the solutions (v_{p1}, ω_p), $(v_{h1}, \omega = 0)$, $(v_{h2}, \omega = 0)$ and $(v = 0, \omega_h)$ fulfill all the physical boundary conditions at the lower wall. The total normal velocity and vorticity is then given by

$$\hat{v}^{n+1} = \hat{v}_{p1}^{n+1} + C_{v1}\hat{v}_{h1}^{n+1} + C_{v2}\hat{v}_{h2}^{n+1} \tag{59}$$

$$\hat{\omega}^{n+1} = \hat{\omega}_{p}^{n+1} + C_{\omega}\hat{\omega}_{h}^{n+1} \tag{60}$$

where C_{v1},C_{v2} and C_ω are chosen such that the boundary conditions at the upper boundary are fulfilled. The u and w velocities are found from the definition of the normal vorticity and the incompressibility constraint.

In general we have to find u and w first to evaluate the boundary conditions. Thus with the C's unknown we find :

$$\hat{u}^{n+1} = \hat{u}_{p1}^{n+1} + C_{v1}\hat{u}_{h1}^{n+1} + C_{v2}\hat{u}_{h2}^{n+1} + C_{\omega}\hat{u}_{h}^{n+1} \tag{61}$$

$$\hat{w}^{n+1} = \hat{w}_{p1}^{n+1} + C_{v1}\hat{w}_{h1}^{n+1} + C_{v2}\hat{w}_{h2}^{n+1} + C_{\omega}\hat{w}_{h}^{n+1} \tag{62}$$

Where (u_{p1}, w_{p1}), (u_{h1}, w_{h1}), (u_{h2}, w_{h2}) and (u_h, w_h) are found from (v_{p1}, ω_p), $(v_{h1}, \omega = 0)$, $(v_{h2}, \omega = 0)$ and $(v = 0, \omega_h)$ using equation (38) and (39).

Assuming the boundary conditions are linear we can write them as :

$$L_i(\hat{u}, \hat{v}, \hat{w}) = \hat{D}_i; \qquad i = 1, 2, 3 \tag{63}$$

Here L_i is the linear operator for the ith boundary condition. This can include derivatives in the wall normal direction. The operator may also depend on the wave number (for example when the boundary condition contains horizontal derivatives). Note that the expression for evaluation L_i may include $\hat{\omega}$ as this is equivalent to horizontal derivatives. $\hat{D}_i$ is the data for the boundary condition, the most common form of which is is either zero (homogeneous boundary conditions) or the operator L_i applied to a base flow.

Finally inserting the expressions (59), (61), (62) into equation (63) and moving all terms containing the particular solution to the right hand side, we get a three by three linear system of equations which is easily solved to find the C's.

For $k = 0$ we solve

$$(D^2 - \lambda^2)\hat{u}_{p0}^{n+1} = \hat{f}_{01}^n \qquad \hat{u}_{p0}^{n+1}(0) = u_{low};\ \hat{u}_{p0}^{n+1}(y_L) = u_{upp} \tag{64}$$

$$(D^2 - \lambda^2)\hat{w}_{p0}^{n+1} = \hat{f}_{03}^n \qquad \hat{w}_{p0}^{n+1}(0) = w_{low};\ \hat{w}_{p0}^{n+1}(y_L) = w_{upp} \tag{65}$$

$$(D^2 - \lambda^2)\hat{u}_{h0}^{n+1} = 0 \qquad \hat{u}_{h0}^{n+1}(0) = 0;\ \hat{u}_{h0}^{n+1}(y_L) = 2 \tag{66}$$

$$(D^2 - \lambda^2)\hat{w}_{h0}^{n+1} = 0 \qquad \hat{w}_{h0}^{n+1}(0) = 0;\ \hat{w}_{h0}^{n+1}(y_L) = 2 \tag{67}$$

where u_{low}, u_{upp},w_{low} and w_{upp} denote the lower and upper wall velocities. Computations in a moving reference frame can increase the time step. If the boundary condition at the upper wall is in the form is of Dirichlet type (specified velocity) then

$$\hat{u}_0 = \hat{u}_{p0} \tag{68}$$

$$\hat{w}_0 = \hat{w}_{p0} \tag{69}$$

For other types of upper wall boundary conditions we find the complete solution from :

$$\hat{u}_0 = \hat{u}_{p0} + C_u \hat{u}_{h0} \tag{70}$$

$$\hat{w}_0 = \hat{w}_{p0} + C_w \hat{w}_{h0} \tag{71}$$

where C_u and C_w are chosen so that $\hat{u}_0$ and $\hat{w}_0$ fulfill the boundary conditions.

The above equations are all in Fourier space, where the non-linear terms h_v, h_ω, H_1 and H_3 become convolution sums. These sums can be efficiently calculated by transforming the velocities and vorticities using FFTs to physical space, where they are evaluated using pointwise products.

2.7. Normal discretization – Chebyshev expansion. The typical equation derived above is a second order constant coefficient ODE of the form

$$(D^2 - \kappa)\hat{\psi} = \hat{f} \qquad \hat{\psi}(0) = \gamma_{-1}, \quad \hat{\psi}(y_L) = \gamma_1, \tag{72}$$

First map the interval $[0, y_l]$ to $[-1, 1]$ by setting $y' = 2y/y_L - 1$. Then

$$(D^{'2} - \nu)\hat{\psi} = \hat{f} \qquad \hat{\psi}(-1) = \gamma_{-1}, \quad \hat{\psi}(1) = \gamma_1, \tag{73}$$

Where $\nu = \kappa y_L^2/4$. In the following we have for simplicity dropped the prime.

This equation can be solved accurately if the dependent variable $\hat{\psi}$, its second derivatives, the right hand side $\hat{f}$ and the boundary conditions are expanded in Chebyshev series, i.e.,

$$\hat{\psi}(y) = \sum_{j=0}^{N_y} \tilde{\psi}_j T_j(y), \tag{74}$$

$$D^2\hat{\psi}(y) = \sum_{j=0}^{N_y} \tilde{\psi}_j^{(2)} T_j(y), \tag{75}$$

$$\hat{f}(y) = \sum_{j=0}^{N_y} \tilde{f}_j T_j(y), \tag{76}$$

$$\hat{\psi}(1) = \sum_{j=0}^{N_y} \tilde{\psi}_j = \gamma_1 \tag{77}$$

$$\hat{\psi}(-1) = \sum_{j=0}^{N_y} \tilde{\psi}_j (-1)^j = \gamma_{-1}, \tag{78}$$

where T_j are the Chebyshev polynomial of order j and N_y the highest order of polynomial included in the expansion. If the Chebyshev expansions are used in Eq. (73), together with the orthogonality properties of the Chebyshev polynomials, we find the following relation between the coefficients

$$\tilde{\psi}_j^{(2)} - \nu\tilde{\psi}_j = \tilde{f}_j. \qquad j = 0, \ldots N_y \tag{79}$$

By writing the Chebyshev functions as cosines and using well known trigonometric identities, one finds relations between the Chebyshev coefficients of $\hat{\psi}$ and those of its derivative that can be used for differentiation and integration (see Canuto *et al.* 1988)

$$\tilde{\psi}_j^{(p)} = \sum_{\substack{m=j+1 \\ m+j \ odd}}^{N_y} m\tilde{\psi}_m^{(p-1)} \qquad j = 1, \ldots N_y, \tag{80}$$

$$\tilde{\psi}_j^{(p-1)} = \frac{1}{2j}(c_{j-1}\tilde{\psi}_{j-1}^{(p)} - \tilde{\psi}_{j+1}^{(p)}) \qquad j = 1, \ldots N_y, \tag{81}$$

where the superscript p indicates the order of the derivative and $c_j = 2$ for $j = 0$ and $c_j = 1$ for $j > 0$. In the first differentiation relation one observes that an error in the highest order coefficients of $\tilde{\psi}^{(p-1)}$ influences all coefficients of its derivative $\tilde{\psi}^{(p)}$. This problem is what is supposed to be avoided by the Chebyshev integration method discussed below. In the second relation we assume that $\tilde{\psi}_j^{(p)} = 0$ for $j > N_y$ and note that $\tilde{\psi}_0^{(p-1)}$ is an integration constant needed when the function $\hat{\psi}^{(p-1)}$ is found by integrating $\hat{\psi}^{(p)}$. Note also that the integration procedure introduces a truncation error, since an integration of a Chebyshev polynomial would result in a polynomial of one degree higher. The coefficient $\tilde{\psi}_{N_y+1}^{(p-1)}$ which would have multiplied T_{N_y+1} is in the present truncation set to zero.

If the relations (81) is used together with relation (79) a systems of equations can be derived for either coefficients $\tilde{\psi}_j$ or $\tilde{\psi}_j^{(2)}$. The second approach, called the Chebyshev integration method (CIM), was proposed by Greengaard (1991) to avoid the ill conditioned process of numerical differentiation in Chebyshev space. It was implemented in the original channel code by Lundbladh, Henningson & Johanson (1992) and is also included in the present implementation. However, we have found that using this method subtle numerical instabilities occurs in some cases and we therefore recommend to solve for the coefficients of the function itself, $\tilde{\psi}_j$. Such a Chebyshev tau method (CTM), almost identical to that used by Kim, Moin & Moser, is also implemented and is so far found to be stable. We first present the CTM, then the CIM and finally we discuss the instabilities observed in computations with the CIM. Note that the instabilities has occurred only a few times and that the results otherwise are the same for the two methods.

2.7.1. *Chebyshev tau method-CTM.* If the recursion relation (81) is used to express equations (79) in the coefficients $\tilde{\psi}_j$, one arrives at the system of equations (82 below). A more detailed derivation can be found in Canuto *et al.* (1988), but observe the sign errors therein. We have

$$
\begin{aligned}
-\frac{c_{j-2}\lambda}{4j(j-1)}\tilde{\psi}_{j-2} + \left(1+\frac{\lambda}{2(j^2-1)}\right)\tilde{\psi}_j + \frac{\lambda}{4j(j+1)}\tilde{\psi}_{j+2} \quad &= \\
\frac{c_{j-2}}{4j(j-1)}\tilde{f}_{j-2} - \frac{\beta_j}{2(j^2-1)}\tilde{f} + \frac{\beta_{j+2}}{4j(j+1)}\tilde{f}_{j+2}, \qquad & j=2,\dots,N_y
\end{aligned}
\tag{82}
$$

where

$$
\beta_n = \begin{cases} 1 & 0 \le j \le N_y - 2 \\ 0 & n > N_y - 2 \end{cases}
\tag{83}
$$

Note that the even and odd coefficients are uncoupled. Since a Chebyshev polynomial with an odd index is an odd function, and vice versa, the decoupling of the systems of equations is just a result of the odd and even decoupling of equation (73) itself. The same can be achieved for the boundary conditions (77) and (78) if they are added and subtracted,

$$
\sum_{\substack{j=0 \\ j\ even}}^{N_y} \tilde{\psi}_j = \frac{\gamma+\gamma_-}{2}, \qquad \sum_{\substack{j=1 \\ j\ odd}}^{N_y} \tilde{\psi}_j = \frac{\gamma-\gamma_-}{2}
\tag{84}
$$

These boundary condition together with the equations (82) constitutes a linear system of $N_y + 1$ equations that can be solved for the coefficients $\tilde{\psi}_j$ ($j = 0, \dots, N_y$). The structure of the equations involving the even coefficients forms a tridiagonal system and so does the equation for the odd coefficients. The boundary conditions fills the top row of both systems and makes the only quasi-tridiagonal but it only takes $16N_y$ operations to solve both systems.

The system (82) has in fact been truncated to only contains $N_y - 1$ equations and two equations has been replaced by boundary conditions. That truncation introduces what is usually called the tau error. In solution algorithms that solve for the three velocity components of the Navier-Stokes equations and the pressure, the coupling between the equations for the velocities and that for the pressure requires corrections of the tau error (Kleiser & Schumann, Werne 1995). We have chosen to eliminate the pressure in the Navier-Stokes equations and solve for the normal velocity and the normal vorticity and as those equations do not couple in the same way we do not have to correct the tau error.

2.7.2. *Chebyshev integration method-CIM.* Instead of solving for the coefficients $\tilde{\psi}_j$, the CIM solves for the coefficients of the Chebyshev series for the second derivative, $\tilde{\psi}_j^{(2)}$. The major advantage is supposed to comes in the calculation of derivatives of the solution $\hat{\psi}$. Derivatives are needed in the calculation of the remaining velocities and vorticities using equations (38)-(41). In the CIM the second derivative is already calculated and the first derivative and the function itself can be found by the numerically well conditioned process of integration.

If the relations (81) are used to write (79) in terms of $\tilde{\psi}_j^{(2)}$ the result is the following system of equations,

$$\begin{aligned}
j=0: &\quad \tilde{\psi}_0^{(2)} - \nu\tilde{\psi}_0 &&= \tilde{f}_0\\
j=1: &\quad \tilde{\psi}_1^{(2)} - \nu(\tilde{\psi}_0^{(1)} - \tfrac{1}{8}\tilde{\psi}_1^{(2)} + \tfrac{1}{8}\tilde{\psi}_3^{(2)} &&= \tilde{f}_1\\
2 \le j \le N_y-2: &\quad \tilde{\psi}_j^{(2)} - \nu\frac{1}{4j}\left[\frac{c_{j-2}\tilde{\psi}_{j-2}^{(2)}}{j-1} - \tilde{\psi}_j^{(2)}\left(\frac{1}{j-1}+\frac{1}{j+1}\right) + \frac{\tilde{\psi}_{j+2}^{(2)}}{j+1}\right] &&= \tilde{f}_j\\
j=N_y-1: &\quad \tilde{\psi}_{N_y-1}^{(2)} - \nu\frac{1}{4(N_y-1)}\left[\frac{\tilde{\psi}_{N_y-3}^{(2)}}{N_y-2} - \tilde{\psi}_{N_y-1}^{(2)}\left(\frac{1}{N_y-2}+\frac{1}{N_y}\right)\right] &&= \tilde{f}_{N_y-1}\\
j=N_y: &\quad \tilde{\psi}_{N_y}^{(2)} - \nu\frac{1}{4N_y(N_y-1)}(\tilde{\psi}_{N_y-2}^{(2)} - \tilde{\psi}_{N_y}^{(2)}) &&= \tilde{f}_{N_y}
\end{aligned} \tag{85}$$

The equations for odd and even coefficients decouple and so do the boundary conditions on the form (84). However, we now need to rewrite them with the aid of (79) to contain the coefficients of $\tilde{\psi}^{(2)}$ that we are now solving for. We find that the first sum in (84) takes the form

$$\begin{aligned}
\tilde{\psi}_0 + \tilde{\psi}_0^{(1)} &\quad + \tfrac{1}{4}\tilde{\psi}_0^{(2)} - \tfrac{1}{12}\tilde{\psi}_1^{(2)} - \tfrac{7}{48}\tilde{\psi}_2^{(2)} + \textstyle\sum_{j=3}^{N_y-2}\frac{3\tilde{\psi}_j^{(2)}}{(j-2)(j-1)(j+1)(j+2)}\\
&\quad - \frac{(N_y-6)\tilde{\psi}_{N_y-1}^{(2)}}{4(N_y-3)(N_y-2)N_y} - \frac{\tilde{\psi}_{N_y}^{(2)}}{2(N_y-2)(N_y-1)N_y} = \gamma_1
\end{aligned} \tag{86}$$

Thus, the solution of Eq. (73) is found by solving the system of equations for the second derivative of $\tilde{\psi}$ together with the boundary conditions (86) and the corresponding one at $y=-1$. We now have two more equations than for the tau method and the solution to the full system is a set of N_y+1 coefficients of the second derivative and the two integration constants $\tilde{\psi}_0^{(1)}$ and $\tilde{\psi}_0^{(2)}$ representing the zeroth order Chebyshev coefficient of $D\hat{\psi}$ and $\hat{\psi}$ itself, respectively. The function $\hat{\psi}$ is then found by two integrations, which in Chebyshev space can easily be constructed using the relations (81). The same quasi-tridiagonal form of the equation systems for the odd and even coefficients appears as for the CTM and the same solution routine can be used.

2.7.3. *Integration correction.* When the solution for $\hat{\psi}^{(2)}$ is found by the CIM and integrated to obtain $\hat{\psi}^{(1)}$ and $\hat{\psi}$ the same truncation is used both the derivatives $\hat{\psi}$ itself. They are all represented with $N_y + 1$ non-zero Chebyshev coefficients. This means that the truncation of the two are not compatible, since the derivative of a function represented as a finite Chebyshev series should have one coefficient less than the function itself. For example, if the coefficients $\tilde{\psi}_j$ are used to construct those for the derivative, using the recurrence relation (80), the result will not be the same as the coefficients $\tilde{\psi}_j^{(1)}$. There will be a slight difference in half of the coefficients for the derivative, the size depending on the magnitude of the coefficient $\tilde{\psi}_{N_y}$. The expression for the difference can be derived as follows. We write $\hat{\psi}$ explicitly using the coefficients $\tilde{\psi}_j^{(1)}$ and the relation (81)

$$\hat{\psi} = \tilde{\psi}_0 T_0 + \sum_{j=1}^{N_y-1} \frac{1}{2j}(c_{j-1}\tilde{\psi}_{j-1}^{(1)} - \tilde{\psi}_{j+1}^{(1)})T_j + \frac{1}{2N_y}\tilde{\psi}_{N_y-1}^{(1)} T_{N_y} \tag{87}$$

Now (80) is applied to the Chebyshev coefficients in (87) to calculate the derivative $D\hat{\psi}$. Let $\tilde{\psi}_j^D$ be its new coefficients. We find that these new coefficients will not equal $\tilde{\psi}_j^{(1)}$ and the following relation between them is found

$$\begin{aligned} \tilde{\psi}_j^D &= \tfrac{2}{c_j} \textstyle\sum_{\substack{q=j+1 \\ q+j\ odd}}^{N_y} (c_{q-1}\tilde{\psi}_{q-1}^{(1)} - \tilde{\psi}_{q+1}^{(1)}) + \frac{1}{c_j}\tilde{\psi}_{N_y-1}^{(1)} \\ &= \tilde{\psi}_j^{(1)} \qquad\qquad q + N_y\ odd \end{aligned} \tag{88}$$

and

$$\begin{aligned} \tilde{\psi}_j^D &= \tfrac{2}{c_j} \textstyle\sum_{\substack{q=j+1 \\ q+j\ odd}}^{N_y} (c_{q-1}\tilde{\psi}_{q-1}^{(1)} - \tilde{\psi}_{q+1}^{(1)}) \\ &= \tilde{\psi}_j^{(1)} - \tfrac{1}{c_j}\tilde{\psi}_{N_y}^{(1)} \qquad\qquad q + N_y\ even \end{aligned} \tag{89}$$

Thus we have a method of correcting the coefficients $\tilde{\psi}_j^{(1)}$ so that they represent $D\hat{\psi}$ with the same truncation as $\tilde{\psi}_j$ represent $\hat{\psi}$. A similar correction can be derived for the coefficients $\tilde{\psi}_j^{(2)}$ of the second derivative. After some algebra we find

$$\tilde{\psi}_j^{D^2} = \tilde{\psi}_j^{(2)} - \tfrac{1}{c_j}\left(1 + \tfrac{(N_y-1)^2-j^2}{4N_y}\right)\tilde{\psi}_{N_y-1}^{(2)} \qquad j + N_y\ odd \tag{90}$$

$$\tilde{\psi}_j^{D^2} = \tilde{\psi}_j^{(2)} - \tfrac{1}{c_j}\tilde{\psi}_{N_y}^{(2)} \qquad j + N_y\ even \tag{91}$$

where $\tilde{\psi}_j^{D^2}$ are the corrected Chebyshev coefficients for $D^2\hat{\psi}$.

When the horizontal components of velocity and vorticity are found using the relations (38) to (41), we need $\hat{\phi}$, $D\hat{v}$ and $D\hat{\omega}$. The above corrections are therefore needed in order for the velocity and vorticity fields to exactly satisfy the incompressibility constraint (2). Note that an error in the highest Chebyshev coefficients will by the above correction scheme affect all other coefficients of the first and second derivative. Exactly what was supposed to be avoided by the integration method.

The CTM and CIM methods are equally efficient and give the same results with the exception of a few very rare cases. We have found that numerical instabilities may occur when the wall normal resolution is very low and the velocity and vorticity fields are not divergence free. We have also found that it in those cases is enough to make the vorticity divergence free to stabilize the calculations. With integration correction or the CTM method, both velocity and vorticity are completely divergence free. However, for one channel flow case so far, and more frequently in the boundary layer, a numerical instability occurs with the integration correction but not without.

Fortunately the instability cause the calculation to blow up in a few time-steps and before that the results are the same as for a stable version of the code. With sufficient wall normal resolution (which is required anyhow) and without the integration correction the boundary layer code has been found completly reliable. The CTM method is, however, to prefer.

References

BECH, K. H., HENNINGSON, D. S. & HENKES, R. A. W. M. 1998. Linear and non-linear development of localized disturbances in zero and adverse pressure gradient boundary layers. *To appear in Phys. Fluids.* .

BERLIN, S., HANIFI, A. & HENNINGSON, D. S. 1998. The neutral stability curve for non-parallel boundary layer flow. Submitted to Phys. Fluids.

BERLIN, S. & HENNINGSON, D. S. 1998. A new nonlinear mechanism for receptivity of free-stream disturbances. Submitted to Phys. Fluids.

BERLIN, S., KIM, J. & HENNINGSON, D. S. 1998. Control of oblique transition by flow oscillations. Technical Report TRITA-MEK 1998:6, Royal Institute of Techmology, Stockholm.

BERLIN, S., LUNDBLADH, A. & HENNINGSON, D. S. 1994. Spatial simulations of oblique transition. *Phys. Fluids.* **6**, 1949–1951.

BERLIN, S., WIEGEL, M. & HENNINGSON, D. S. 1998. Numerical and experimental investigation of oblique boundary layer transition. Submitted to jfm.

BERTOLOTTI, F. P., HERBERT, T. & SPALART, P. R. 1992. Linear and nonlinear stability of the Blasius boundary layer. *J. Fluid Mech.* **242**, 441–474.

CANUTO, C., HUSSAINI, M. Y., QUARTERONI, A. & ZANG, T. A. 1988. *Spectral Methods in Fluids Dynamics.* Springer.

ELOFSSON, P. A. & LUNDBLADH, A. 1994. Ribbon induced oblique transition in plane poiseulle flow. In *Bypass transition - proceedings from a mini-workshop* (HENNINGSON, D. S., editor), pp. 29–41. TRITA-MEK Technical Report 1994:14, Royal Institute of Technology, Stockholm, Sweden.

GREENGARD, L. 1991. Spectral integration and two-point boundary value problems. *SIAM J. Numer. Anal.* **28**, 1071–1080.

HENNINGSON, D. S. 1995. Bypass transition and linear growth mechanisms. In *Advances in turbulence V* (BENZI, R., editor), pp. 190–204. Kluwer Academic Publishers.

HENNINGSON, D. S., JOHANSSON, A. V. & LUNDBLADH, A. 1990. On the evolution of localized disturbances in laminar shear flows. In *Laminar-Turbulent Transition* (ARNAL, D. & MICHEL, R., editors), pp. 279–284. Springer-Verlag.

HENNINGSON, D. S. & LUNDBLADH, A. 1994. Transition in Falkner-Skan-Cooke flow. *Bull. Am. Phys. Soc.* **39**, 1930.

HENNINGSON, D. S., LUNDBLADH, A. & JOHANSSON, A. V. 1993. A mechanism for bypass transition from localized disturbances in wall bounded shear flows. *J. Fluid Mech.* **250**, 169–207.

HILDINGS, C. 1997. Simulations of laminar and transitional separation bubbles. Technical report, Department of Mechanics, The Royal Institute of Technology, Stockholm, Sweden.

HÖGBERG, M. & HENNINGSON, D. S. 1998. Secondary instability of cross-flow vortices in Falkner-Skan-Cooke boundary layers. To appear in jfm.

KIM, J., MOIN, P. & MOSER, R. 1987. Turbulence statistics in fully developed channel flow. *J. Fluid Mech.* **177**, 133–166.

KREISS, G., LUNDBLADH, A. & HENNINGSON, D. S. 1994. Bounds for threshold amplitudes in subcritical shear flows. *J. Fluid Mech.* **270**, 175–198.

LU, Q. & HENNINGSON, D. S. 1990. Subcritical transition in plane Poiseuille flow. *Bull. Am. Phys. Soc.* **35**, 2288.

LUNDBLADH, A., 1993. Growth of a localized disturbance in inviscidly stable shear flow. TRITA-MEK 93-04, Royal Institute of Technology, Stockholm, Sweden.

LUNDBLADH, A., BERLIN, S., SKOTE, M., HILDINGS, C., CHOI, J., KIM, J. & HENNINGSON, D. S., 1998. An efficient spectral method for simulation of incompressible flow over a flat plate. FFA TN (in preparation) Technical Report from the Aeronautical Research Institute of Sweden (FFA), Bromma.

LUNDBLADH, A. & HENNINGSON, D. S., 1993. Numerical simulation of spatial disturbance development in rotating channel flow. FFA-TN 1993-30, Aeronautical Research Institute of Sweden, Bromma.

LUNDBLADH, A. & HENNINGSON, D. S., 1995. Evaluation of turbulence models from direct numerical simulations of turbulent boundary layers. FFA-TN 1995-09, Aeronautical Research Institute of Sweden, Bromma.

LUNDBLADH, A., HENNINGSON, D. S. & JOHANSSON, A. V., 1992. An efficient spectral integration method for the solution of the Navier-Stokes equations. FFA-TN 1992-28, Aeronautical Research Institute of Sweden, Bromma.

LUNDBLADH, A., HENNINGSON, D. S. & REDDY, S. C. 1994. Threshold amplitudes for transition in channel flows. In *Transition, Turbulence and Combustion, Volume I* (HUSSAINI, M. Y., GATSKI, T. B. & JACKSON, T. L., editors), pp. 309–318. Kluwer, Dordrecht.

LUNDBLADH, A. & JOHANSSON, A. V. 1991. Direct simulation of turbulent spots in plane Couette flow. *J. Fluid Mech.* **229**, 499–516.

LUNDBLADH, A., JOHANSSON, A. V. & HENNINGSON, D. S., 1992. Simulation of the breakdown of localized disturbances in boundary layers. Proceedings of the 4th European Turbulence Conference, Delft, The Netherlands.

LUNDBLADH, A., SCHMID, P. J., BERLIN, S. & HENNINGSON, D. S., 1994. Simulation of bypass transition in spatially evolving flows. Proceedings of the AGARD Symposium on Application of Direct and Large Eddy Simulation to Transition and Turbulence, AGARD-CP-551.

MALIK, M. R., ZANG, T. A. & HUSSAINI, M. Y. 1985. A spectral collocation method for the Navier-Stokes equations. *J. Comp. Phys.* **61**, 64–88.

NORDSTRÖM, J., NORDIN, N. & HENNINGSON, D. S. 1997. The fringe region technique and the fourier-method used in the direct numerical simulation of spatially evolving viscous flows. *Submitted to SIAM J. Sci. Comp.* .

REDDY, S. C., SCHMID, P. J., BAGGET, P. & HENNINGSON, D. S. 1998. On stability of streamwise streaks and transition thresholds in plane channel flows. *J. Fluid Mech.* . (Accepted for publication).

SCHMID, P. J. & HENNINGSON, D. S. 1992. A new mechanism for rapid transition involving a pair of oblique waves. *Phys. Fluids A.* **4**, 1986–1989.

SCHMID, P. J. & HENNINGSON, D. S. 1993. Nonlinear energy density transfer during oblique transition in plane Poiseuille flow. Technical Report TRITA-MEK 1993:5, Royal Institute of Technology, Stockholm.

SCHMID, P. J., LUNDBLADH, A. & HENNINGSON, D. S. 1994. Spatial evolution of disturbances in plane Poiseuille flow. In *Transition, Turbulence and Combustion, Volume I* (HUSSAINI, M. Y., GATSKI, T. B. & JACKSON, T. L., editors), pp. 287–297. Kluwer, Dordrecht.

SCHMID, P. J., REDDY, S. C. & HENNINGSON, D. S. 1996. Transition thresholds in boundary layer and channel flow. In *Advances in Turbulence VI* (GAVRILAKIS, S., MACHIELS, L. & MONKEWITZ, P. A., editors), pp. 381–384. Kluwer Academic Publishers.

SPALART, P. R. & YANG, K. 1987. Numerical study of ribbon induced transition in blasius flow. *J. Fluid Mech.* **178**, 345–365.

WERNE, J. 1995. Incompressibility and no-slip boundaries in the chebychev-tau approximation: correction to kleiser and schumann's influence-matrix solution. *J. Comp. Phys.* **120**, 260–265.